Università degli Studi di Bologna
Facoltà di Scienze Matematiche Fisiche
e Naturali

Dottorato di Ricerca in Fisica
XII Ciclo

Exclusive Photoproduction of $J/\psi \to \mu^+\mu^-$ in e-p interactions at HERA

Candidato:
Dr. Alessandro Polini

Tutore:
Prof. Maurizio Basile

Coordinatore:
Prof. Giulio Pozzi

A mia madre e mio padre

Contents

Introduction **1**

Introduzione **3**

1 Vector Meson Production in *ep* Scattering **5**
1.1 Lepton-Proton Scattering 5
1.2 Photon-Proton Scattering 8
1.3 Vector Dominance Model 9
1.4 Regge Phenomenology 10
1.5 Vector Meson Photoproduction 13
1.5.1 Elastic Photoproduction of light $(\rho^\circ, \omega, \phi)$ Vector Mesons 14
1.5.2 Elastic Photoproduction of J/ψ mesons 15
1.6 Decay Angular Distributions 17
1.7 Monte Carlo Generators 18
1.7.1 DIPSI 18
1.7.2 EPSOFT 20
1.7.3 LPAIR 21

2 HERA and the ZEUS Detector **23**
2.1 The HERA Collider 23
2.2 The ZEUS Detector 25
2.3 The Central Tracking Detector 28
2.4 The Uranium Calorimeter 29
2.5 The Forward Muon Spectrometer 31
2.5.1 The LST planes and the Limited Streamer Regime 32
2.5.2 The Drift Chambers 33
2.5.3 The FMUON Trigger System 34
2.6 The Barrel and Rear Muon Detectors 34
2.7 The Luminosity Monitor 36
2.8 The Proton Remnant Tagger 37
2.9 The Veto Wall and the C5 Counters 38
2.10 The ZEUS Trigger and Data Acquisition Systems 38

3 Data Selection **43**
3.1 Introduction 43
3.2 First Level Trigger 43

3.2.1 FLT Selection . . . 45
3.3 Second Level Trigger . . . 45
3.4 Third Level Trigger . . . 47
3.4.1 FMUON TLT . . . 47
3.4.2 BMUON, RMUON TLT . . . 47
3.5 Event Reconstruction . . . 48
3.5.1 Tracking . . . 48
3.5.2 Muons . . . 48
3.6 Offline Event Selection . . . 48
3.7 Elastic Selection . . . 49
3.7.1 Cylinder Radius Tuning . . . 50
3.7.2 Energy Threshold Tuning For Noise Subtraction . . . 50
3.7.3 Mip compatibility . . . 51
3.8 Final Data Sample . . . 53

4 Data and Monte Carlo Studies 59
4.1 The Monte Carlo Chain . . . 59
4.2 Reconstruction of Kinematic Variables . . . 60
4.3 Kinematic Variables Resolution . . . 62
4.3.1 $W_{\gamma p}$ and t Binning . . . 62
4.4 Trigger Efficiency . . . 62
4.4.1 Momentum Correction . . . 67
4.5 Comparison of Data with Monte Carlo . . . 67

5 Signal Extraction 73
5.1 Background Studies . . . 73
5.2 Non-Resonant Background . . . 73
5.2.1 The Bethe-Heitler Process . . . 73
5.3 Resonant Background . . . 75
5.3.1 Proton Dissociation . . . 75
5.3.2 ψ' Contamination . . . 78

6 Results 83
6.1 Procedure for Obtaining a Cross Section . . . 83
6.2 Photoproduction Cross Section . . . 83
6.3 Systematic Uncertainties . . . 84
6.4 Elastic Cross Sections in W bins . . . 85
6.5 b Slope Extraction . . . 86
6.6 Pomeron Trajectory . . . 88
6.7 Decay Angular Distributions . . . 94

Conclusions 99

Conclusioni 101

Acknowledgements 107

Ringraziamenti **109**

Introduction

The subject of this thesis is the study of the process of elastic photoproduction of the J/ψ meson in electron-proton interactions, performed within the ZEUS experiment at DESY, Hamburg.

In the photoproduction regime, this process can be regarded as the interaction of a real photon with the proton, with a flux factor that can be calculated from QED. According to the Vector Meson Dominance Model, one can imagine that the photon fluctuates into a vector meson, with which it shares the quantum numbers, before interacting with the proton. The following elastic scattering with the proton can then be interpreted as the exchange of a Regge trajectory with the quantum numbers of the vacuum.

Crucial scales in this process are the 4-momentum transfer squared at the electron and proton vertices, Q^2, t and the mass of the produced vector meson. As one of these scales changes it is possible to investigate the transition between the "soft" regime, described by phenomenological theories à la Regge, and the "hard" regime, calculable with the perturbative QCD, where the real photon is treated as a quark-antiquark pair and the interaction at the proton vertex as the exchange of a colour singlet state consisting of gluons. According to this description, the cross section is sensitive to the square of the gluon density at low x in the proton which, as seen from previous measurements at HERA, would imply a strong increase in the slope as a function of the photon-proton center of mass energy $W_{\gamma p}$, not compatible with the phenomenological approaches.

In the study of elastic J/ψ photoproduction the large vector meson mass ($M_{J/\psi} \gg \Lambda_{QCD}$) provides the necessary hard scale for pQCD calculation to be valid.

The events considered were taken in the data-taking period 1996-1997, when the collider accelerated 820 GeV protons and 27.5 GeV positrons, and correspond to an integrated luminosity of 38 pb^{-1}. The J/ψ mesons are identified from the decay into a muon pair.

The selection is based on the muon chamber trigger and on specific requirements on calorimeter sections and central tracking detector. Kinematic variables have been reconstructed using the mesurement of the track momentum in the central detector.

The work is presented in the following way.

The first chapter, after a brief introduction on the kinematics of electron-proton and photon-proton interactions, provides the theoretical motivations and discusses the interest of vector meson production. Phenomenological models of the Regge type and QCD inspired models are described, the topology of the signal and background processes is shown and the models used in Monte Carlo simulation are presented.

In the second chapter the ZEUS experiment is described, with particular focus on the components relevant for this analysis.

In the third chapter the data selection is described, consistently following data acquisition, subsequent reconstruction and final off-line selection.

In the fourth chapter the selected data sample is studied and the results are compared with the Monte Carlo simulation.

In the fifth chapter the different background contributions included in the sample are estimated, with particular emphasis on proton dissociation and the Bethe Heitler $\gamma\gamma \to \mu^+\mu^-$ process.

In the sixth chapter the cross sections for the elastic production $\gamma p \to J/\psi p$ in different W bins are extracted. Then they are calculated in t bins for measuring the b slope and to search for shrinkage effects as predicted by Regge phenomenology.

Finally the parameters of the Regge trajectory describing the process (intercept $\alpha_{I\!P}(0)$ and slope $\alpha'_{I\!P}$) are extracted.

Introduzione

Argomento di questa tesi è lo studio del processo di fotoproduzione elastica del mesone J/ψ nelle interazioni elettrone-protone, effettuato nell'ambito dell'esperimento ZEUS a DESY, Amburgo.

Nel regime di fotoproduzione questo processo può essere visto come l'interazione di un fotone reale col protone, con un fattore di flusso calcolabile dalla QED.

In accordo col Modello della Dominanza Vettoriale, si può immaginare che il fotone fluttui in un mesone vettore, con gli stessi numeri quantici, prima di interagire con il protone. Il successivo scattering elastico può essere interpretato come scambio di una traiettoria di Regge con i numeri quantici del vuoto.

Scale fondamentali in questo processo sono il 4-impulso trasferito al quadrato ai vertici di elettrone e protone, Q^2 e t, e la massa del mesone vettore prodotto. Al variare di una di queste scale è possibile investigare la transizione fra regime "soft", descritto da teorie fenomenologiche alla Regge, e il regime "hard", calcolabile con la QCD perturbativa, dove il fotone reale è trattato come una coppia quark-antiquark e la interazione al vertice del protone come uno scambio di uno stato singoletto di colore formato da gluoni. Secondo questa descrizione la sezione d'urto è sensibile al quadrato della densità del gluone a basso x che, come visto in precedenti misure ad HERA, implicherebbe una forte crescita della slope in funzione della energia nel centro di massa $W_{\gamma p}$, non compatibile con gli approcci fenomenologici.

Nello studio della fotoproduzione elastica di J/ψ la grande massa del mesone vettore ($M_{J/\psi} \gg \Lambda_{QCD}$) fornisce la scala dura necessaria perché i calcoli di QCD perturbativa siano validi.

Gli eventi considerati furono presi nel periodo di misure 1996-1997, quando il collider accelerava protoni di 820 GeV e positroni di 27.5 GeV, e corrispondono a una luminosità integrata di 38 pb^{-1}. I mesoni J/ψ sono identificati dal decadimento in una coppia di muoni.

La selezione si basa sul trigger delle camere per muoni e su richieste specifiche sulle sezioni calorimetriche e sul rivelatore di tracce centrale. Le variabili cinematiche sono state ricostruite usando la misura dell'impulso delle tracce nel rivelatore centrale.

Il lavoro è presentato nel modo seguente.

Il primo capitolo, dopo una breve introduzione sulla cinematica delle interazioni elettrone-protone e fotone-protone, fornisce le motivazioni teoriche e discute l'interesse della produzione di mesoni vettori. Si descrivono i modelli fenomenologici del tipo di Regge e i modelli ispirati dalla QCD, si mostra la topologia del segnale e dei processi di fondo, e si presentano i modelli usati nella simulazione Monte Carlo.

Nel secondo capitolo si descrive l'esperimento ZEUS, con particolare riguardo alle

componenti rilevanti per questa analisi.

Nel terzo capitolo si descrive la selezione dei dati, seguendo in modo consistente l'acquisizione dei dati, la ricostruzione successiva e l'analisi off-line finale.

Nel quarto capitolo si studia il campione di dati selezionati e si confrontano i risultati con la simulazione Monte Carlo.

Nel quinto capitolo si stimano i diversi contributi di fondo contenuti nel campione, con particolare attenzione alla dissociazione del protone e al processo di Bethe-Heitler $\gamma\gamma \to \mu^+\mu^-$.

Nel sesto capitolo si estraggono le sezioni d'urto per la produzione elastica di $\gamma p \to J/\psi p$ in diversi bin di W. Esse sono poi calcolate in bin di t per misurare la slope b e per cercare effetti di shrinkage come previsti dalla fenomenologia di Regge. Infine si estraggono i parametri della traiettoria di Regge descrivente il processo (intercetta $\alpha_{I\!P}(0)$ e pendenza $\alpha'_{I\!P}$).

Chapter 1

Vector Meson Production in ep Scattering

1.1 Lepton-Proton Scattering

At first order, lepton-proton scattering is described by the Feynman diagram shown in Fig. 1.1. The incoming lepton interacts with the proton through the exchange of a virtual photon (γ^*) or one of the weak gauge bosons (Z^0, W^+, W^-)[1].

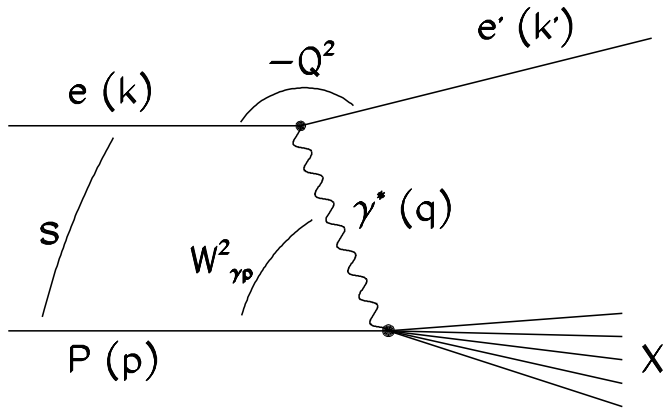

Figure 1.1: First order Feynman diagram describing the ep interaction. The four-momenta of the particles are in parentheses.

The kinematic variables relevant to the description of this process are obtained by the following four-momenta:

[1]For simplicity, from now on we will use the terms of electron and proton even if the subject may be easily extended to lepton-nucleon scattering. In most of the cases the word electron will refer to positrons since this study is based on positron-proton data. We will also neglect weak ep interactions, since they are irrelevant for the subject of this thesis.

- k, the four-momentum of the incoming lepton
- k', the four-momentum of the scattered lepton
- p, the four-momentum of the incoming proton
- q, the four-momentum of the exchanged virtual gauge boson.

The kinematics of the inclusive electron-proton scattering is completely described by the center of mass energy ($\sqrt{s}$):

$$s = (p + k)^2 \approx 4E_pE_e \tag{1.1}$$

being E_p, E_e the energies of the incoming proton and electron respectively, and any two of the following variables:

- the negative of the four-momentum transfer squared:

$$Q^2 = -q^2 = -(k - k')^2, \tag{1.2}$$

- the inelasticity:

$$y = \frac{p \cdot q}{p \cdot k} \tag{1.3}$$

  which corresponds to the fraction of the incoming lepton energy transferred at the lepton vertex in the proton rest frame,

- the Bjorken scaling variable:

$$x = \frac{Q^2}{2p \cdot q} \approx \frac{Q^2}{sy} \tag{1.4}$$

  which corresponds to the fraction of the proton momentum carried by the struck quark in the lowest order process and in the infinite proton momentum frame.

- the electron energy transferred in the proton rest frame:

$$\nu = \frac{p \cdot q}{m_p}, \tag{1.5}$$

- the photon-proton center of mass energy W:

$$W^2 = (p + q)^2 \approx sy - Q^2. \tag{1.6}$$

The ep cross section in a general formalism can be expressed as a function of the leptonic $(L^e)^{\mu\nu}$ and the hadronic tensor $W_{\mu\nu}$ describing respectively the electron and the proton vertex in the diagram of fig 1.1:

$$\frac{d^2\sigma}{dE'_e d\Omega} = \alpha^2 \frac{1}{Q^4} \frac{E'_e}{E_e} (L^e)^{\mu\nu} W_{\mu\nu} \tag{1.7}$$

where α is the electromagnetic coupling, the $1/Q^4$ term is the virtual photon propagator and the leptonic tensor $(L^e)^{\mu\nu}$ is completely calculable from QED:

$$(L^e)^{\mu\nu} = 2(k'^{\mu}k'^{\nu} + k'^{\nu}k'^{\mu} - (k' \cdot k - m^2)g^{\mu\nu}). \tag{1.8}$$

The hadronic tensor $W_{\mu\nu}$ is of the form

$$W^{\mu\nu} = -W_1 g^{\mu\nu} + \frac{W_2}{m_p^2}p^{\mu}p^{\nu} + \frac{W_4}{m_p^2}q^{\mu}q^{\nu} + \frac{W_5}{m_p^2}\left(p^{\mu}q^{\nu} + q^{\mu}p^{\nu}\right), \tag{1.9}$$

where the anti-symmetric part (W_3) has been omitted; the leptonic tensor $L^{\mu\nu}$ is symmetric since we are neglecting the weak interactions and the cross section has to be a scalar. From the current conservation at the proton vertex

$$q_{\mu}W^{\mu\nu} = q_{\nu}W^{\mu\nu} = 0, \tag{1.10}$$

$W^{\mu\nu}$ can be expressed as a function of two quantities only, W_1 and W_2:

$$W^{\mu\nu} = W_1\left(-g^{\mu\nu} + \frac{q^{\mu}q^{\nu}}{q^2}\right) + \frac{W_2}{m_p^2}\left(p^{\mu} - \frac{p\cdot q}{q^2}q^{\mu}\right)\left(p^{\nu} - \frac{p\cdot q}{q^2}q^{\nu}\right). \tag{1.11}$$

or performing the substitution

$$F_1 \equiv m_p W_1, \quad F_2 \equiv \frac{p\cdot q}{m_p}W_2, \tag{1.12}$$

the electron-proton cross section becomes:

$$\frac{d^2\sigma}{dQ^2 d\nu} = \frac{4\pi\alpha^2}{Q^4}\frac{E'_e}{E_e}\frac{1}{\nu}\left[F_2\left(Q^2,\nu\right)\cos^2\left(\frac{\theta}{2}\right) + \frac{2\nu}{m_p}F_1\left(Q^2,\nu\right)\sin^2\left(\frac{\theta}{2}\right)\right], \tag{1.13}$$

where the dependence has been expressed as a function of Q^2 and ν. $F_1(Q^2,\nu)$,$F_2(Q^2,\nu)$ are called *structure functions* of the proton and are related to the polarization state of the exchanged virtual photon. At high energies, using the adimensional variables x e y, equation (1.13) becomes

$$\frac{d^2\sigma}{dxdQ^2} = \frac{4\pi\alpha^2}{xQ^4}\left\{(1-y)\,F_2\left(x,Q^2\right) + y^2 x F_1\left(x,Q^2\right)\right\}, \tag{1.14}$$

Referring to Fig. 1.1 the exchanged boson of virtuality Q^2 can be viewed as a probe of the proton structure with a resolution r of

$$\Delta r = \frac{\hbar c}{\sqrt{Q^2}} \approx \frac{0.2}{\sqrt{Q^2}}\ \text{GeV fm} \tag{1.15}$$

This is especially true when $Q^2 \gg m_p^2$ and $W^2 \gg m_p^2$, also known as Deep Inelastic Scattering regime, where the intrinsic structure of the proton and its quark and gluon densities can be studied as function of Q^2 and x in a perturbative QCD approach.

1.2 Photon-Proton Scattering

At small virtualities ($Q^2 \simeq 0$), known as photoproduction regime, the photon may be considered real and the *ep* process can be used to study the properties and the structure of the photon itself as well as the photon-proton interaction.

The γp total hadronic cross section can be extracted from the electron-proton measurements since one is related to the other by means of a photon flux factor generated at the leptonic vertex which is calculable within QED. Thus the *ep* cross section can be factorised, as shown in Fig. 1.2, into:

$$\sigma_{ep} = \phi_{\gamma/e} \cdot \sigma_{\gamma p}, \tag{1.16}$$

where:

$$\phi_{\gamma/e} = \frac{\alpha}{2\pi} \int_{y_{min}}^{y_{max}} \left[\frac{1+(1-y)^2}{y} \ln\left(\frac{Q^2_{max}(y)}{Q^2_{min}(y)} \right) + \frac{2(y-1)}{y} \left(1 - \frac{Q^2_{min}(y)}{Q^2_{max}(y)} \right) \right] dy \tag{1.17}$$

is the flux of virtual photons emitted by the electron beam.

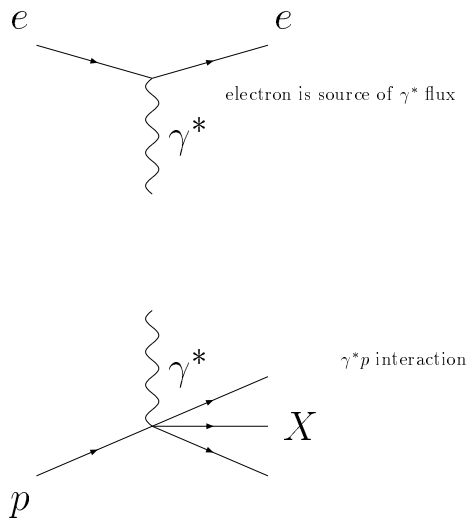

Figure 1.2: At small Q^2, *ep* scattering can be thought as radiation of a virtual photon (photon flux) followed by the $\gamma^* p$ scattering

The exchanged photon is treated as a massive spin 1 particle and acquires three polarization vectors corresponding to the helicities $\lambda = \pm 1, 0$, where in the last would become negligible for Q^2 sufficiently small. The cross section may depend on the photon helicity although for parity invariance reasons the cross section for $\lambda = \pm 1$ have to be equal. There will thus be two independent cross sections: one for absorbing a transversely polarized photon $\sigma_T(\lambda = \pm 1)$ and one for longitudinally polarized photons

$\sigma_L(\lambda = 0)$. The relations between these cross sections and the structure functions are:

$$2xF_1 = \frac{K}{4\pi^2\alpha}\frac{Q^2}{\nu}\sigma_T \quad (1.18)$$

$$F_2 = \frac{K}{4\pi^2\alpha}\frac{Q^2\nu}{Q^2+\nu^2}(\sigma_T + \sigma_L) \quad (1.19)$$

where K is the virtual photon flux defined according to the Hand convention as $K = \nu - Q^2/2m_p$.

1.3 Vector Dominance Model

Experimental features of hadron-hadron and photon-hadron scattering at high energy show that the photon under certain conditions exhibits an internal hadron-like structure. The Vector Dominance Model (VDM) represents the photon as a superposition of a bare photon and a hadronic component

$$|\gamma\rangle = N|\gamma\rangle_{bare} + \sqrt{\alpha}|\gamma\rangle_{hadronic} \quad (1.20)$$

where N is introduced for normalization reasons.

The uncertainty principle allows the bare photon to fluctuate into a $q\bar{q}$ pair with the same quantum numbers, i.e. $J^{PC} = 1^{--}$ and $Q, B, S = 0$ which are the quantum numbers of the three lightest vector mesons: ρ^0, ω, ϕ. If the fluctuation time $t_f \sim \frac{2\nu}{Q^2+M_V^2}$, where M_V is the mass of the vector meson the photon fluctuates into, is large compared to the interaction time, a photon-proton process similar to a hadronic type process may occur. According to the VDM model the hadronic component of the photon can be written as

$$\sqrt{\alpha}|\gamma\rangle_{hadronic} = \sum_V \frac{1}{f_V}\left(\frac{M_V^2}{M_V^2+Q^2}\right)|\gamma\rangle, \quad (1.21)$$

where f_V is the $\gamma \to V$ coupling. Vector meson production in γp reactions as well as in e^+e^- annihilation experiments, provides a solid basis for this picture. Data from these experiments have been used to extract the coupling constants f_V. From these assumptions one can determine the following expressions for the trasverse $\sigma^T_{\gamma^* p}(W, Q^2)$ and longitudinal $\sigma^L_{\gamma^* p}(W, Q^2)$ cross-sections for the interaction of virtual photons on protons at a center-of mass energy W and a momentum transfer Q^2:

$$\sigma^T_{\gamma^* p}(W, Q^2) = \sum_{V=\rho^0,\omega,\phi} \frac{4\pi\alpha}{f_V^2}\left(\frac{M_V^2}{M_V^2+Q^2}\right)^2 \sigma^T_{Vp}(W) \quad (1.22)$$

$$\sigma^L_{\gamma^* p}(W, Q^2) = \sum_{V=\rho^0,\omega,\phi} \frac{4\pi\alpha}{f_V^2}\left(\frac{M_V^2}{M_V^2+Q^2}\right)^2 \frac{Q^2}{m_V^2}\sigma^L_{Vp}(W) \quad (1.23)$$

where $\sigma^T_{Vp}(W)$ is the total cross-section of transversely polarized vector meson on protons at $Q^2 = 0$. The total cross section of longitudinally polarized vector mesons $\sigma^L_{Vp}(W)$ on protons at $Q^2 = 0$ is given by:

$$\sigma^L_{Vp}(W) = \xi_V \cdot \sigma^T_{Vp}(W) \quad (1.24)$$

The factor ξ_V accounts for the fact that the total transverse cross-section needs not to be the same as the total longitudinal one. ξ_V is expected to be within $0 \leq \xi_V \leq 1$ The ratio R of the total longitudinal to the total transverse $\gamma^* p$ cross-section is given by:

$$R = \frac{\sigma^L_{\gamma^* p}(W, Q^2)}{\sigma^T_{\gamma^* p}(W, Q^2)} = \xi_V \frac{Q^2}{m_V^2}. \tag{1.25}$$

1.4 Regge Phenomenology

Regge phenomenology has been successfully used to describe the hadron dynamics of two-particle scattering processes. It allows to estimate characteristic features of the behaviour of hadronic interactions in the high energy limit. The region of large values in W accessible at HERA corresponds to the high energy limit within the Regge approach and explains why the subject is still of interest. Even before the Regge models, the one particle exchange model (OPE) was developed to describe strong interactions in two-particle scattering processes. Within this framework, the exchange of one particle in the t channel with spin j yelds a scattering amplitude which is proportional to s^j and a total cross section proportional to $\sigma_{tot} \propto s^{2(j-1)}$. Such behaviour in the high energy limit would violate the Froissart bound, and, therefore, unitarity. The Regge phenomenology allows to avoid such difficulties by including multiple particle exchanges instead of a single particle exchange.

The scattering amplitude of a two-particle process using a decomposition into partial waves is given by:

$$\mathcal{A}(s,t) = \sum_{j=0}^{\infty} (2j+1) a_j(t) P_j(z) \tag{1.26}$$

where t is the Mandelstam variable representing the four-momentum exchanged at the hadron vertex and $z = \cos\theta_t = 1 - 2s/(t - 4m_j^2)$. The partial wave amplitude $a_j(t)$ of a resonance contribution which corresponds to a particular exchanged particle of mass m_j, decay width $\Gamma_j(t)$ and spin j can be viewed as a propagator like term and is given by:

$$a_j(t) = \frac{\Gamma_j(t)}{t - m_j^2}. \tag{1.27}$$

All possible exchanged particles fit on a line called Regge trajectory or Reggeon in a Chew-Frautschi plot (spin j versus mass m_j^2), as shown in Fig. 1.3. Each trajectory can be parametrized by a linear function $\alpha(t)$, i.e. $j = \alpha(m_j^2)$.

The main idea of the Regge approach is to evaluate the scattering amplitude $\mathcal{A}(s,t)$ taking into account all particles on a particular trajectory through an analitic continuation of the scattering amplitude into the complex angular momentum plane. The sum over exchanged particles is transformed into an integral by means of the Sommerfeld-Watson transformation:

$$\mathcal{A}(s,t) = \frac{1}{2i} \int_C dj (2j+1) \frac{\Gamma_j(t)}{t - m_j^2} \frac{e^{i\pi j} \pm 1}{2} \frac{P_j(z)}{\sin(\pi j)} \tag{1.28}$$

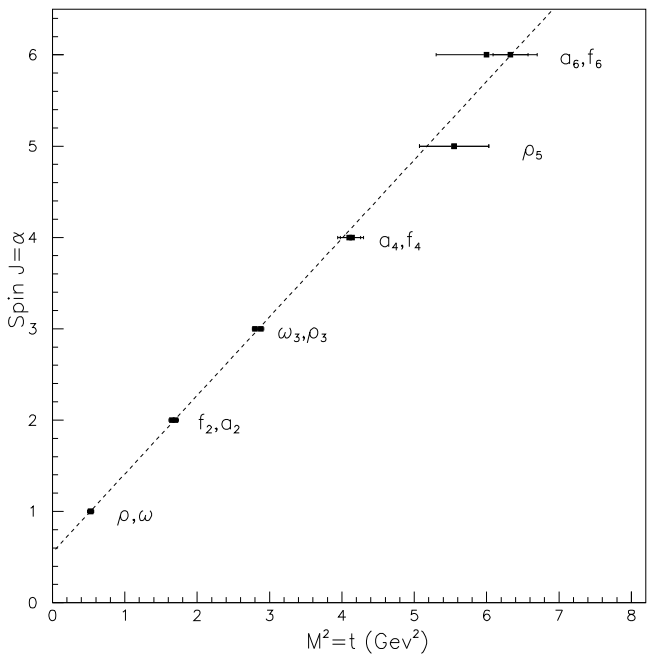

Figure 1.3: Chew-Frautschi plot: Spin J versus mass squared for different mesons. The line is the corresponding Regge trajectory.

Using the parametrization $\alpha(t)$ for the Regge trajectory, one can write the partial wave amplitude as $a_{0j}(t) = (\Gamma_j(t)d\alpha(t)/dt)/(\alpha(t) - j)$. Choosing a suitable path C in the Chew-Frautschi plane, the above integral is simply given by the residue of the poles at $\alpha(t) = j$ employing Cauchy's theorem:

$$\mathcal{A}(s,t) = -\pi \frac{e^{i\pi\alpha(t)} \pm 1}{2\sin(\pi\alpha(t))} (2\alpha(t)+1)\, \Gamma_{\alpha(t)} \frac{d\alpha(t)}{dt} P_{\alpha(t)}(z). \tag{1.29}$$

The asymptotic expression of the Legendre polynomials $P_{\alpha(t)}(z)$ for $|t| \gg s$ yields $P_{\alpha(t)} \approx e^{-i\pi\alpha(t)} \cdot (s/s_0)\alpha(t)$. In the high energy limit ($s \to \infty$), the scattering amplitude becomes:

$$\mathcal{A}(s,t) = \beta(t) \cdot \left(\frac{s}{s_0}\right)^{\alpha(t)} \tag{1.30}$$

and, via the Optical Theorem, that relates the total cross section to the immaginary part in the forward region:

$$\sigma_{tot} \propto s^{\alpha(t=0)-1}. \tag{1.31}$$

Measurements of the total cross-section of hadronic interactions have shown that σ_{tot} slowly rises as a function of the center of mass energy. Such behaviour cannot be

generated by any of the known trajectories since $\alpha(t=0) < 1$. It is therefore necessary to postulate the existence of a new trajectory (the pomeron) with $\alpha(t=0) \geq 1$ which explains the observed rise of the total cross-section at high energies. The pomeron is not an observed particle but a phenomenological object which follows from the high energy limit in the Regge approach.

Experimental results on elastic scattering of hadronic particles show that at low t the distribution $d\sigma/dt$ can be described by an exponential function. Thus, by replacing the function $\beta(t)$ in equation 1.30 with $e^{-b_0 t}$, one gets

$$\frac{d\sigma}{dt} \propto e^{-b_0 t} \left(\frac{s}{s_0}\right)^{2(\alpha(t)-1)} = e^{-b_t t} \left(\frac{s}{s_0}\right)^{2(\alpha(0)-1)} \tag{1.32}$$

where

$$b_t = b_0 + 2\alpha' \ln\left(\frac{s}{s_0}\right). \tag{1.33}$$

According to this view, Regge model predicts that the slope of the elastic differential distribution $d\sigma/dt$ has a logarithmic dependence on energy for non-zero values of α'. The dependence of b is known as "Regge shrinkage" since in a geometric picture the slope of the t dependence is due to the size of the scattering objects.

As mentioned earlier, all Regge trajectories from known particles have $\alpha(t=0) < 1$. Since at high energy the total cross section σ_{tot} is supposed to behave as $s^{\alpha(0)-1}$ (eq.1.31) the hadron cross sections should decrease with energy. This is true for $\sqrt{s} \leq 10$ GeV, but at higher energies experimental results show that the cross section are either constant or rise slowly with energy. This observation motivated the need for the pomeron trajectory, which has an intercept $\alpha(0) = 1 + \epsilon$ with $\epsilon \geq 0$. The exchanged "particles", which correspond to this trajectory, have the quantum numbers of vacuum. Donnachie and Landshoff [1] used experimental results of total cross sections for hadron-hadron and photon-hadron interactions to extract the pomeron trajectory. The cross sections were fitted to the form

$$\sigma_{tot} = X s^{\epsilon} + Y s^{-\eta}. \tag{1.34}$$

The first term describes the contribution from the pomeron trajectory which dominates at high energy while the second term accounts for the reggeon (i.e. the known particle trajectories) contributions which dominates at low energy. The results of the fits are $\epsilon = 0.0808$ and $\eta = 0.4525$. In the pomeron case, the t dependence of the trajectory was also extracted with a value $\alpha'_{I\!P} = 0.25$ GeV^{-2}, yelding the following parametrization of the pomeron trajectory:

$$\alpha_{I\!P} = 1.08 + 0.25t. \tag{1.35}$$

This pomeron trajectory, which describes the weak energy dependence of the total cross section is known as "soft" pomeron. The combination of VDM with a Regge "soft" pomeron has successfully described the experimental measurements of the total photoproduction cross section, as shown in Fig. 1.4.

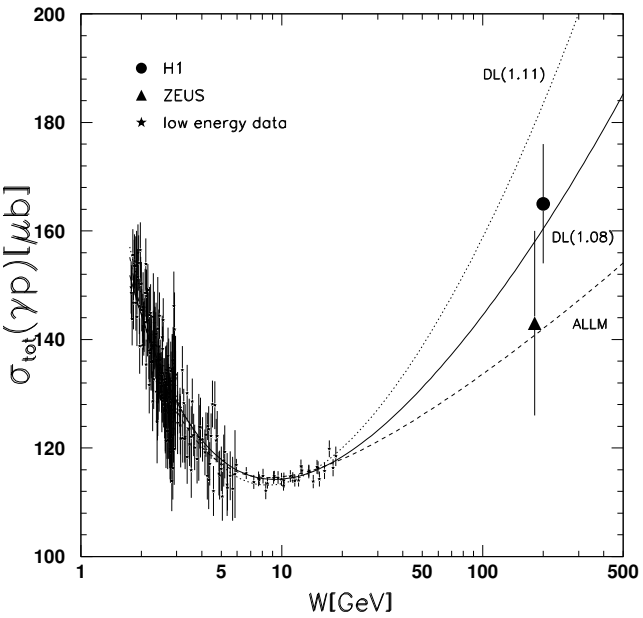

Figure 1.4: Total photoproduction cross section as a function of the γp center of mass energy $W_{\gamma p}$, as measured by the H1 [2] and ZEUS [3] collaborations. The results are compatible with an extrapolation of low energy measurements, using the energy dependence found in hadronic scattering. This indicates that the photon behaves similarly to a hadron. The curves are from the Regge inspired model by Donnachie-Landshoff with an $\alpha_0 = 1.08$ and $\alpha_0 = 1.11$ and from the ALLM parametrization [4].

1.5 Vector Meson Photoproduction

In ep interactions, vector mesons are produced via the interaction of the exchanged virtual photon with the incoming proton. There are several vector meson production processes in $\gamma^* p$ interactions. These processes can be separated into two groups: non diffractive and diffractive.

In non diffractive processes, color exchange takes place between the proton and the virtual photon via a gluon which interacts either directly with the virtual photon (direct photon processes) or with a parton of the photon itself (resolved photon processes) as shown in Fig. 1.5. The final state contains significant hadronic activity from the proton remnant, the hadronization of the emitted gluon (g_2 in Fig. 1.5) and the photon remnant (for the resolved process).

In diffractive processes, a colorless object with the same quantum numbers as the vacuum, the pomeron, is assumed to be exchanged between the proton and the virtual photon. Since no colour flow is present, the particles from the dissociation of photon and proton will appear well separated in rapidity with no hadronic activity in-between. Diffractive processes are usually referred to as single or double diffractive dissociation depending on whether the photon only or both photon and proton dissociate into higher

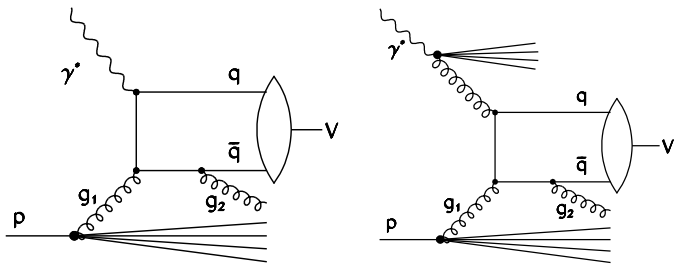

Figure 1.5: Diagrams of non-diffractive photon gluon fusion vector meson production processes. The direct photon on the left, the resolved on the right.

mass states. The special case of diffractive processes in which the photon dissociates into a vector meson and the proton remains intact, $\gamma p \to Vp$ (Fig.1.6 left), is called elastic or exclusive vector meson production and will be studied in detail in this thesis. The process $\gamma p \to VN$, in which the photon diffractively dissociates into a vector meson and the proton dissociates into a higher mass state N (Fig.1.6 right), is referred to as proton dissociative and represents one of the main background sources to the study of the elastic process.

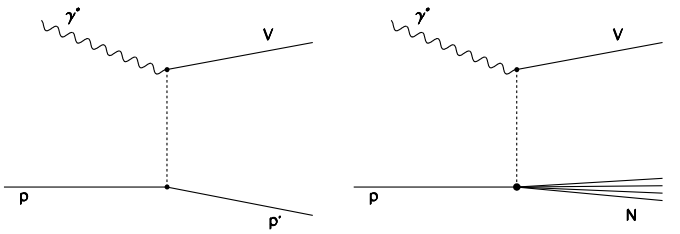

Figure 1.6: Diagrams of diffractive vector meson production processes: elastic vector meson production (left) and proton dissociative vector meson production (right)

1.5.1 Elastic Photoproduction of light (ρ°, ω, ϕ) Vector Mesons

Using the tools we have introduced in the previous sections, we can describe elastic photoproduction of vector mesons in the following way: a virtual photon, γ^*, emitted from the incoming electron, fluctuates according to the VDM into a virtual vector meson which then interacts with the proton through the exchange of a colourless object carrying the quantum numbers of vacuum, e.g. a pomeron. The absorption of the pomeron four-momentum puts the vector meson on mass shell.

Using equation 1.32 and a soft pomeron trajectory 1.35 this picture predicts that at high energies the $W_{\gamma^* p}$ dependence of the elastic cross section be:

$$\sigma^{el}_{\gamma^* p \to Vp} \propto \frac{(W^2_{\gamma^* p})^{2(\alpha_{I\!P}(0)-1)}}{b(W^2_{\gamma^* p})} \approx W^{0.22}_{\gamma^* p} \tag{1.36}$$

with a logarithmic $W_{\gamma^* p}$ dependence of the diffractive slope b given by:

$$b = b_0 + 4\alpha'_{I\!P} \ln\left(\frac{W_{\gamma^* p}}{W_0}\right) \tag{1.37}$$

This behaviour successfully describes the fixed target and HERA data as shown in Fig 1.7.

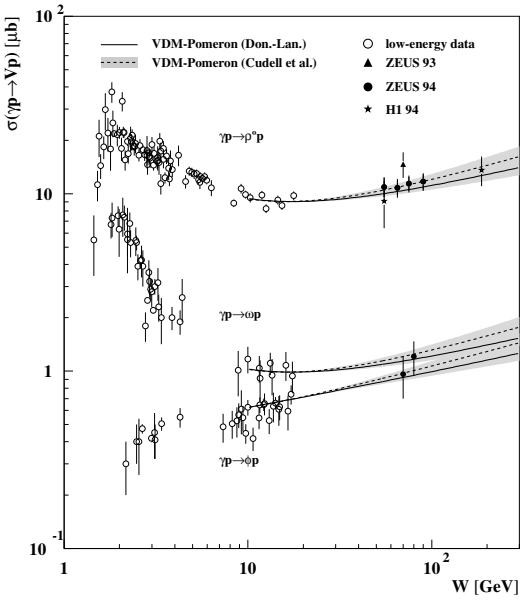

Figure 1.7: The elastic vector meson photoproduction cross sections as a function of the energy for light vector mesons. The solid curve is for the pomeron trajectory of Donnachie-Landshoff [1] while the dashed line is based on a model by Cudell et al. [5]

1.5.2 Elastic Photoproduction of J/ψ mesons

While the Donnachie-Landshoff model has been successful in describing the elastic production of light vector mesons it does not describe the elastic J/ψ production cross section. Fig 1.8 shows the elastic cross section for the different light vector mesons as well as the more massive J/ψ. The cross section for J/ψ production shows a much steeper $W_{\gamma^* p}$ dependence when compared to the ρ^0, ω or ϕ production.

Attempts have been made [6], [7] to describe this dependence in the framework of the Regge model introducing a "hard" pomeron trajectory (i.e. $\alpha_{I\!P}^{hard}(0) \gg \alpha_{I\!P}^{soft}(0) = 1.08$).

Another possibility is to try to use a perturbative QCD approach even at the low Q^2 values of the photoproduction regime, since in the case of the J/ψ the large meson mass could provide a large enough scale to apply perturbative QCD. In a model by Ryskin [8] the virtual photon fluctuates into a $c\bar{c}$ pair before interacting with the proton via a two gluon exchange. The outgoing $c\bar{c}$ pair then combines to form the J/ψ meson.

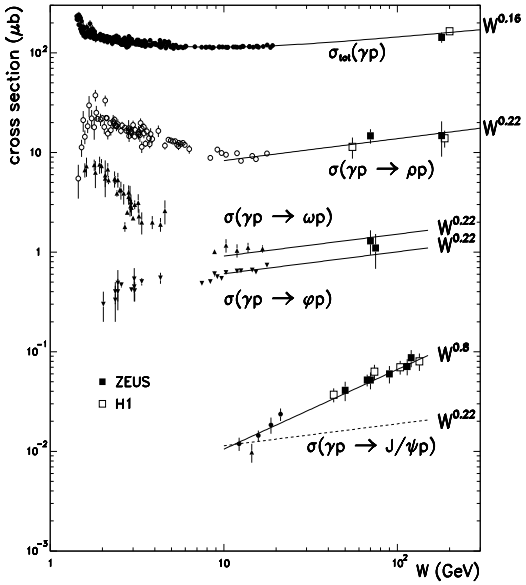

Figure 1.8: The energy dependence of the ρ^0, ω, ϕ and J/ψ elastic photoproduction cross sections measured at HERA, compared to measurements at lower energy and to the total photoproduction cross section. The lines illustrate a comparison of various power–law energy dependences at high energy.

The diagram for the process is shown in Fig. 1.9. The cross section is sensitive to the square of the gluon density in the proton evaluated at:

$$\bar{x} = \frac{Q^2 + M_{J/\psi}^2 - t}{W_{\gamma^* p}^2}, \quad \bar{q}^2 = \frac{Q^2 + M_{J/\psi}^2 - t}{4}. \tag{1.38}$$

The calculation is performed in the leading $\ln(Q^2)$ approximation of perturbative QCD and assumes a non-relativistic wavefunction for the J/ψ. The predicted cross section for elastic J/ψ production is:

$$\frac{d\sigma_T(\gamma^* p \to J/\psi p)}{dt} = \left[F_N^{2G}(t)\right]^2 \frac{\alpha_s^2 \Gamma_{ee}^{J/\psi} M_{J/\psi}^3 \pi^3}{3\alpha_{em}} \left[\bar{x} g(\bar{x}, \bar{q}^2) \frac{2\bar{q}^2 - |t|}{(2\bar{q}^2)^3}\right]^2, \tag{1.39}$$

where $\Gamma_{ee}^{J/\psi}$ is the partial width of the $J/\psi \to e^+e^-$ decay and $F_N^{2G}(t)$ is the two-gluon form factor of the proton.

Calculations extending beyond the leading $\ln(Q^2)$ approximation have been performed [9] to include the effects of the transverse momentum of the exchanged gluons and quark motion whithin the J/ψ. In this case a set of more complicated Feynman diagrams including the gluon ladder have to be summed up. It turns out that the shape of the $W_{\gamma^* p}$ dependence rather then the normalization is a better discriminator between the different parametrizations of the gluon density of the proton.

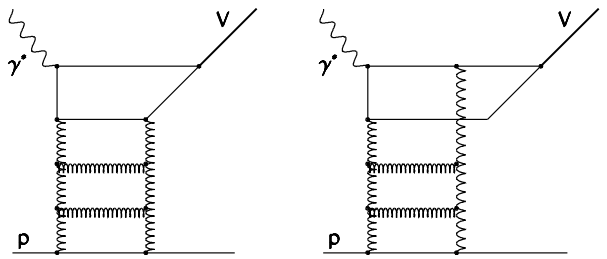

Figure 1.9: Diagrams for the $\gamma^* p \to Vp$ process through gluon ladder exchange

It is worthwhile to note that this model is very promising for future extraction of the gluon density in the proton, $xg(x, Q^2)$. Indeed, the dependence of the cross section on the square of the gluon density should allow $xg(x, Q^2)$ extraction with a high sensitivity, provided that a full NLO calculation is available.

1.6 Decay Angular Distributions

The study of the angular distribution of the vector meson decay products is usually done in the s-channel helicity frame [10]. In this frame, shown in Fig. 1.10, the vector meson direction in the $\gamma^* p$ frame is taken as the quantization axis and, in the case of two-body decay, the direction of one of the particles in the rest frame of the vector meson is used to calculate θ_h, ϕ_h. In the case of a three-body decay, the normal to the decay plane is used to define the decay angles.

The angle Φ between the vector meson production plane and the electron scattering plane in the γp rest frame is also used. The full decay angular distribution is usually expressed in terms of $\cos\theta_h$, ϕ_h, Φ (Fig. 1.10). In the case where the electron beam is not longitudinally polarized, the electron beam energy is not varied, and the s-channel helicity conservation (SCHC) is assumed to apply, the decay distribution reduces to:

$$\begin{aligned} W\left(\cos\theta_h, \phi_h\right) &= \frac{3}{4\pi}\left[\frac{1}{2}\left(1 - 3r_{00}^{04}\right)\cos^2\theta_h \right. \\ &\left. + \sqrt{2}\mathrm{Re}(r_{10}^{04})\sin 2\phi_h \cos\theta_h + r_{1-1}^{04}\sin^2\theta_h \cos 2\phi_h\right] \end{aligned} \tag{1.40}$$

where r_{00}^{04}, $\mathrm{Re}(r_{10}^{04})$ and r_{1-1}^{04} are the non-zero combinations of the vector meson spin density matrix elements. r_{00}^{04} gives the probability that the vector meson is produced in a helicity zero state, the element $\mathrm{Re}(r_{10}^{04})$ corresponds to the interference between helicity non-flip and single flip amplitudes, while r_{1-1}^{04} measures the interference helicity non-flip and double flip amplitudes. If the production process is consistent with SCHC, then both r_{10}^{04} and r_{1-1}^{04} are zero and R, the ratio of longitudinal to trasnverse photon cross section can be related to r_{00}^{04}

$$R = \frac{\sigma_L}{\sigma_T} = \frac{1}{\epsilon}\left(\frac{r_{00}^{04}}{1 - r_{00}^{04}}\right) \tag{1.41}$$

where ϵ is the ratio of longitudinal to transverse photon fluxes.

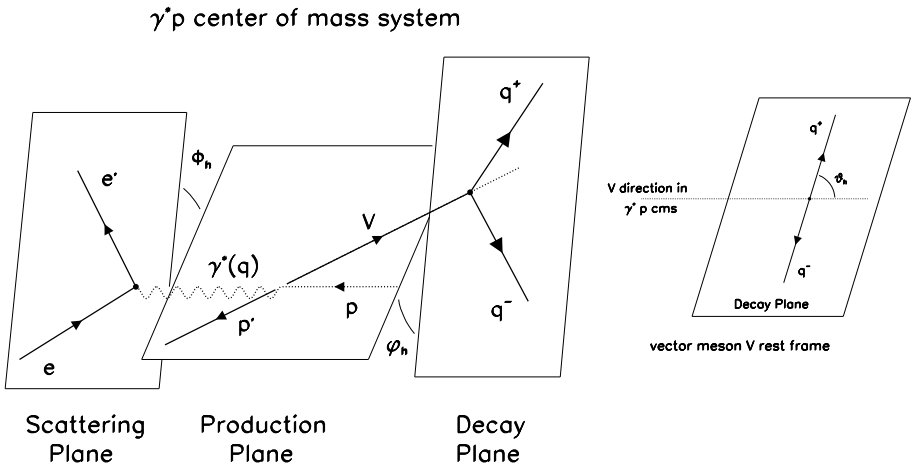

Figure 1.10: The decay angles in the vector meson helicity frame.

Physics Process	Generator
Elastic J/ψ production: $\gamma_e p \to eJ/\psi p$	DIPSI
Proton Dissociative process: $\gamma_e p \to J/\psi X$	EPSOFT
Elastic Non resonant production $\gamma_e\gamma_p \to \mu^+\mu^-$	LPAIR
Elastic ψ' production: $\gamma_e p \to e\psi' p$	DIPSI

Table 1.1: The list of the main physics generators used in the analysis and the corresponding processes simulated.

1.7 Monte Carlo Generators

In this chapter the Monte Carlo generators which have been used to simulate, respectively, the elastic, the proton dissociative and the non resonant $\gamma\gamma \to \mu^+\mu^-$ Bethe-Heitler process are briefly described.

1.7.1 DIPSI

The Monte Carlo generator DIPSI [11] was specifically designed to simulate events with elastic vector meson production ($ep \to epV$). The generator is based on the Ryskin model [8] described in section 1.5.2: this model assumes that the exchanged virtual photon fluctuates into a $q\bar{q}$ pair, which then interacts with the proton. The momentum required to produce an on shell meson is supplied by a pomeron exchange. This is described as a gluon ladder evaluated in the leading logarithm approximation of QCD. The parameters of the model are the strong coupling constant α_s, the two-gluon form factor of the proton $F_N^{2G}(t)$ and the gluon momentum density in the proton. Once

these are chosen, the dependence on W and t is fixed. In this model the cross section is proportional to $\left[\alpha\bar{x}g(\bar{x},\bar{q}^2)\right]^2$ where the variables $\bar{x}$, $\bar{q}^2$ are given by 1.38: which can be interpreted as the effective momentum fraction and scale at which the gluon density is probed respectively. For J/ψ photoproduction, $\bar{q}^2$ takes a value of approximately 2.5 GeV^2. The function $F_N^{2G}(t)$ is approximated by an exponential function $e^{-b|t|}$. The model also assumes that the interaction with the proton conserves s-channel helicity.

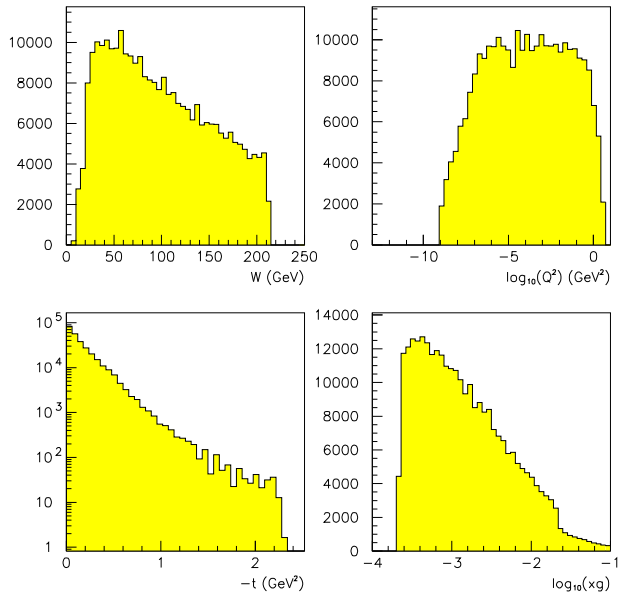

Figure 1.11: Distribution of the main kinematic variables from the DIPSI Monte Carlo generator. The center mass energy in the γ^*p frame W_{γ^*p}, the photon virtuality Q^2, and the four momentum exchanged at the proton vertex t.

In Fig. 1.11 the main kinematic variables are plotted as obtained directly from the generator for ep interactions of 820 GeV protons and 27.5 GeV positrons in the photoproduction regime ($Q^2 < 4$ GeV) and for $20 < W_{\gamma p} < 200$ GeV. The t distribution is parametrized as $e^{-b|t|}$ with $b = 5.3$ GeV^{-2}. The angles and momenta distribution of the J/ψ and of the decay muons are plotted in Fig. 1.12 The J/ψ is most likely produced at small angles, close to the beam pipe. The angular distribution of the muons is much smoother with an average momentum around 2 GeV. For this analysis events were generated using the MRSA$'$ [12]. parametrization of the proton parton densities. Both the b slope as well as the W dependence (W^δ) where retuned to the data distributions in the last part of the analisys. Due to the uncertainties in the cross section calculations, the Monte Carlo provides non normalized distributions.

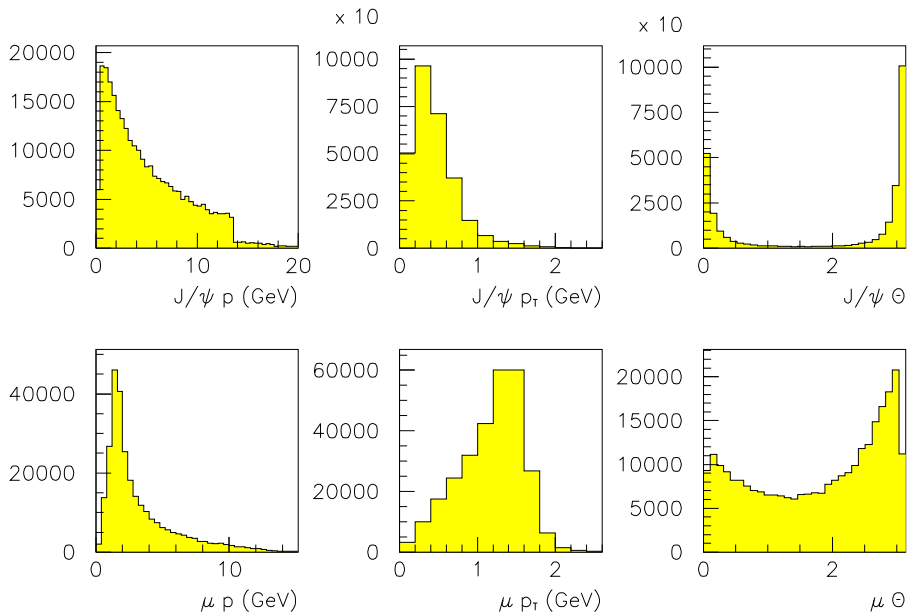

Figure 1.12: Momentum and polar angle distribution for the J/ψ meson and the decay muons from the DIPSI generator. The direction $\theta = 0$ is defined along the outgoing proton beam.

1.7.2 EPSOFT

EPSOFT [13] is a Monte Carlo program for simulating soft diffractive and non diffractive photon-proton collision. It has been developed in the framework of HERWIG and tuned specifically for photoproduction in diffractive events.

In this thesis EPSOFT was used to simulate the proton diffractive dissociation process shown in Fig. 1.6, to estimate and subtract the contribution of this background process to the elastic sample. The cross section for this process is described by the following formula:

$$\frac{d\sigma(\gamma p \to VX)}{dt dM_X^2} = \sigma_{ALLM}(\gamma p) \cdot C \cdot \frac{e^{-b_d \cdot |t|}}{(M_X^2 + Q^2 - M_V^2)^{1+\epsilon}} \tag{1.42}$$

where M_X is the mass of the proton dissociating system.

The simulation of the hadronization of the dissociative system includes a parametrization of the resonance spectrum. In Fig. 1.13 the main kinematic variables are plotted as obtained directly from the generator. The gluon density is assumed to follow the ALLM parametrization. The t distribution is parametrized as $e^{-b_d|t|}$ with $b = 1.5$ GeV^{-2} i.e. a smother t dependence when compared to the the elastic process.

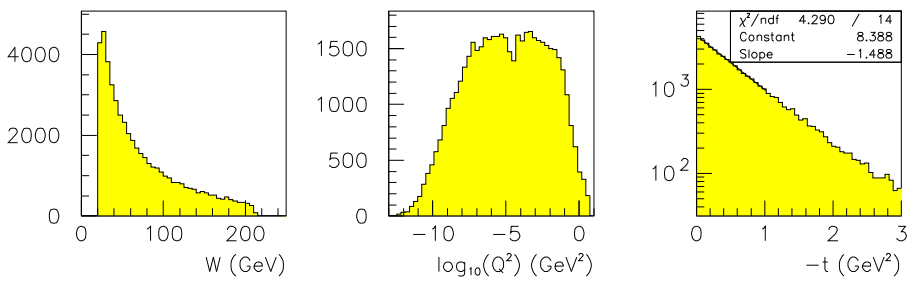

Figure 1.13: Distribution of the main kinematic variables from the EPSOFT Monte Carlo generator. The center mass energy in the $\gamma^* p$ frame $W_{\gamma^* p}$, the photon virtuality Q^2, the four momentum exchanged at the proton vertex t.

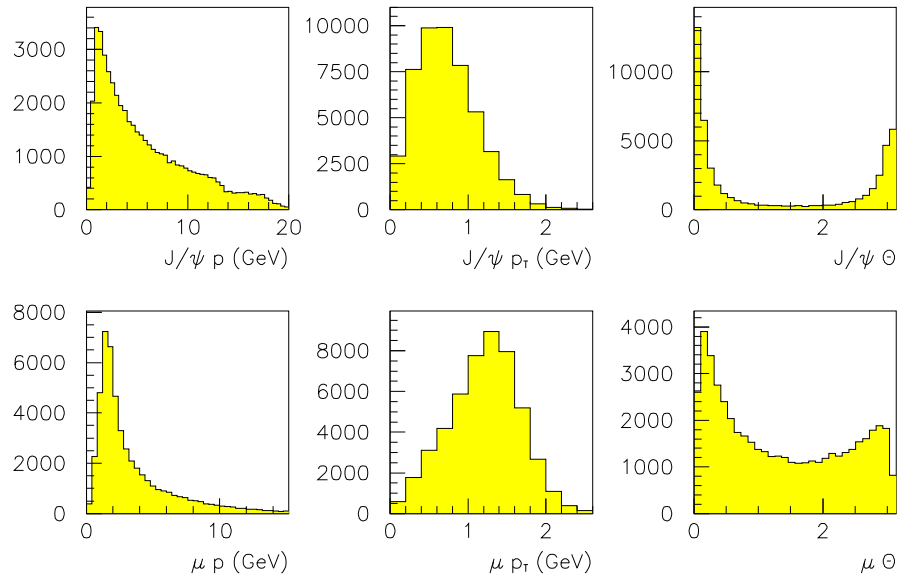

Figure 1.14: Momentum and polar angle distribution for the J/ψ meson and the decay muons from the EPSOFT generator.

1.7.3 LPAIR

The LPAIR Monte Carlo was designed to simulate lepton pair production via two photon process in e^+e^-, $p\bar{p}$ and $e^{\pm}p$ interactions in the ZEUS environment[14]. The

corresponding process diagram is shown in Fig. 1.15. The two exchanged photons in the t-channel interact and produce a pair of leptons. This program, based on a generator by Vermaseren [15], was used both for simulation of elastic and proton dissociative lepton pair production. A plot of the the kinematic quantities as obtained directly from the generator is shown in Fig. 1.16.

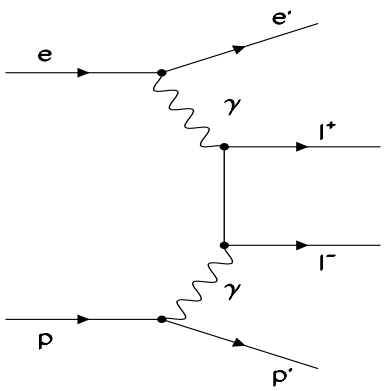

Figure 1.15: The lepton pair production by $\gamma\gamma$ fusion $\gamma_e\gamma_p \rightarrow \mu^+\mu^-$ also known as Bethe-Heitler process.

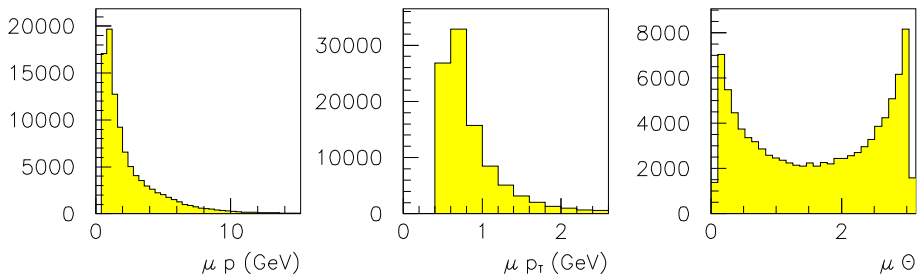

Figure 1.16: Momentum and polar angle distribution for the produced muons from the LPAIR generator. The direction $\theta = 0$ is defined along the outgoing proton beam.

Chapter 2

HERA and the ZEUS Detector

2.1 The HERA Collider

HERA (Hadron Elektron Ring Anlage) [20] [21] is the first lepton proton collider. It has been designed to accelerate electrons or positrons and protons to energies of 30 GeV and up to 1 TeV, respectively. It is located in Hamburg, crossing the DESY laboratory site where a 10-25 m underground tunnel of 6.34 km circumference houses two separate rings for leptons and protons. Accelerated using conventional and superconducting magnets, the two beams are brought into collision at zero crossing angle at two interaction points around the ring. In Fig. 2.1 the layout of HERA is shown along with the location of the different detector halls and the pre-accelerators chain. The two collider experiments,

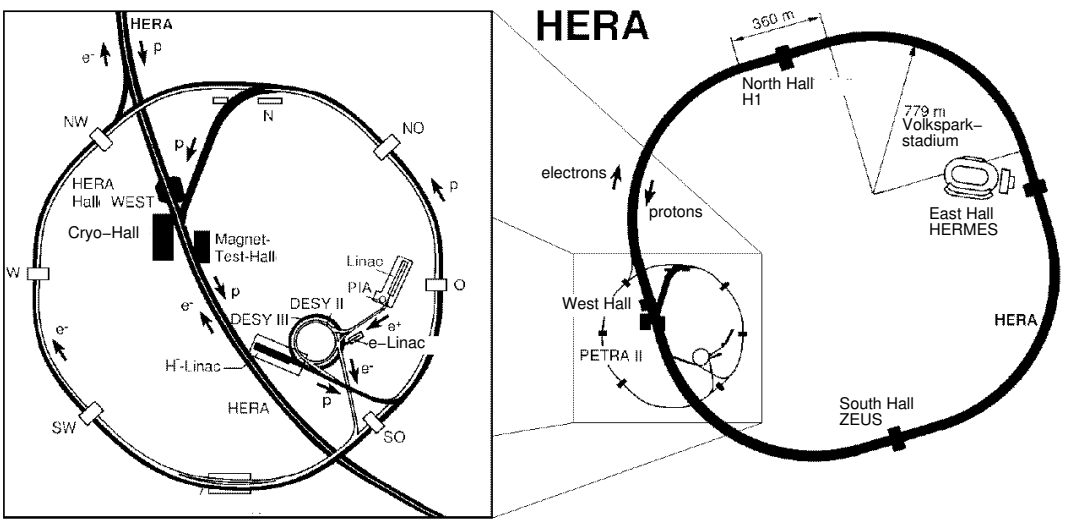

Figure 2.1: The HERA collider and the injection system.

H1 and ZEUS, are located in the north and south hall respectively, while the fixed target experiments HERMES and HERA-B are located in the remaining east and west

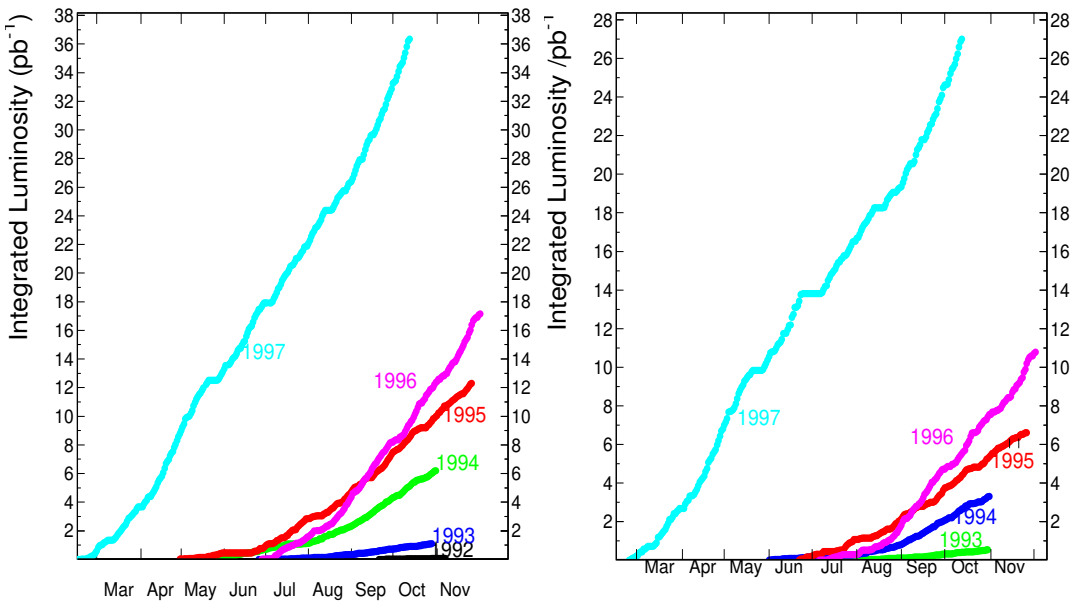

Figure 2.2: The integrated luminosity as delivered by HERA in each operating year and the part gated by the ZEUS Experiment and used for physics analysis.

halls. HERMES is designed to study the spin structure of the nucleon by scattering longitudinally polarised photons off polarised targets of hydrogen, deuterium or ^{3}He. HERA-B is designed to investigate CP violation in the $B^o\bar{B}^o$ system by means of beam halo protons scattering off wire targets inserted very close to the beam.

Positrons and protons are grouped and accelerated in bunches of particles which fill the 220 buckets of the HERA machine and cross every 96 ns the interaction points. Not all bunches are usually filled with particles: unpaired bunches, also called pilot-bunches, and empty bunches are used for the estimation of the beam related background and cosmics contamination respectively.

The HERA accelerator was commissioned in 1991 and the first *ep* interactions were observed in the H1 and ZEUS experiments during spring 1992. The plot of figure 2.2 shows the luminosity delivered by HERA for each year up to end of 1997 and the part taken by the ZEUS experiment.

This thesis makes use of 38 pb^{-1} of data collected in 1996-7. During this period, the machine operated as a positron proton collider with energies of 27.5 GeV and 820 GeV respectively, corresponding to a centre-of-mass energy $\sqrt{s} = 300$ GeV. The operating conditions of the HERA collider during this data taking period are summarised in table 2.1.

HERA parameters	1996-97	
	positrons	protons
Energy (GeV)	27.52	820
Centre-of-mass energy (GeV)	300	
Specific luminosity ($cm^{-2}s^{-1}mA^{-2}$)	$4.0 \cdot 10^{29}$	
Typical instantaneous luminosity ($cm^{-2}s^{-1}$)	$6.0 \cdot 10^{30}$	
Integrated luminosity (pb^{-1})	16+21	
Injection energy (GeV)	11	40
Typical beam currents (mA)	30	60
Energy loss per turn (MeV)	127	$1.4 \cdot 10^{-10}$
Number of bunches (paired+pilot)	173+15	173+7
Bunch crossing time	96ns	

Table 2.1: HERA design parameters performance during the 1996-97 running period.

2.2 The ZEUS Detector

The ZEUS Collaboration includes more than 450 physicists and a comparable number of technicians coming from 51 institutes distributed in 11 countries. This large Collaboration built the ZEUS detector, a multi-purpose hermetic detector with a solid angle coverage greater than 99.6%, located in the south experimental hall of HERA. A detailed description of the ZEUS detector components can be found in the original technical proposal [22] or in the most recent status report [23], since several detector upgrades have taken place after the assembly, completed in autumn 1991.

A brief outline of the detector components is given below. The detector components which are essential for the present analysis will be discussed in more detail in the following sections.

Before starting the detector description, we define here the coordinate system used in ZEUS. It is a right-handed orthogonal system with the origin at the interaction point (IP) and the z-axis pointing along the direction of the proton beam; the x-axis points towards the centre of the HERA ring and the y-axis is directed upwards. A polar coordinate system is also used, with the radius $\rho = \sqrt{x^2 + y^2}$, the azimuthal angle ϕ measured with respect to the x-axis, and the polar angle θ defined with respect to the proton beam direction (the proton beam polar angle is 0^o, whereas the electron beam polar angle is 180^o).

A view of the main detector in the $\rho\phi$ plane is shown in figure 2.3. Starting from the centre, where the nominal interaction point is, the charged particles tracking system begins with the Central Tracking Detector (CTD). Around the CTD is placed a thin superconducting solenoid providing a magnetic field of 1.43 T. Forward and rear tracking chambers (FTD and RTD) provide extra tracking information and particle identification in the forward and rear directions - i.e. following the proton and the electron beams respectively from the IP - (cf. Fig. 2.4 for a cross section of ZEUS along the beam direction). A high resolution uranium calorimeter (CAL) surrounds

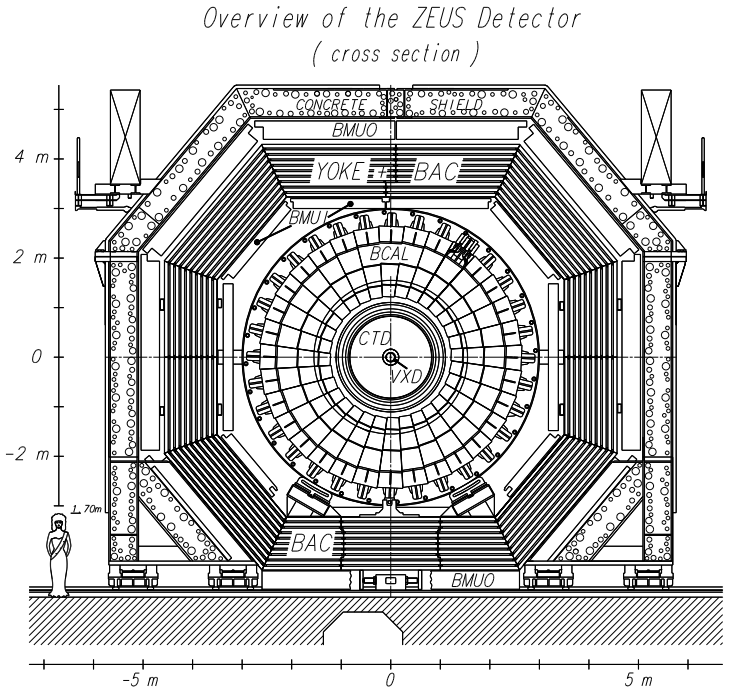

Figure 2.3: Cross Section of the ZEUS detector in the $\rho - \phi$ plane, perpendicular to the beam direction.

the tracking chambers; it is divided into three sections: the FCAL in the forward direction, the RCAL in the rear section and the BCAL, a barrel section in the central region. A Small Angle Rear Tracking Detector (SRTD) is situated behind the RTD chambers covering the face of RCAL down to a radius of about 34 cm around the beam pipe hole. A backing calorimeter (BAC), used to measure the energy of late-showering particles, is placed inside the iron yoke which also serves as return path for the magnetic flux. The muon detection system is divided into three sections: the barrel (BMUON) and rear (RMUON) muon detectors and the Forward Muon Spectrometer (FMUO). Downstream of the main detector, at $z = -7.5$ m, an iron/scintillator VETOWALL is used to reject beam-related background. A small lead/scintillator counter (C5) is located around the beam pipe at $z = -3.15$ m and is used to monitor the synchrotron radiation from the electron beam and to measure the timing and the longitudinal structure of the proton and electron bunches.

Even if the ZEUS apparatus covers most of the solid angle, some particles produced in ep collisions escape in the forward and rear beam-pipe holes. Some detectors have been therefore placed along the beam-lines, upstream and downstream the IP, in order to detect along the proton and the electron beam directions particles scattered at very small angles. The so-called forward detectors are located between $z = +20$ m and $z = +106$ m and allow to measure protons, with the leading proton spectrometer (LPS), and neutrons, with the forward neutron calorimeter (FNC), which are scattered with angles less than few mrad. The Proton Remnant Tagger (PRT) is made of two sets of scintillator counters surrounding the beam-pipe at $z = 5.1$ m and $z = 24$ m. Upstream

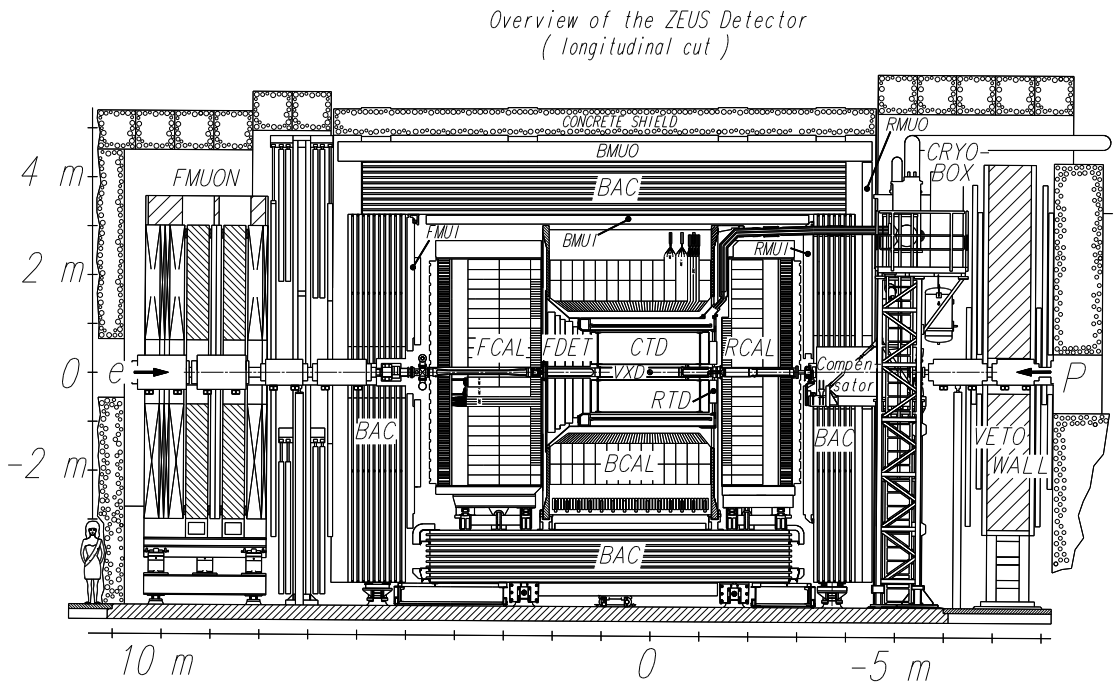

Figure 2.4: Cross Section of the ZEUS detector along the beam direction.

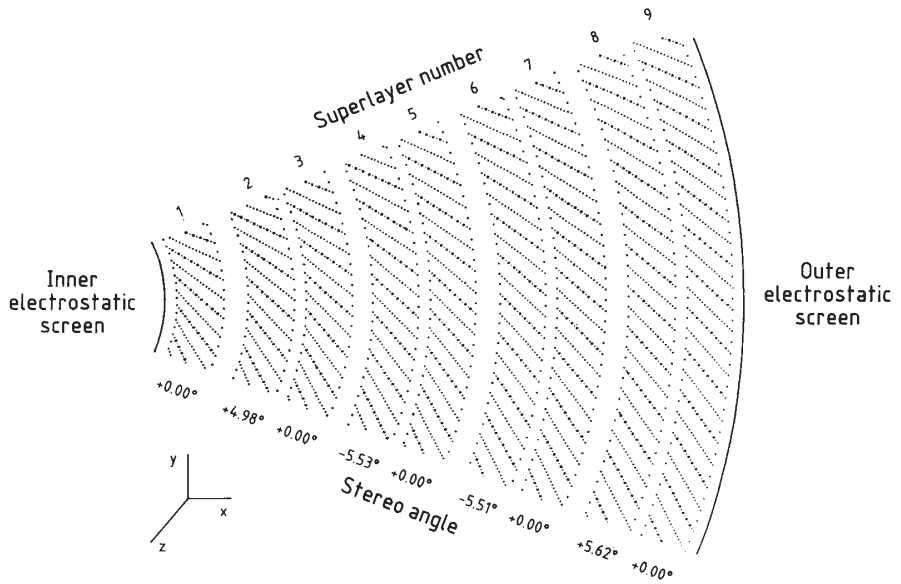

Figure 2.5: Layout of a CTD octant. The superlayers are numbered and the stereo angles of their sense wires are indicated.

the IP, following the electron beam direction, two lead/scintillator calorimeters have been installed at $z = -35$ m and $z = -104$ m; they are part of the luminosity monitor (LUMI) and have been designed to measure small angle outgoing electrons and photons, respectively.

The high beam crossing rate of 10 MHz is determined by the short interval of 96 ns between the bunch crossings; a three-level trigger system is used to reduce the rate to a few Hz which can be written to tape.

2.3 The Central Tracking Detector

The central tracking detector (CTD) [24] measures the trajectory of charged particles and allows to reconstruct their momenta with a high precision; it also allows to estimate the energy loss dE/dx which is used for particle identification. The CTD is a cylindrical drift chamber filled with a gas mixture of argon, CO_2 and ethane, with an inner and outer radius of 18.2 cm and 79.4 cm respectively and a length of 205 cm. It covers the polar angle range $15^o < \theta < 164^o$ and consists of 72 radial layers grouped into 9 superlayers: the odd superlayers have wires parallel to the beam axis while the even superlayers have small angle ($\pm 5^o$) stereo wires allowing the determination of the z-position of the hits. Figure 2.5 shows the layout of one of the CTD octants. The three inner axial layers are equipped with z-by-timing electronics [25] which determine the z-position of a hit from the difference in arrival times of a pulse at both ends of the chamber. This is used for trigger purposes.

The single hit spatial resolution of the CTD is around 180 μm in the $\rho - \phi$ plane

and this corresponds to a transverse momentum resolution for full length tracks of:

$$\frac{\Delta p_t}{p_t} = 0.0058 p_t \oplus 0.0065 \oplus \frac{0.0014}{p_t} \ ,$$

where $\oplus$ indicates the sum in quadrature and p_t is measured in GeV.

The resolution on the z-vertex determination is better than 2 mm for medium and high multiplicity events.

2.4 The Uranium Calorimeter

The ZEUS uranium-scintillator compensating calorimeter (CAL) is an essential component for the reconstruction of the final state in ep collisions. The CAL is a sampling calorimeter consisting of sandwiched layers of depleted uranium[1] and plastic scintillator[2] whose thickness[3] is chosen in order to have an equal response to hadrons and electrons over a wide range of energies. The energy resolution, measured under test beam conditions, is

$$\frac{\sigma(E)}{E} = \frac{35\%}{\sqrt{E}} \oplus 2\%$$

for hadrons, and

$$\frac{\sigma(E)}{E} = \frac{18\%}{\sqrt{E}} \oplus 1\%$$

for electrons, with the energy E measured in GeV.

The ZEUS Calorimeter is divided into three main parts covering different angular regions: the forward FCAL, the barrel BCAL and rear RCAL. The calorimeter covers more than 99.6% of the total solid angle, with the exceptions of 20 cm $\times$ 20 cm holes, located in the centre of FCAL and RCAL, which are occupied by the beam-pipe. The three calorimeter sections are divided into vertical (FCAL and RCAL) or radial (BCAL) modules which are subdivided into towers with transverse dimensions of approximately 20 cm $\times$ 20 cm. Figure 2.6 shows an isometric view of an FCAL module. Each tower is segmented longitudinally into an inner electromagnetic section (EMC) and two (or one for RCAL) outer hadronic sections (HAC1 and HAC2) which are divided transversely into cells. The typical size of the EMC cells is 5 cm $\times$ 20 cm (FCAL and BCAL) or 10 cm $\times$ 20 cm (RCAL). The cells of the HAC section are somewhat larger with typical transverse dimensions of 20 cm $\times$ 20 cm. The depth of the CAL sections is reported in table 2.2 together with some additional detector parameters.

Each calorimeter cell is read-out on two opposite sides by photomultiplier tubes (PMTs) coupled to the scintillator via wavelength-shifters bars. The energy measurement is independent of the position of the particle within the cell since the energies of both PMTs are summed; the comparison of the signals of the two PMTs allows to determine the impact point of the particle within a cell.

[1] An alloy of 98.4% U^{238}, 1.4%Nb and less than 0.2%U^{235}.
[2] SCSN-38
[3] 2.6 mm scintillator and 3.3 mm ($\sim$ 1 X_0) uranium.

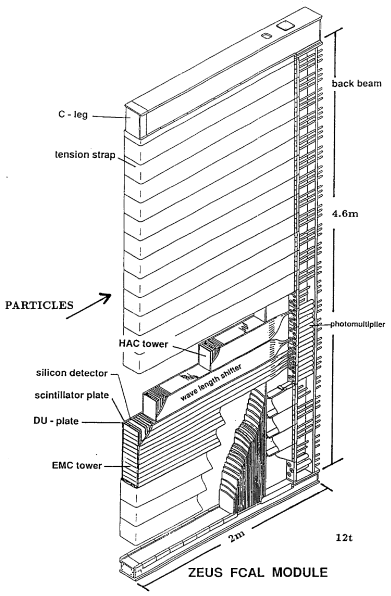

Figure 2.6: Isometric view of an FCAL module. The 20 cm $\times$ 20 cm towers, with the EMC and HAC sections, are shown.

	FCAL	BCAL	RCAL
θ-range	2.2^o —39.9^o	36.7^o —129.1^o	128.1^o —176.5^o
η-range	-4.0 — -1.0	-1.1 — 0.74	0.72 — 3.49
radiation length X_0	25.9	24.6	24.3
absorbtion length λ	7	5	4

Table 2.2: CAL angular acceptance and longitudinal depth.

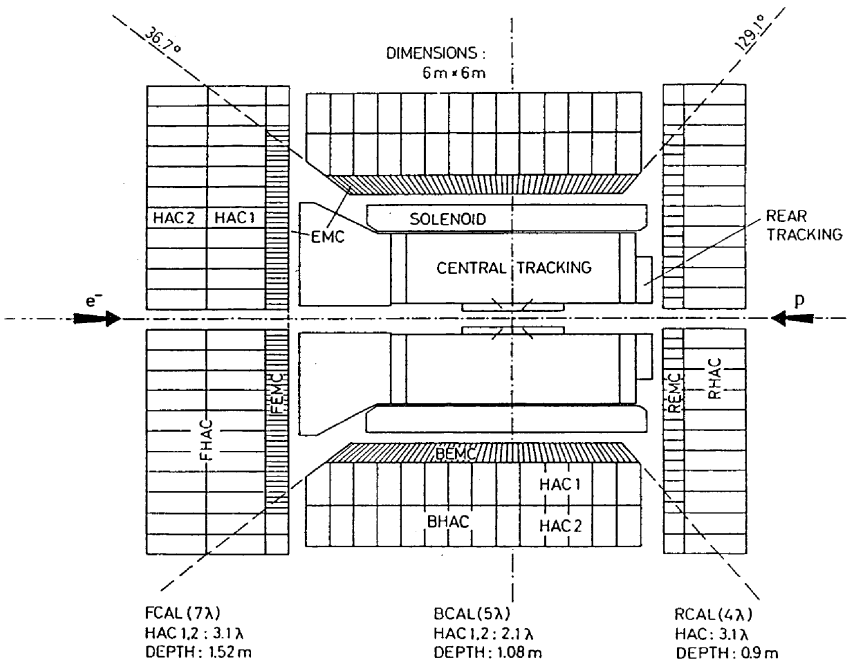

Figure 2.7: ρz view of the three parts of the Calorimeter and it's division into EMC and HAC cells.

The calibration of the calorimeter is performed using the natural radioactivity of the ^{238}U which provides a constant reference signal. The PMTs are calibrated using light emission of known intensity from LEDs.

The calorimeter provides timing information with a resolution better than 1 ns for energy deposits greater than 4.5 GeV.

2.5 The Forward Muon Spectrometer

Muon detection in the forward region is crucial at HERA where the kinematics of important physical phenomena as the production of heavy quarks or other rare events implies small angle production. In the region of small polar angle, where the resolution of the other detectors becomes worse the Forward Muon Spectrometer can provide an independent trigger and a precise momentum measurement up to 100 GeV with a resolution of 25% for high momentum muons.

The FMUON detector as shown in Fig. 2.8 is composed of the following components:

- a system of four Limited Streamer Tubes trigger planes (LT1 ÷ LT4) with ρ (radial strips) and ϕ (longitudinal strips) digital readout;
- two coverage planes of limited streamer tubes with digital (ρ,ϕ) and analog(ρ) read-out (LW1,LW2) in the large polar angle region;
- four planes of drift chambers (DC1 ÷ DC4)

- two large iron magnets of toroidal shape providing a magnetic field of 1.7 Tesla for the momentum separation and measurement.

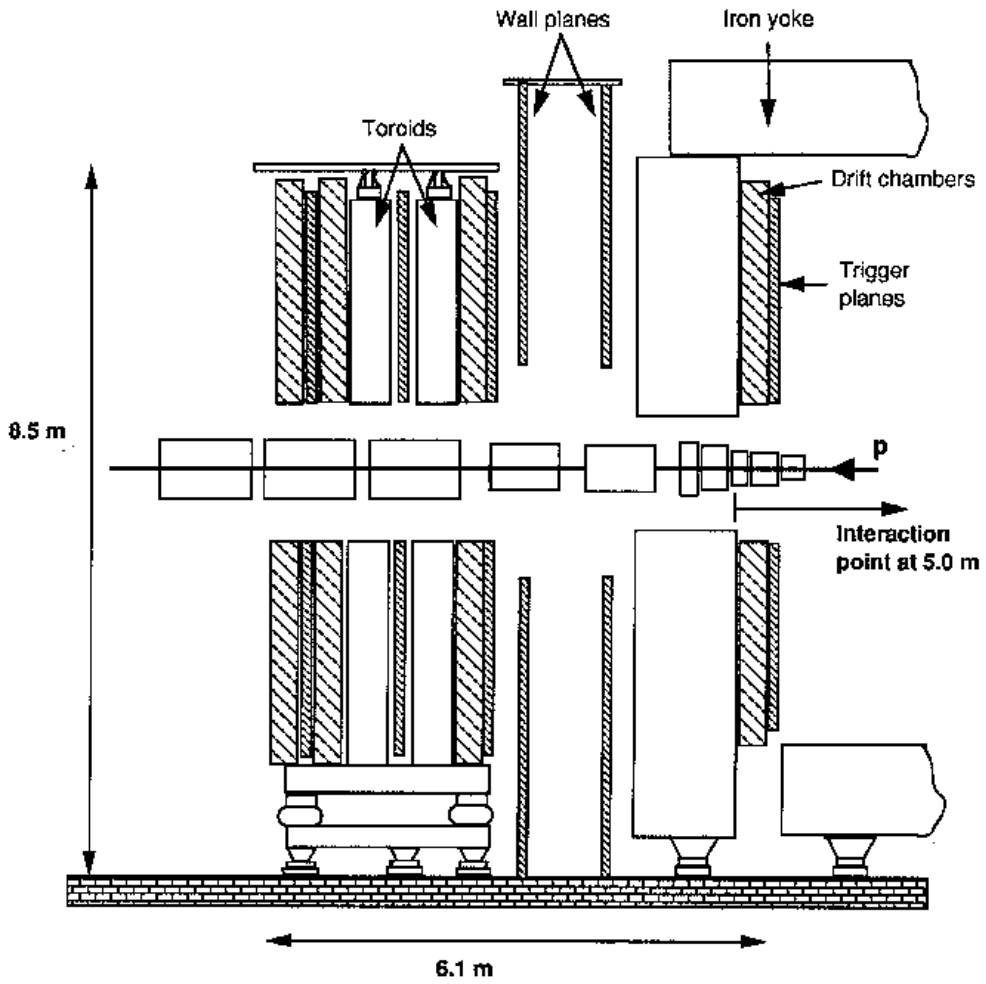

Figure 2.8: The Forward Muon Spectrometer

2.5.1 The LST planes and the Limited Streamer Regime

Detectors working in the limited streamer regime [27] make use of wires of larger diameter (tipically 100 μm) when compared to proportional chambers, allowing higher anode voltages (around 4600 Volts). As a consequence the region with a field higher than the 10 KV/cm, required to start the multiplication, is in this case much wider extending up to 1 mm from the wire surface and providing a higher gain, up to 10^8. The dipole field created by the charge is so intense to balance the original field favouring the

recombination of electrons and ion with subsequent emission of isotropic photons capable of creating new ions pairs at several microns distance. These secondary electrons may generate new cascades in particular at the borders of the primary multiplication region enhanced by the spatial charge, forming a radial fuse of charge called streamer. The streamer propagates in the direction of the incoming primary electrons several millimeters towards the cathode.

The choice of the absorbing gas mixture as well as the cathode material are important items to be considered during the design phase.

The cathode is usually an insulator covered on the inner surface by a resistive paint that favours the physical separation of the discharge device from the detector itself. The tube resistivity measured in ohm per square ($\Omega/\Box$) may vary from 10 k$\Omega/\Box$ to a maximum of 10M$\Omega/\Box$. Depending on the desired multiplicity and width of the signal as well as the read-out system, a lower or higher resistivity may be chosen. For the FMUON LT planes, read-out by a digital system, a lower resistivity was chosen. For the large angle planes (LW) as well as for the Barrel and Rear Muon Chambers (see next topic) being read-out by an analog system, a higher value was used ($10-15k\Omega/\Box$).

The gas mixture used is Ar:CO_2:C_4H_{10} (3%:88%:9% respectively).

In figure 2.9 a drawing of one LST plane (LT1) is shown. Each plane is composed by two of these layers with double ρ, ϕ read-out logically *OR*-ed to minimize inefficiencies.

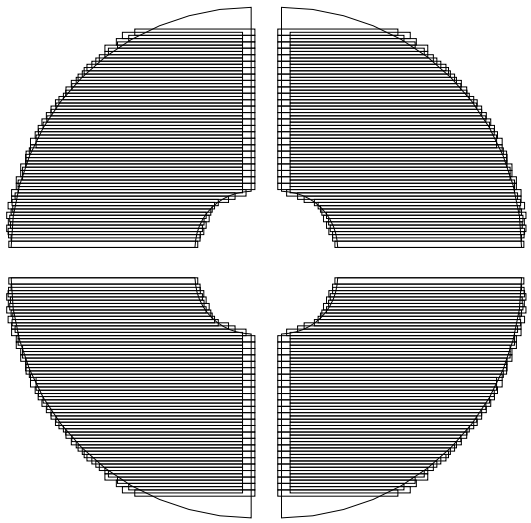

Figure 2.9: Drawing of the limited streamer tubes layout of the FMUON LT1 plane.

2.5.2 The Drift Chambers

Four planes of drift chambers (DC1 $\div$ DC4) provide an accurate track reconstruction and momentum resolution for high energy traversing muons. Each plane is made of eight chambers of trapezoidal shape that in the case of the outer planes are partially overlapping for an optimal coverage around the ϕ angle. Each chamber is subdivided

into 32 (31 for DC1) cells with 4 sense wires each for pseudo ρ and $d\rho/dz$ measurements. The intrinsic resolution of the system is 200μm.

2.5.3 The FMUON Trigger System

The FMUON read-out[29] is subdivided over the azimuthal angle into eight octants. The $\rho\phi$ strip information of the digital read-out of the 6 LST planes (LT1-4, LW1-2) is used to build an internal trigger by means of hardware programmable gatearrays. Depending on the polar angle, a $\rho\phi$ match between an inner and an outer plane compatible with a traversing muon, as well the presence of a hit in the intermediate planes is required.

For elastic events, characterized by lower energy muons ($p \leq 3$GeV) which would not reach the outer part of the spectrometer, a less restrictive trigger based only on the presence of a $\rho\phi$ hit in the inner plane (LT1) is used. Further requirements on the inner tracking and energy deposits in the main calorimeter allow a sufficient background rejection while keeping a high efficiency in the elastic channel.

2.6 The Barrel and Rear Muon Detectors

Muon detection in the barrel and rear region is also done using limited streamer tubes but with a different frame design and read-out technology. Both the barrel and rear muon detector are composed of two layers of chambers (BMUI/BMUO) (RMUI/RMUO) placed inside and outside the Iron Yoke. Each chamber (cf. Fig. 2.11) contains two groups, of two layers each, of LST separated by an aluminum honeycomb structure. The use of two layer, shifted by half cell as already mentioned in the FMUON LT case, minimizes inefficiencies due to geometrical design or dead tubes. Attached to each layer of LST is a single plane of read-out strips perpendicular to the wires direction.

The particle detection is done by measuring signals both on the strips and the wires. While wires are read-out by a digital system the strips are read-out by a digital-analog hybrid system specifically designed [4]. This system provides a digital fast-OR of 16 adiacent strips for trigger decision, a digital information for groups of 4 strip for each event as well as an analog measurement strip by strip of the charge in case of muon trigger. The information of the fast-OR as well as the hit on the wires, is used to generate the muon trigger by means of a coincidence matrix programmed to select tracks coming from the interaction point. The spatial resolution obtainable by means of the analog read-out is of 200μm for the strip read-out and of 700μm for the wire read-out.

The structure of the detector allows an accurate measure of the position of the track at the exit of the calorimeter and a momentum evaluation by means of the yoke magnetic field.

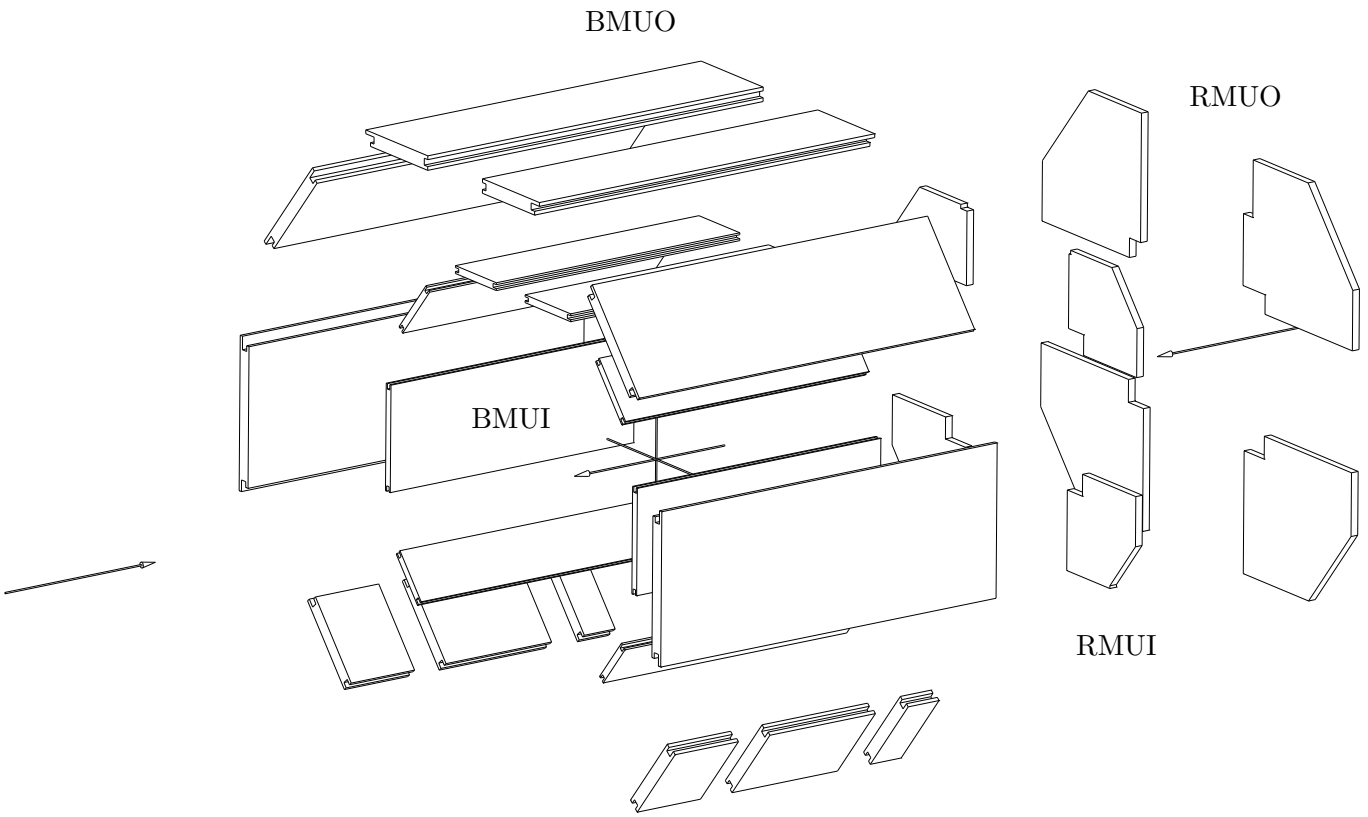

Figure 2.10: three dimensional view of the BMUON and RMUON chambers.

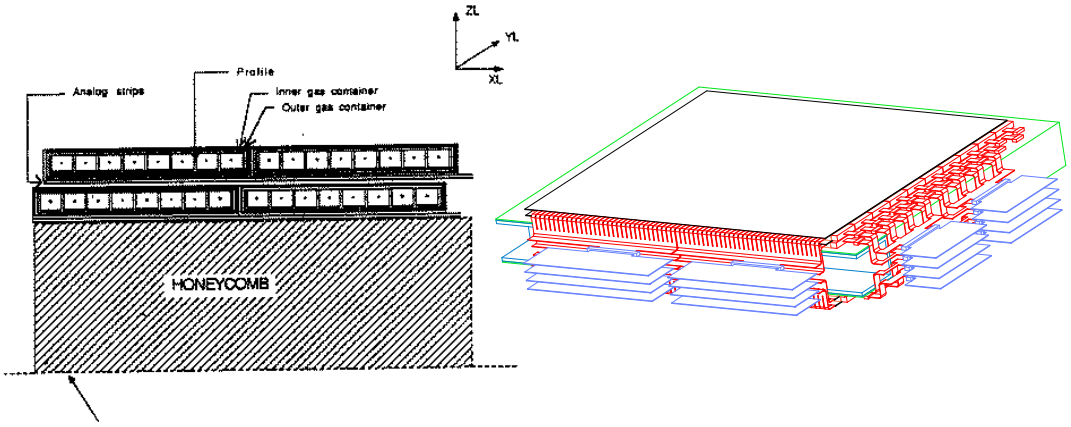

Figure 2.11: Internal structure and external layout of a BMUON chamber

2.7 The Luminosity Monitor

The luminosity measurement is done by measuring the hard bremsstrahlung photons in the bremsstrahlung events ($ep \to ep\gamma$). This process is chosen because of his large cross section and a clean experimental signature. The bremsstrahlung differential cross section is given by the Bethe-Heitler formula:

$$\frac{d\sigma}{dk} = 4\alpha r_e^2 \frac{E'}{kE}\left(\frac{E}{E'} + \frac{E'}{E} - \frac{2}{3}\right)\left(\ln\frac{4E_pEE'}{m_em_pk} - \frac{1}{2}\right) \tag{2.1}$$

where k, E and E' are respectively the energies of the photon, the incoming and outgoing electron. By knowing the acceptance of the detector, the Luminosity $\mathcal{L}$ can be extracted:

$$\frac{dN}{dt} = \mathcal{L} \cdot \sigma. \tag{2.2}$$

The luminosity monitor consists of a photon and an electron calorimeters placed along the beam-line upstream of the interaction point (cf. Fig. 2.12).

The photon detector (LUMI-γ) is a lead/scintillator calorimeter located at $z = -104$ m with a carbon filter $2X_0$ deep, which is used to protect the detector against synchrotron radiation. A Cerenkov detector is located between the filter and the calorimeter and is used to detect possible photon conversions in the filter. Photons radiated at the IP with an angle less than 0.5 mrad with respect to the beam axis travel along the proton beam pipe and leave it at $z = -92$ m, where a copper/beryllium exit window is located, and reach the LUMI-γ.

The electron calorimeter (LUMI-e) is a lead/scintillator sampling calorimeter, $23X_0$ deep, and it is able to measure the position of the tagged electron by means of scintillator

[4]New Streamer Tube Analog Read-out [29] designed by the INFN Padua and Rome group.

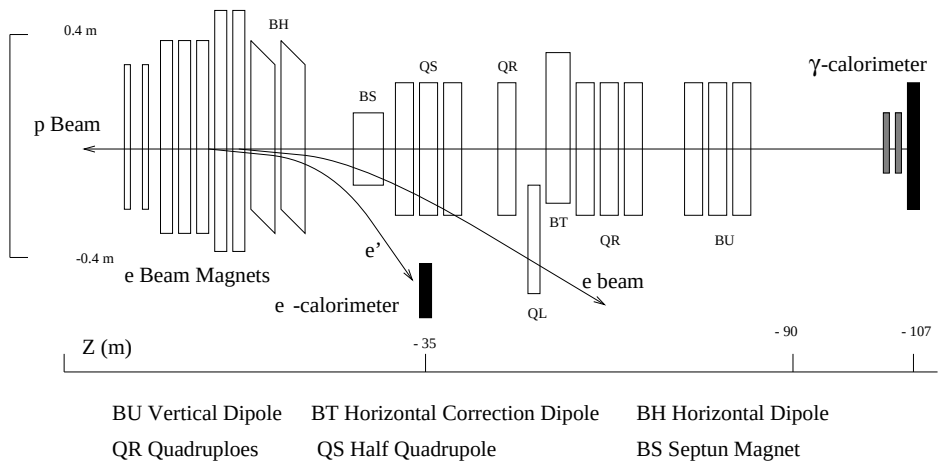

Figure 2.12: The luminosity detectors and the beam-line.

fingers located at a depth of $7X_0$. The geometric acceptance of LUMI-e is determined by the magnets and the beam-pipe apertures: electrons that have lost part of their energy radiating a bremsstrahlung photon, or have been scattered at a very low angle at the IP, are deflected from the nominal beam orbit by the magnetic field of HERA. These electrons leave the beam-pipe through at exit-window located at $z = -27$ m and are detected by the LUMI-e which is located at $z = -35$ m.

Initially the events used for luminosity measurement required the coincidence of a scattered electron in the electron calorimeter and a radiated photon in the photon detector. Due to poor understanding of the electron acceptance only hard bremsstrahlung events assuming $E = E' + k$ were used later.

The LUMI-e calorimeter is used to detect photoproduction events, where the scattering angle is very small, in the interval $10^{-7} < Q^2 < 0.02$ GeV^2.

2.8 The Proton Remnant Tagger

The purpose of the PRT is to detect charged particles emitted at small angles that escape the central detector through the forward beam pipe. The detection of these particles allows to distinguish events with an elastically scattered proton from those in which the proton dissociates.

The layout of the detector, consisting of two stations (PRT1, PRT2), is shown in Fig. 2.13. The PRT1, located at $z = +5.15$ m, consists of two pairs of scintillation counters covering the polar angle range $6 < \theta < 26$ mrad. Each scintillator plate has an area of 26×15 cm, a thickness of 2.6 mm and is shielded against electron syncrotron radiation. Five other pairs of counters, known as PRT2, are placed further downstream, one at $z = +23.1$ m and four at $z = +24.4$ m. These counters provide a polar angle coverage of $1.5 < \theta < 8$ mrad. The scintillators, which are 10 mm thick, are shielded with several millimeters of lead foils. The light produced in the scintillator plates of all counters is detected by photomultipliers via light guides.

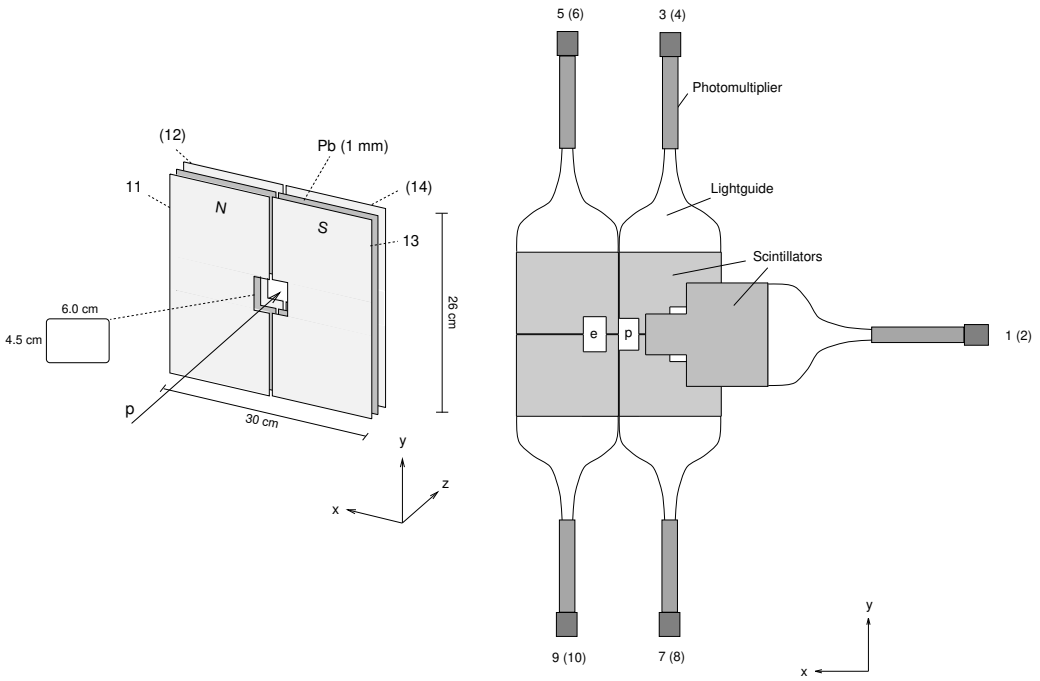

Figure 2.13: Layout of the scintillator counters for the PRT1 (left) and PRT2 (right).

2.9 The Veto Wall and the C5 Counters

The Veto Wall is situated downstream along the proton direction at about $z = -7.5$ m. It consists of an 87 cm thick iron wall, covering completely the rear muon system, instrumented with a layer of scintillation counters mounted on the front and the back surface of the wall. The main purpose of the detector is to protect the central detector against beam halo particles accompanying the proton beam by absorbing them. Particles that penetrate through the wall are recognized by the timing onformation of the scintillators and rejected at First Level Trigger. The C5 counter, is a set of scintillation counters placed very close to the beam pipe at $z = -3.15$ m in corrispondence of the C5 proton quadrupole and is named accordingly. It is composed of two pairs of scintillator plates (10×5 cm^2 of active area) separated by a lead foil. The C5 counter measures the rate and arrival times of the halo particles accompanying both beams and is used as a monitor for bunch profiles and background rates. Proton beam halo is rejected the same way as for the Veto Wall.

2.10 The ZEUS Trigger and Data Acquisition Systems

The HERA bunch crossing time of 96 ns corresponds to the very high beam crossing frequency of about 10 MHz. The interaction rate is dominated by background coming from the interactions of the proton beam with residual gas in the beam pipe or with the beam collimators before the IP; this rate is of the order of a few hundred kHz, while the rate of physics events written on tape is of the order of several Hz.

The ZEUS three-level trigger system [32] and the data acquisition system [33] have

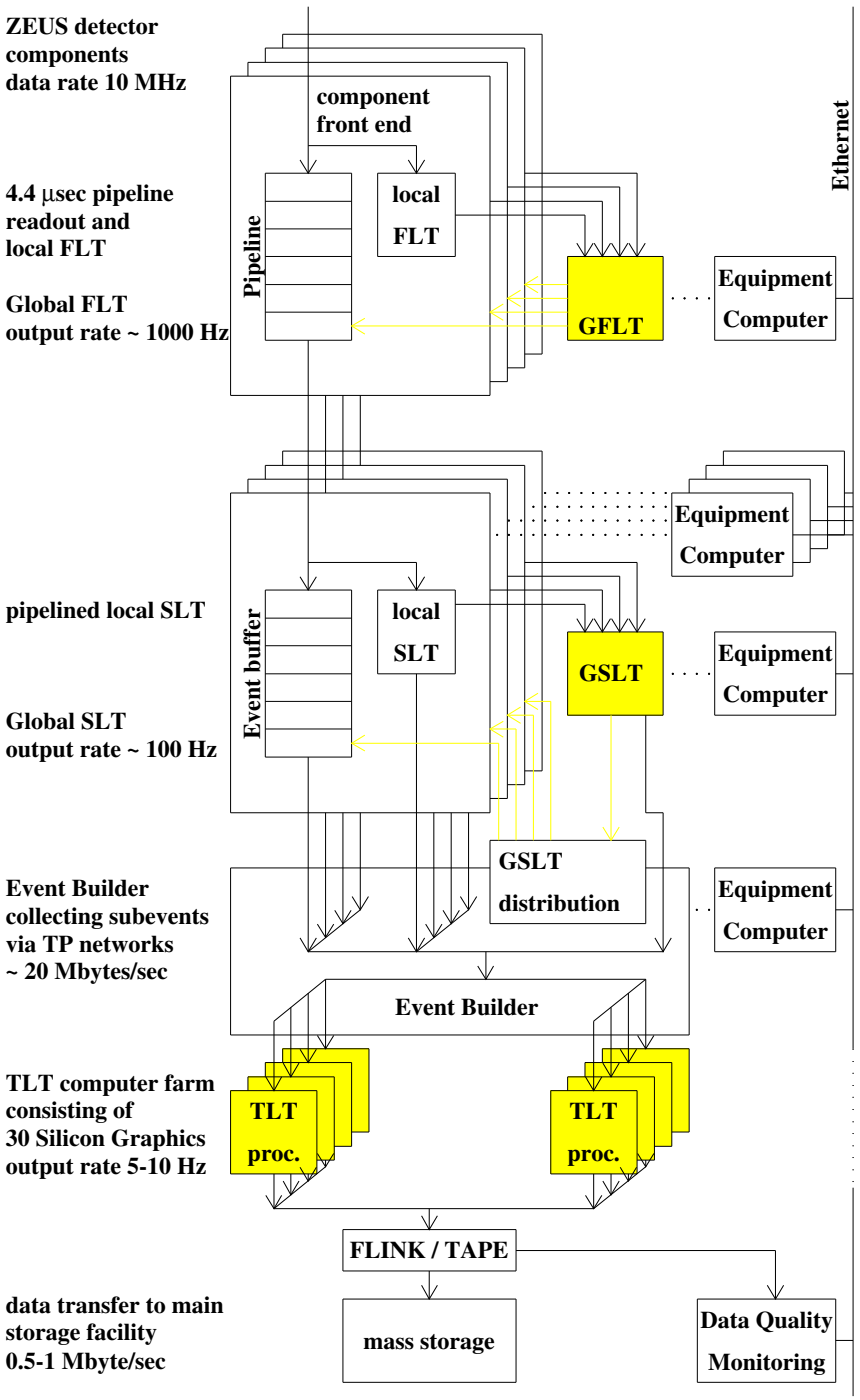

Figure 2.14: ZEUS Trigger system.

been designed to reduce the initial interaction rate by suppressing background events and applying selection filters for accepting interesting events while inducing a minimum dead-time. (cf. Fig. 2.14).

At first level (FLT) a programmable hardware trigger has been designed to reduce the rate below 500 Hz, rejecting a huge part of background events.

All the detector components, participating or not to the FLT decision, store the data in a pipeline, while those partecipating make a trigger decision, and send it to the Global First Level Trigger (GFLT) which combines all the single-component information and decides whether to accept or reject the event. The FLT pipeline is 46 crossings deep: 26 are needed by the detector components to produce a decision (2.5 μs), and 20 are used by the GFLT to collect all the information and produce a trigger decision (1.9 μs). The GFLT performs logical operations on the component FLT information and can combine the results in 64 different slots; the basic operations possible are the comparison of a signal with a threshold and the generation of accept/reject bits. When the input rate to the GFLT exceeds the processing rate, the events in excess are lost. The time during which the trigger is anavailable while processing a previous trigger is called dead time. During normal operation, the GFLT dead time is smaller than 1%.

The FLT implements a three-fold veto based on the information of the VETOWALL, C5 counters and the SRTD detector: events with a coincidence in the VETOWALL and C5 are rejected, while the SRTD provides a timing information which is used to reject proton beam-gas events.

The second level trigger (SLT) consists of a set of algorithms running on a transputer network and has been designed to further reduce the rate below 100 Hz. As for the FLT, several detector components have their own SLT processor and give the local decision to the Global Second Level Trigger (GSLT) which takes the final decision whether to accept or reject the event. The time available to the GSLT is about $1 \div 2$ ms and depends on the input rate coming from the GFLT.

At the SLT stage more accurate information is available and more complex rejection algorithms are thus possible. The following filtering methods are used at the SLT:

- **Timing**. The CAL time for an event originating from the IP is zero, by definition. All events which occurred far from the IP release energy in different parts of the CAL; upstream proton beam-gas interactions are thus vetoed by means of time differences among the CAL sections. Isolated cosmic muons are also rejected with the help of timing differences between the upper and lower halves of BCAL.

- **Sparks**. The so-called spark events are triggered by a PMT discharge which produces enough energy to give a trigger signal in the Calorimeter First Level Trigger. These events are characterised by a large energy imbalance in one cell and easily identified.

- $\boldsymbol{E - p_z}$. The $E - p_z$ quantity is used to reject unphysical events. For a fully contained event in the CAL, from momentum conservation, $E - p_z = 2E_e$. Using the CAL energy information, an event is rejected if $(E - p_z)_{CAL} > 75$ GeV.

After an event is accepted by the GSLT, all the components send their data to the Event Builder which writes all the event information in a format similar to that used in

the offline analyses and sends it to the Third Level Trigger (TLT). The TLT is a UNIX farm of Silicon Graphics stations and runs a simplified part of the offline reconstruction code, such as electron finders and track reconstruction algorithms. It has been designed to reduce the rate to a few Hz. The TLT applies a set of physics filters to the events and is able to further suppress background and classify events according to specific physics requirements.

Events accepted by the TLT are sent via a FDDI link to the computing center and stored on tape.

Chapter 3

Data Selection

3.1 Introduction

The data used for this analysis were collected by the ZEUS detector during HERA's operation in the years 1996 and 1997 corresponding to an integrated luminosity of about 38 pb^{-1}. As described earlier, the events had to satisfy a three level trigger prior to their storage and subsequent offline reconstruction.

The signature of elastic photoproduction $J/\psi \to \mu^+\mu^-$ is a clean 2-track event with small energy deposit in the Uranium Calorimeter compatible with a minimum ionizing particle (mip) and hits in the muon chambers.

The starting data sample for this analysis was selected by requiring the elastic muon filters with the additional requirement of a reconstructed vertex in the interaction region.

A detailed description of the online and offline selection filters is given below following, as much as possible, the trigger and data acquisition stream and the reconstruction steps.

Due to the different shape and design of the detectors over the polar angle, the trigger is subdivided into 3 regions corresponding respectively to the forward ($15^\circ < \theta < 30^\circ$), barrel ($34^\circ < \theta < 135^\circ$) and rear region ($135^\circ < \theta < 160^\circ$). The overall muon distribution as a function of the polar angle is shown in Fig. 3.1 with superimposed those for events that had a trigger set in forward, or in the rear region.

3.2 First Level Trigger

At First Level Trigger (FLT) only a subset of the detector information is available for the selection, like rough estimates of the energy deposit in the different towers of the electromagnetic and hadronic sections of the calorimeter, tracking quality information and muon triggers. In addition events are rejected if the activities in the C5 counter, the Vetowall and the SRTD have a timing inconsistent with that of an *ep* interaction.

The detector components used in the selection are the CTD, the main calorimeter and the inner muon detectors (FMUI, BMUI, RMUI). A brief description of the main FLT quantities that appear in the trigger logic of the selection is given below:

- Muon trigger:

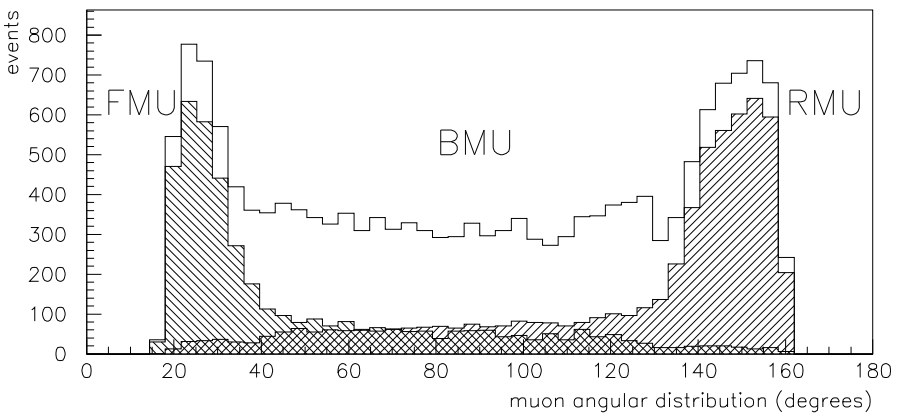

Figure 3.1: Total angular distributions of the decay muons. Superimposed are the fraction of events triggered by the FMUON (left) and RMUON (right) chambers. The remaining events have been triggered by the BMUON

.

  - FMUI tag contains the information of a hit in the first LST plane of the FMUON detector. The information is segmented into four angular regions (cf. Fig. 2.9).
  - B/RMUI trigger requires the presence of a segment in the inner barrel or rear muon chambers. For the barrel region the information is segmented into eight regions over the ϕ angle following the detector boundaries while for the rear region the information is segmented into two corresponding to the two RMUON detector halves.

- Calorimeter Quantities:

  - CAL_*isomu* is set when the energy deposit in one region of CAL compatible with a traversing mip. The definition of a mip involves cuts on the energies seen by the electromagnetic and hadronic cells as well as requirements on the spatial extension and shape of the global energy deposit. At FLT the whole Calorimeter information is segmented in sixteen regions (Fig.3.2) and is used in coincidence with other detectors as the muon chambers for trigger pourposes.
  - CAL_E_{FLT}: Total energy deposited in the calorimeter excluding the contributions from the towers of the first three rings around the FCAL beam pipe and those of the first ring around the RCAL beam pipe.
  - $FCAL_Ebp_{FLT}$: Sum of the energy deposit in the towers of the first ring around the FCAL beam pipe. Cuts on this quantity are used to discard proton diffractive events.

- Tracking Information: The CTD FLT provides a quick event classifaction by running a hardware reprogrammable track finding algorithm. The output is given in terms of:
  - *Track multiplicity*: An estimate of the number of reconstructed segments.
  - *Track class*: A function relating the number of reconstructed tracks and the number of track segments pointing to the vertex.

3.2.1 FLT Selection

Depending on the angular region considered the following conditions are required:

- FMUON region (FLT slot 4):

  A hit in FMUI matching an "isolated muon" compatible energy deposit in the corresponding FCAL regions as well as the absence of similar energy deposit in the RCAL for halo muon rejection.

- BMUON region (FLT slot 10)

  A segment in BMUI matching an "isolated muon" compatible energy deposit in the corresponding BCAL regions

- RMUON region (FLT slot 11)

  A segment in RMUI matching an "isolated muon" compatible energy deposit in the corresponding RCAL regions

The previously mentioned triggers require in addition general cuts on the calorimeter and the tracking. These are:

- CTD Requirements:

  from 1 to 5 track segments found in the CTD with at least one pointing to the nominal interaction point.

- Calorimeter Energy:

  Hadronic energy $E_{HAC} > 464$ MeV.

3.3 Second Level Trigger

At second level trigger the following conditions are required:

- The total energy deposit in the calorimeter has to be lower than 10 GeV and the ratio between hadronic and e.m. energy in FCAL is required to be greater than 3/2.
- If there are reconstructed tracks in the CTD, the SLT requires that the primary vertex to be at $|z| < 75$ cm and the track multiplicity lower than 5.
- CAL Timing cuts are chosen to remove events coming from proton beam gas interactions.

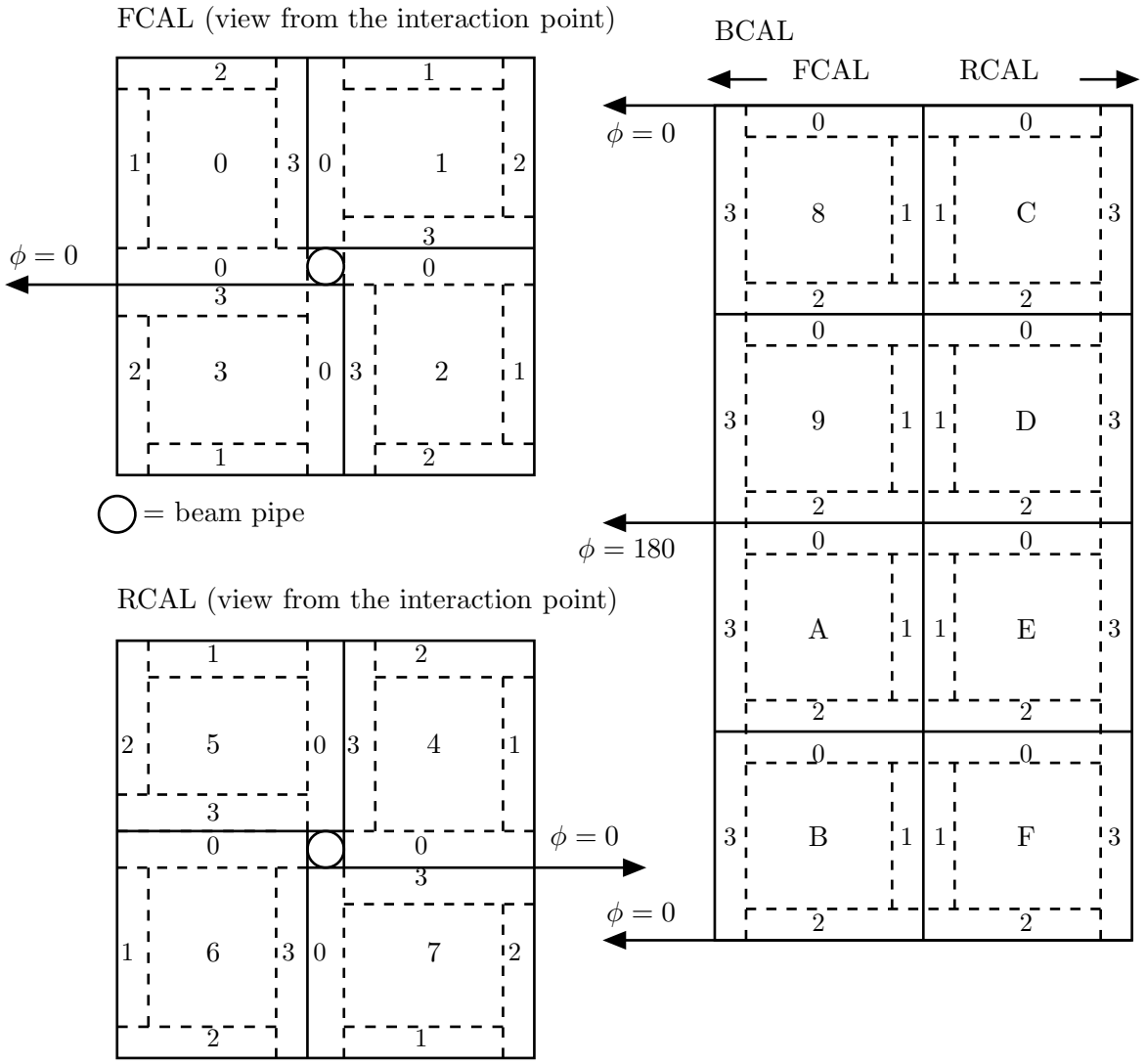

Figure 3.2: The CAL *isomu* regions: forward (4), barrel (8) and rear (4) The numbers on the edges indicate the number of rows of cells that have to be below the energy threshold in oder to have an isolated muon definition.

3.4 Third Level Trigger

Events that have passed the GSLT are subjected to a fast reconstruction involving among others electrons and muons candidates finding by matching tracks and hits measured by the different detectors. In particular for low momentum muon candidates we are interested in, a match between the CTD, the Uranium Calorimeter and depending on the polar angle, the inner Forward, Barrel or Rear Muon chambers is perfomed. A brief description of the packages used is given below.

3.4.1 FMUON TLT

At third level trigger a matching algorithm (*mamma* [37]) based on a parabolic fit involving hits in the FMUI with the forward CTD tracks and isolated energy deposit consistent with a mip in FCAL is applied. A mip is defined at TLT in terms of an isolated energy deposit in the Uranium Calorimeter [38] and involves cuts on the energies seen by the electromagnetic and hadronic cells as well as requirements on the spatial extension and shape of the global energy deposit as summarized in table 3.1.

component	type of cut	cut parameter
EMC	energy	$0.0GeV \leq energy \leq 3.0GeV$
HAC	energy	$0.5GeV \leq energy \leq 8.0GeV$
EMC	# cells	$1 \leq \#cells \leq 6$
HAC	# cells	$1 \leq \#cells \leq 6$

Table 3.1: Definition of a mip at TLT.

At least one FMUON match and a pair of CTD tracks of opposite charge with an invariant mass greater than 1 GeV are required.

3.4.2 BMUON, RMUON TLT

In the barrel and rear region the *glomu* [39] package is used: a muon candidate is formed by matching a track from the CTD to a calorimeter energy cluster, consistent with a passage of a mip, and to a good track segment in BMUI or RMUI

The CTD track has to satisfy the following criteria:

- the impact parameter of a track, i.e. the minimum distance of the track from the origin in the ZEUS x, y plane, must be less than 10 cm in order to reject cosmic muons
- $|z| \leq z_{max}(75cm)$
- the momentum associated with the track should exceed 1 GeV

Once a track satisfies these requirements it is extrapolated from the point of closest approach to the vertex to a fiducial surface (external to the CTD) via a Runge-Kutta integration. This method has been adopted because of its precise extrapolation: the number of integration steps is dictated by a compromise between speed and accuracy.

A track satisfying these criteria is extrapolated to the BMUI and RMUI chambers and a match with a BMUI or RMUI segment is required.

3.5 Event Reconstruction

Data collected during luminosity run are stored and submitted to the reconstruction. The reconstruction, not having the tight constraints of the running phase performs a calculation similar to that at TLT but more refined, using the full ZEUS software from the Physics Groups and taking into account the data taking and detector conditions and known correction.

3.5.1 Tracking

Track and vertex are reconstructed using the *VCTRAK* package [40] a streamlined version of is available and used at the Third Level Trigger also. Besides the default mode of operation, namely *CTD Regular*, during this analisys also the *CTD only* was used. While the last is derived from the 9 superlayers of the CTD information only, the CTD Regular mode makes use of the segments and hits found by FRTD reconstruction program in the RTD and FTD1 detectors as well in order to increase the angular acceptance. A drawback of this solution are the additional uncertainties in the Monte Carlo description and in the alignment that may in particular cases justify the use for precise measurements of the CTD *only* solution.

3.5.2 Muons

Essentially the same tracking, and mip matching algorithms previously described and already used at TLT are re-applied with an enhanced detector description (dead tubes, inefficiency regions etc).

3.6 Offline Event Selection

This section describes the offline selection of the final J/ψ data sample. The complete list of the selection criteria as well as some discussion on their tuning is shown below.

- The events had to pass the specific trigger slots as mentioned earlier in this chapter.
- Runs with detector or read-out problems affecting the components used in this analysis were removed keeping detailed trace of the corresponding luminosities.
- Exactly two tracks of opposite charge in the CTD fitted to a vertex.
- $|Z_{vertex}| < 50cm$ (the vertex distribution for data and Monte Carlo is shown in Fig. 3.3).
- The Calorimeter noise suppression routines [41] were applied in order to remove noisy isolated cells.

- Energy cut on the first ring of FCAL ($FCAL_Ebp_{FLT} < 0.5$ GeV) for proton dissociation background removal.
- Each track should have hits in at least three superlayers of the CTD in order to guarantee a good reconstruction quality. This translates into a cut on the polar angle $17^\circ < \theta < 163^\circ$.
- To further reduce contribution from cosmic ray muons traversing the interaction region the angle beween the two muon tracks had to satisfy the cut:

  $$\cos\theta_{\mu^+\mu^-} < -0.995 \text{ (equivalent to } \theta_{\mu^+\mu^-} < 174^\circ)$$

- Elastic selection (as described below).

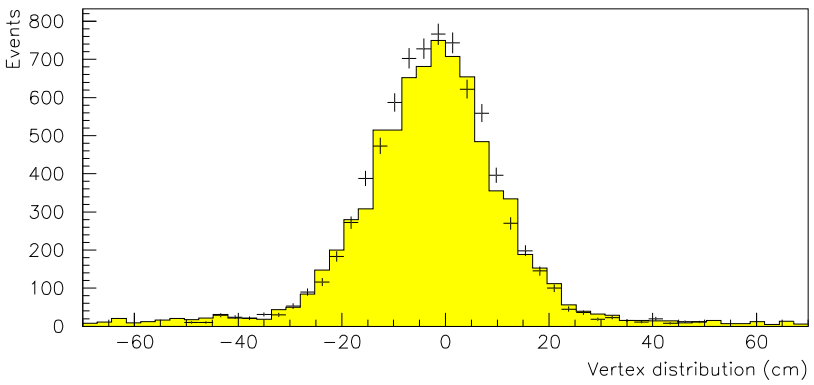

Figure 3.3: Vertex distribution (z coordinate) of the data after the selection. The full histograms are from a sample of DIPSI Monte Carlo events.

3.7 Elastic Selection

In order to select only elastic event, more refined cuts on mip compatibility and on the event topology are applied. For the mip a slightly modified version of the *cellcone* routine [42] was used for tracking-calorimeter matching. Each of the two CTD tracks is extrapolated to the Inner Calorimeter surface. After noise subtraction the energy deposit of the cells within a cylinder centered in the track impact point and oriented along the track direction is computed both for the electromagnetic and hadronic sections as shown in Fig. 3.4.

Cuts on the total energy deposit inside and outside the cylinders are available to remove the remaining events with deposits non compatible with two muons elastic events. The procedure needs to tune the radius of the cylinder, which must completely contain the energy released by muons in the calorimeter, and the cell energy thresholds.

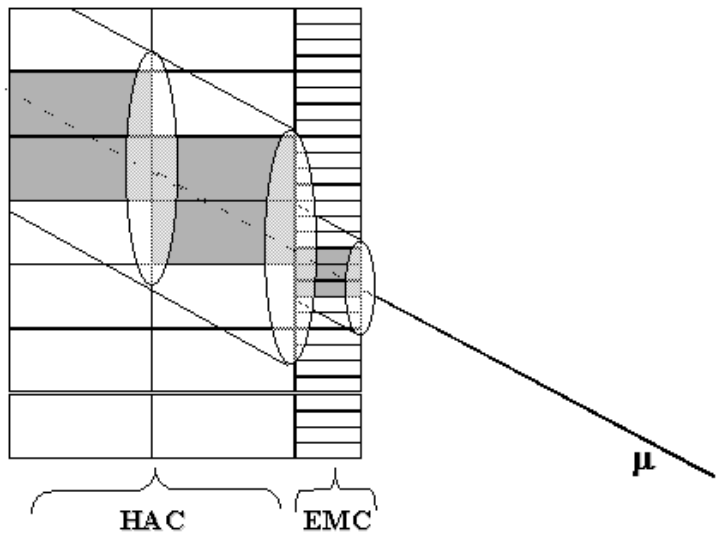

Figure 3.4: Track-calorimeter energy matching: the cell energy inside the cylinders is associated to the track.

3.7.1 Cylinder Radius Tuning

The tuning of the cylinder radius for both EMC and HAC has been performed using elastic J/ψ Monte Carlo (DIPSI) events and studying the selection efficiency and residual energy (defined as calorimeter energy not associated to a track) as a function of the cylinder radius. Figures 3.5 and 3.6 show separately for EMC and HAC section, efficiency and residual energy (when evaluating the residual energy for one section, the radius of the other section has been fixed to the final value). Both efficiency and residual energy show saturation increasing the radius.

3.7.2 Energy Threshold Tuning For Noise Subtraction

The cell thresholds have been tuned using random triggers which, having no special requirements, are unbiased and well suited for noise studies. Figures 3.7 and 3.8 show the EMC and HAC distributions of the maximum cell energy not associated to a track for random triggers (dashed histogram) and data (dots) normalized to the entries up to 100 MeV (random trigger entries are a factor ~ 2 above the data). Increasing the cell energy, data tend to be over the noise, clearly indicating an inelastic contribution or, in the case of the rear energy, that the scattered positron begins to be visible. Table 3.2 reports the choosen thresholds for the different calorimeter sections and parts and also the inefficiency of each cut, defined as the noise events which pass the cut divided by the total noise events.

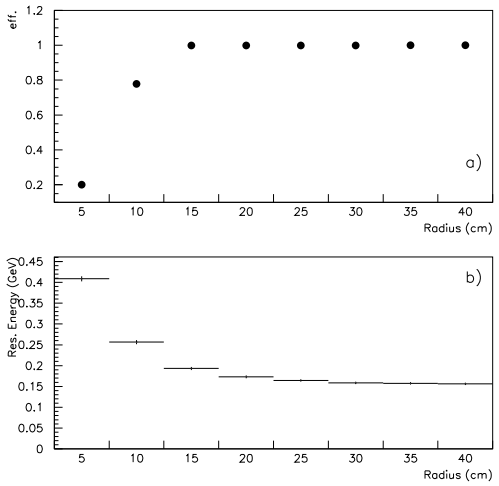

Figure 3.5: Efficiency and residual energy for the EMC CAL section. a) Efficiency as a function of the radius. b) Residual energy as a function of the radius fixing the HAC section radius to 50 cm.

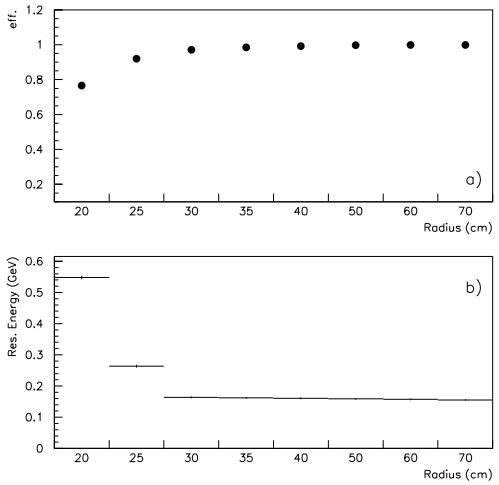

Figure 3.6: Efficiency and residual energy for the HAC CAL section. a) Efficiency as a function of the radius. b) Residual energy as a function of the radius fixing the EMC section radius to 30 cm.

3.7.3 Mip compatibility

Further requirements on the calorimeter energy associated to the track should be compatible with a muon deposit. The following conditions on the ratio between HAC and EMC energy ($R_{H/E}$) and the total energy associated to the track (E_{track}) are applied:

- $R_{H/E} > 0.8$

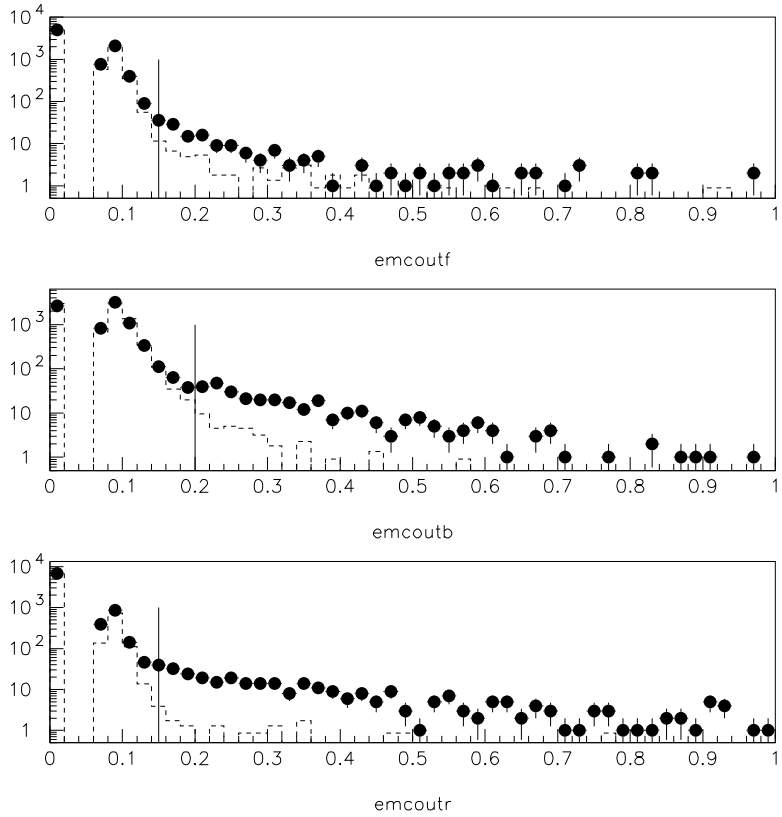

Figure 3.7: Maximum cell energy not associated to a track for forward, barrel and rear EMC section calorimeter. Data (dots) are normalized to random triggered events (dashed histogram) up to 100 MeV. The vertical bars show the applied cut.

CAL Section	Threshold (MeV)	Inefficiency
REMC	150	.003
BEMC	200	.004
FEMC	150	.008
RHAC	300	.004
BHAC	300	.004
FHAC	300	.004

Table 3.2: Thresholds and inefficiencies for the elastic selection in the different CAL sections.

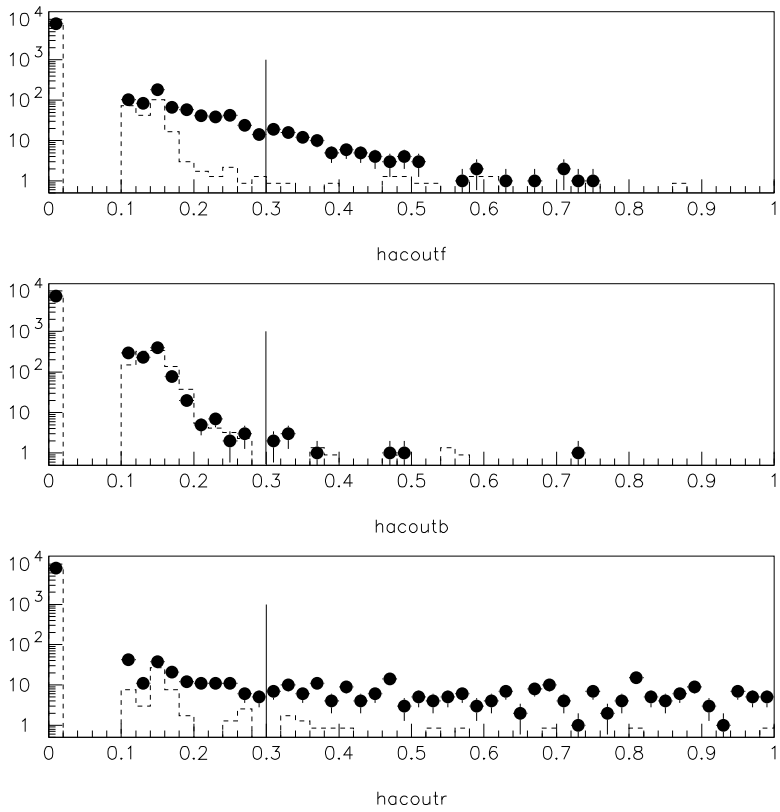

Figure 3.8: Maximum cell energy not associated to a track for forward, barrel and rear HAC section calorimeter. Data (dots) are normalized to random triggered events (dashed histogram) up to 100 MeV. The vertical bars show the applied cut.

- $0.7 < E_{track} < 4.0$ GeV.

The relevant distributions for data and DIPSI Monte Carlo are shown in Fig. 3.9. A small shift (200 MeV) in energy distribution between data and Monte Carlo is observed. Due to the large cuts applied the discrepancy does not affect the results of the analysis.

The efficiency of the cuts is above 97%.

3.8 Final Data Sample

After all selection cuts described above a sample of about 12000 events is obtained. No costraint on the reconstructed invariant mass $M_{\mu^+\mu^-}$ was applied yet. In Fig. 3.10 the number of selected events per unit of integrated luminosity over the two years of data taking is shown. All plots show that the rate of the accumulated J/ψ events candidated is stable with the integrated luminosity. Inefficiencies due to detector or

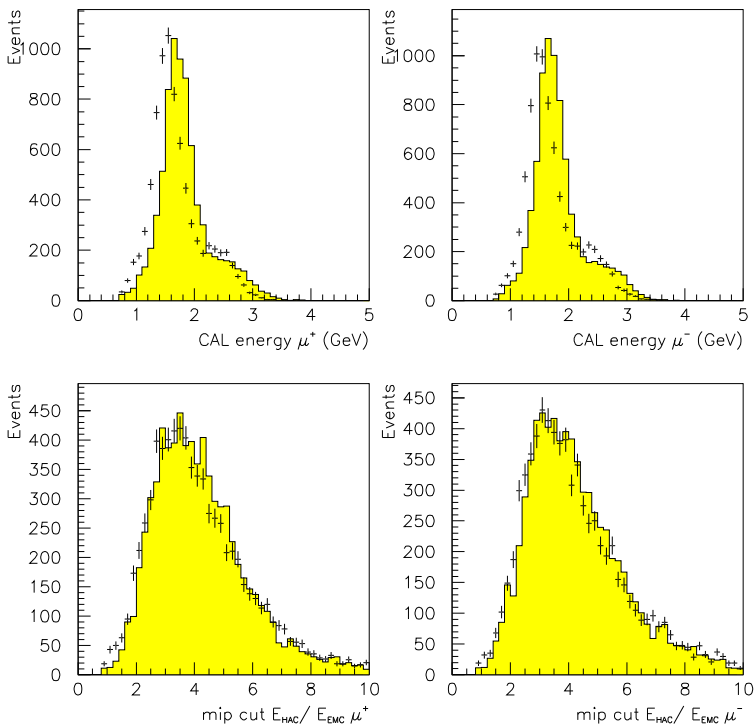

Figure 3.9: Mip cuts: total energy distribution ($E_{EMC} + E_{HAC}$) and E_{HAC}/E_{EMC} ratio for the final selection. The distributions are displayed for positive and negative muons separately. The full histograms are from a sample of DIPSI Monte Carlo events.
.

beam related problems have been included in the luminosity estimation. In table 3.8 the list of integrated luminosity is given for each data taking year for the central components (CTD, CAL alone) and for the central components including the muon systems (FMUON, BRMUON).

The plot in Fig. 3.11 shows the reconstructed mass distribution $M_{\mu^+\mu^-}$ for the selected sample. The J/ψ peak is clearly visible. A second bump at about 3.7 GeV visible in log scale shows the signal coming from the di-muon decay of the ψ' vector meson. About 9000 events are in the mass range $2.5 \leq M_{\mu^+\mu^-} \leq 4.0$.

In figures 3.12,3.13 two events of the selection sample are displayed by means of the ZEUS event display.

Integrated luminosity in pb^{-1}			
	1996	1997	Total
ZEUS	10.710	27.694	38.404
FMUON	7.596	26.374	33.967
BRMUON	10.530	27.485	38.015

Integrated luminosity in pb^{-1} during the 1996 1997 data taking for the central component (CTD, CAL) and the muon (FMUON and BRMUON) elastic triggers.

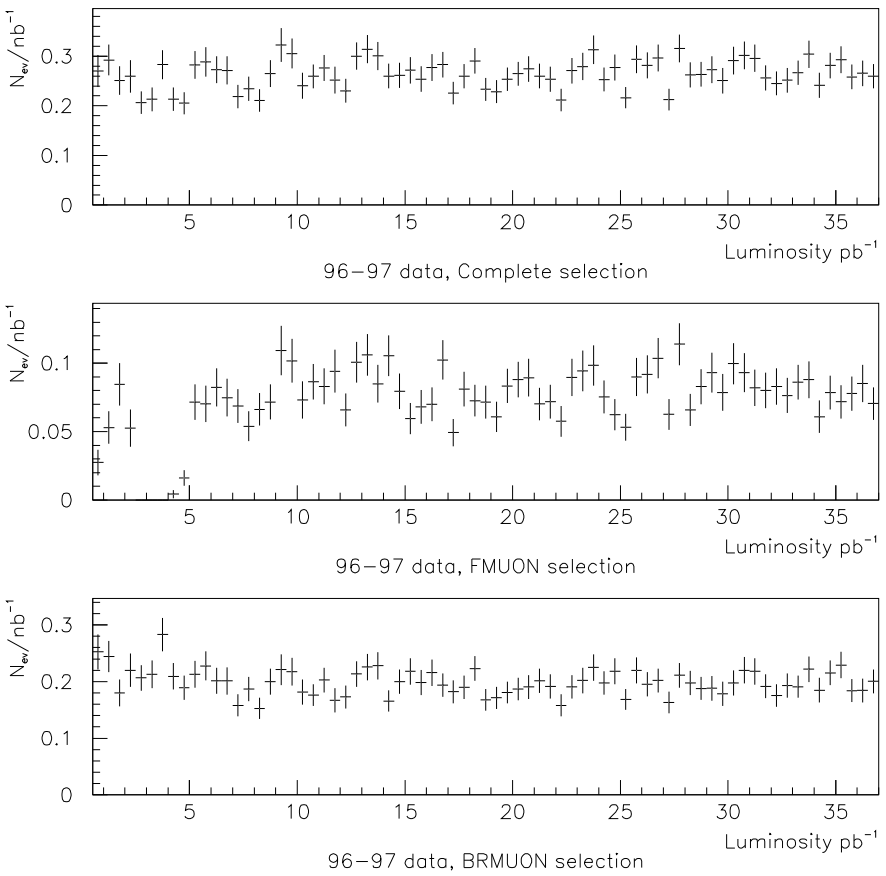

Figure 3.10: Overall stability of the selection. The number of the selected events per nb^{-1} in the mass range $2.5 < MJ/\psi < 4.0$ GeV is displayed as a function of the integrated luminosity over the two years of data taking (38 pb^{-1}). Below the same plot for the FMUON and BRMUON selection. The lower values in the first bins of the FMUON selection are related to bad data taking/beam conditions. This and other corrections have been included in the final luminosity and efficiency estimation.

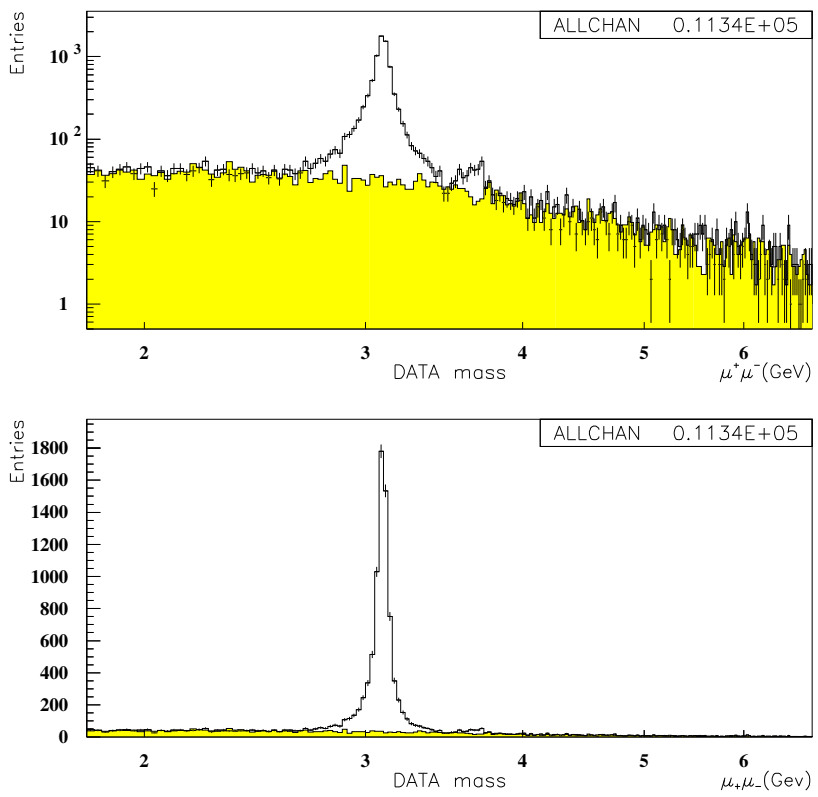

Figure 3.11: $\mu^+\mu^-$ invariant mass distribution as obtained after applying the full selection, plotted once in linear and once in logarithmic scale. The ψ' peak at 3.689 GeV is visible in log scale. The superimposed full histogram is the Bethe-Heitler $\gamma\gamma \to \mu^+\mu^-$ contribution as obtained from the LPAIR Monte Carlo normalized to the data in the region outside the J/ψ mass region.

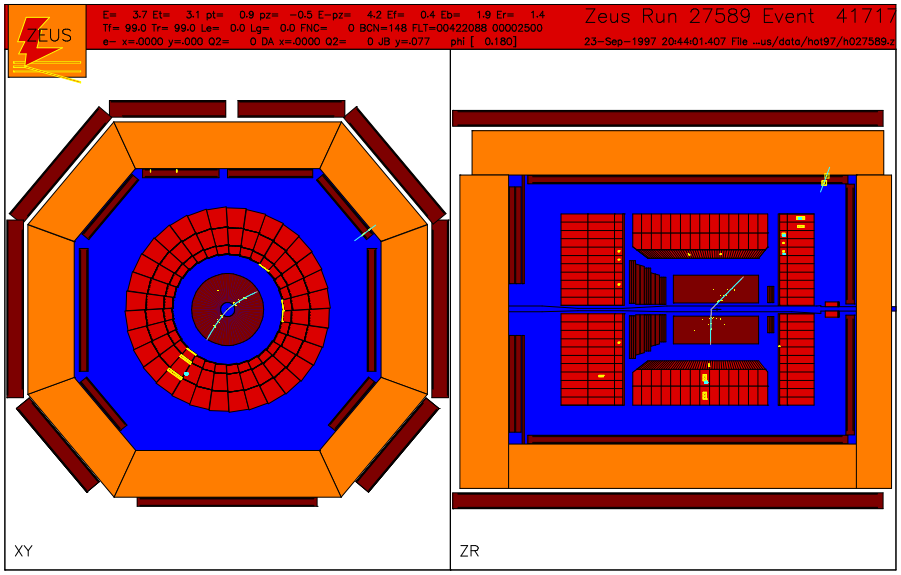

Figure 3.12: An event of the selection triggered by the rear muon system. This is a clean elastic event in the J/ψ mass region.

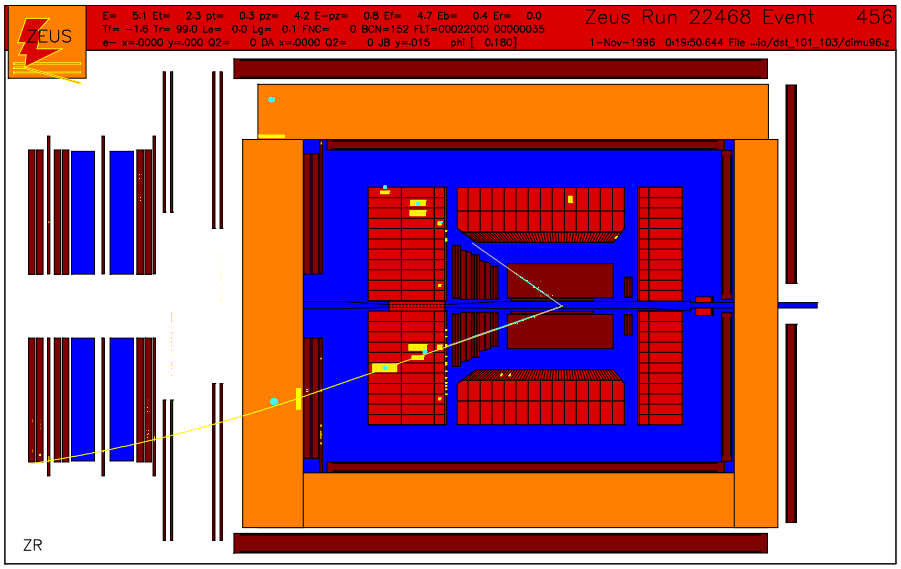

Figure 3.13: An event of the selection triggered by the FMUON system. The di-muon pair is boosted in the forward region with a complete track reconstructed in the spectrometer. This event comes from a di-muon decay of an Υ vector meson.

Chapter 4

Data and Monte Carlo Studies

To study the resolution of the detector in the reconstruction of physics variables and to evaluate the acceptance of the apparatus, a sample of Monte Carlo events have been generated and passed through an accurate simulation of the detector response and trigger. These events have been reconstructed and analyzed with the same programs as for the data.

4.1 The Monte Carlo Chain

The ZEUS Monte Carlo chain consists of 4 programs: the data-flow diagram of figure 4.1 shows their relation.

- **ZDIS** (Zeus interface to Deep Inelastic Scattering) [43]. It runs a user-defined Monte Carlo generator which produces events, according to specific reactions and models, and writes the results of the generation (e.g. the four-momenta of the final state particles) in a format understood by the program which simulates the whole apparatus.
- **MOZART** (MOnte carlo for Zeus Analysis, Reconstruction and Trigger) is a full simulation of the ZEUS detector. The structure of the ZEUS detector, geometry and material, are simulated using the GEANT [44] package; a full simulation of the magnetic fields is included. The final state particles of a ZDIS event are tracked through the apparatus taking into account particle decays, interactions with materials in the detector and detector response. The program produces two data structures: the first containing the complete information on the four-momenta of all tracks in the event and the coordinates of their hits in the detector, and a second containing the raw-data as observed from the detector response.
- **ZGANA** (ZG313 ANAlysis) [45] is a complete simulation of the three-level trigger system of ZEUS. The events which pass or fail the trigger requirements are identified by a bit pattern; this information is used to evaluate trigger efficiencies.
- **ZEPHYR** is the ZEus PHYsics Reconstruction package [46] and is run on both data and Monte Carlo to reconstruct energies, momenta and the other physics quantities used for physics analyses. It's logically subdivided in 3 phases. First

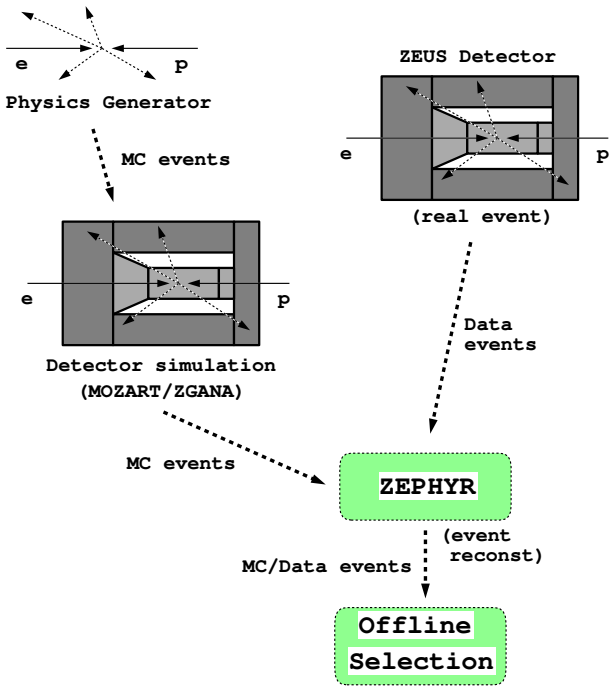

Figure 4.1: Structure of the ZEUS offline software.

(*phase 1*) data are reconstructed for individual components and physics quantities such as calorimeter cell energy and track segments in the chambers are computed. Later (*phase 2*) compound objects are created using the information of different detectors; track segments from different tracking devices are used together in order to determine the event vertex. Clustering algorithms are applied to groups of calorimeter cells. In the last stage (*phase 3*), physics variables to be used for data analyses, such as particle four-momenta and other observables, are evaluated and flags corrresponding to different physics processes are set and stored among the data in the form of a Data Summary Tape (DST). Each event has a bit pattern corresponding to the different trigger requirements it has satisfied.

4.2 Reconstruction of Kinematic Variables

In the measurement of the exclusive reaction $ep \rightarrow eJ/\psi p$ in photoproduction regime, since both the electron and the proton escape from the detector undetected, all relevant kinematic variables have been reconstructed from the decay particles ($\mu^+\mu^-$) as extracted from the the tracking detectors when assuming the mass of the muon. In

particular for the J/ψ energy-momentum and the invariant mass are:

$$\begin{aligned} P_{iJ/\psi} = P_{i\mu^+\mu^-} &= P_{i\mu^+} + P_{i\mu^-} \qquad (i = x, y, z) && (4.1)\\ E_{J/\psi} = E_{\mu^+\mu^-} &= \sqrt{M^2_{\mu^+} + P^2_{\mu^+}} + \sqrt{M^2_{\mu^-} + P^2_{\mu^-}} && (4.2)\\ M_{J/\psi} &= \sqrt{E^2_{\mu^+\mu^-} - P^2_{\mu^+\mu^-}} && (4.3) \end{aligned}$$

In photoproduction regime, i.e. $Q^2 \approx 0$ the emitted photon has zero transverse momentum and a longitudinal momentum $P_{z\gamma} \approx -E_\gamma$ in the direction of the incoming proton. From the assumption that the emitted virtual photon is parallel to the beam axis it follows that

$$E_\gamma - P_{z\gamma} \approx 2E_\gamma; \tag{4.4}$$

Using the conservation of energy and momentum

$$E_\gamma + E_p = E_{J/\psi} + E_{p'} \tag{4.5}$$

$$P_{z\gamma} + P_{zp} = P_{zJ/\psi} + P_{zp'} \tag{4.6}$$

and subtracting equation 4.6 from 4.5, one gets

$$E_\gamma - P_{z\gamma} \approx E_{J/\psi} - P_{zJ/\psi} \approx 2E_\gamma \tag{4.7}$$

where the relations $E_p \approx P_{zp}$ and $E_{p'} \approx P_{zp'}$ were used. The obtained result can be used to reconstruct the $\gamma^* p$ center of mass energy as:

$$\begin{aligned} W^2_{\gamma^* p} = (P_p + q)^2 &= M_p - Q^2 + 2P_p \cdot q \\ &\approx 2E_p(E_\gamma - P_{z\gamma}) \\ &\approx 2E_p(E_{J/\psi} - P_{zJ/\psi}) \end{aligned} \tag{4.8}$$

while the transverse momentum t at the proton vertex is approximated by the vector meson transverse momentum:

$$\begin{aligned} t = (P_p - P_{p'})^2 &= (P^2_{J/\psi} - q)^2 \\ &= M^2_{J/\psi} - Q^2 - 2P_{J/\psi} \cdot q \\ &\approx -2E_\gamma(E_{J/\psi} + P_{zJ/\psi}) + M^2_{J/\psi} \\ &\approx -(E_{J/\psi} - P_{zJ/\psi})(E_{J/\psi} + P_{zJ/\psi}) + M^2_{J/\psi} \\ &= -P^2_{TJ/\psi} \end{aligned} \tag{4.9}$$

where, as already mentioned, the value of t deviates from $-P^2_{TJ/\psi}$ for non zero values of Q^2.

When reconstructing the decay angles, since the scattered electron is not measured, only the decay angles θ_h and ϕ_h were extracted. The virtual photon was assumed to be emitted parallel to the beam axis.

4.3 Kinematic Variables Resolution

In this section a study on the reconstruction of the main physics quantities used in this analysis is shown. This is done by means of Monte Carlo samples, by direct comparison of the reconstructed quantities, as obtained after the full detector simulation with the generated quantities.

The quality of the reconstruction of $W_{\gamma p}$ is shown in Fig.4.2. Over the whole $W_{\gamma p}$ range the agreement between the generated and reconstructed quantity is good. Both at low and high $W_{\gamma p}$ the agreement becomes slighly worse due to the lower accuracy for tracks traversing a minor number of superlayers of the CTD. The W range with reasonable acceptance is in the range $30 < W < 150$ GeV. As previously mentioned, events at low W will have the outcoming muons essentially in the forward muon spectrometer region (FMUON) while events at medium or high W are characterized by tracks in the barrel or rear region respectively.

The reconstruction quality of p_T^2 which in photoproduction should be equal to the proton transverse momentum squared t is shown in Fig.4.3. The agreement is satisfactory at small p_T^2 and becomes less accurate for $|t| > 1$ GeV^2.

4.3.1 $W_{\gamma p}$ and t Binning

The W range $30 < W < 150$ GeV has been subdivided into 6 bins of equal width with comparable populations. The migrations from one bin to the other are low and always below 10%.

The t range $0. < |t| < 1.8$ has been subdivided into 6 bins of different size in order to take into account the different statistics available in each bin and to minimize migration effects. The migrations from one bin to the others are generally low at low t and become quickly worse as soon as t increases. In table 4.1 the acceptance [1] and purity [2] are shown for each W and t bin.

4.4 Trigger Efficiency

In the present section the trigger efficiency of the slots used in the analysis has been studied.

The trigger efficiency of CTD has been estimated using an independent trigger of deep inelastic scattering events by requiring the scattered electron to be seen in the Calorimeter. The comparison between data and Monte Carlo has shown to be in good agreement [47]. An uncertainty of 5% has been included when considering the systematics.

Concerning the muon detectors the trigger efficiency has been studied using the same elastic selection of 2-track events [3]. Since the trigger information is segmented

[1] The acceptance is defined as the ratio of accepted events generated in one kinematic bin over the number of generated in the same bin

[2] The purity is defined as the ratio of events generated and reconstructed in a given bin over the number of events reconstructed in the same bin.

[3] The full selection described in chapter 3 without the final invariant mass cut in the J/ψ region. By doing so a higher statistics and a wider muon momentum range can be analized.

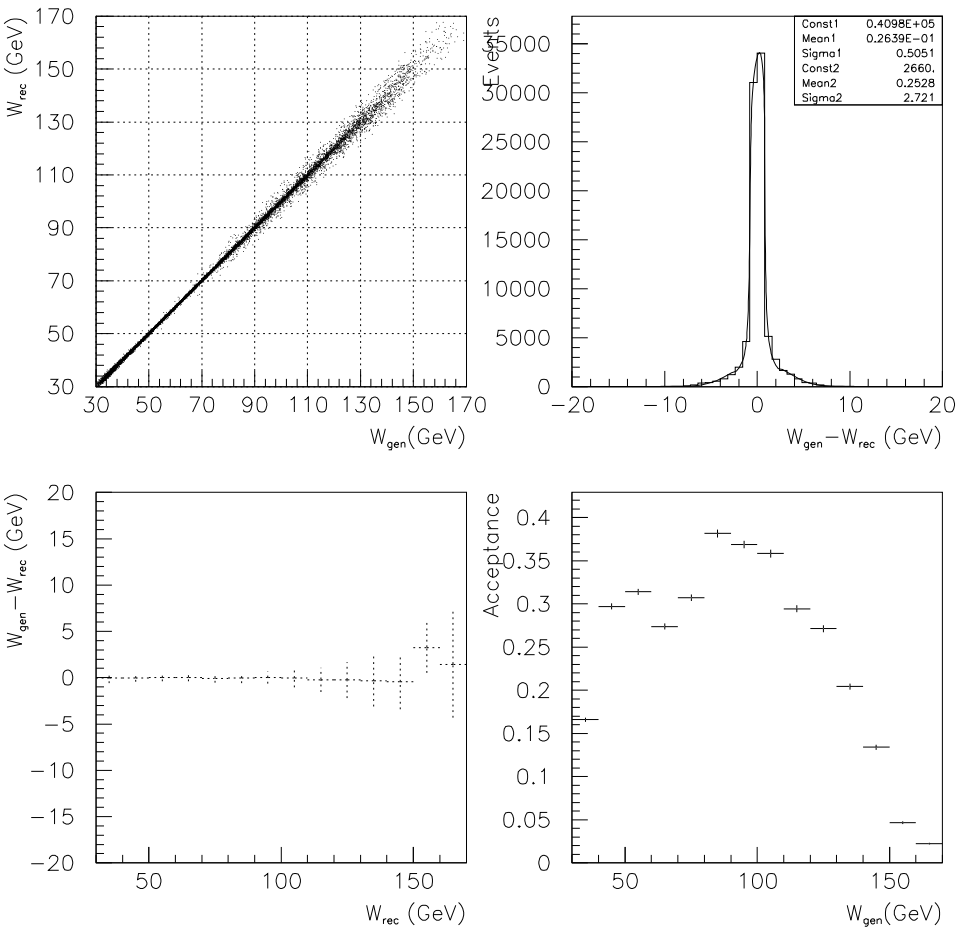

Figure 4.2: Plots from the reconstruction of W: 1) correlation between W_{rec} and W_{gen}; 2) distribution of $W_{gen} - W_{rec}$; 3) $(W_{gen} - W_{rec})$ as a function of W_{rec} and 4) acceptance as a function of W_{gen}

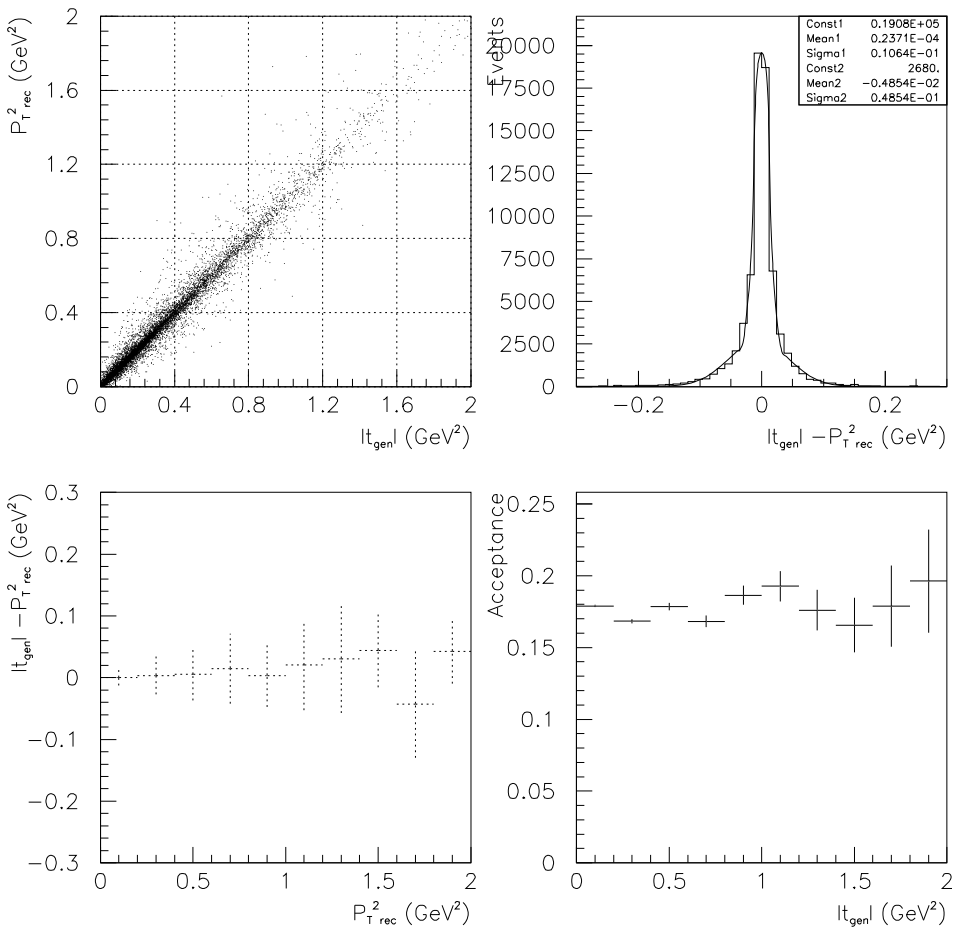

Figure 4.3: Plots from the reconstruction of t as measured from the J/ψ p_T^2: 1) correlation between p_{Trec}^2 and $|t_{gen}|$; 2) distribution of $|t_{gen}| - p_{Trec}^2$; 3) $(|t_{gen}| - p_{Trec}^2)$ as a function of p_{Trec}^2 and 4) acceptance as a function of $|t_{gen}|$

Purity / Acceptance	$30 < W < 50$	$50 < W < 70$	$70 < W < 90$	$90 < W < 110$	$110 < W < 130$	$130 < W < 150$
$0.0 < t < 0.2$	0.94 / 0.24	0.94 / 0.29	0.93 / 0.33	0.90 / 0.35	0.86 / 0.28	0.85 / 0.16
$0.2 < t < 0.4$	0.67 / 0.24	0.78 / 0.31	0.75 / 0.35	0.70 / 0.36	0.68 / 0.28	0.60 / 0.16
$0.4 < t < 0.6$	0.61 / 0.24	0.72 / 0.31	0.72 / 0.36	0.64 / 0.38	0.59 / 0.28	0.50 / 0.18
$0.6 < t < 0.6$	0.46 / 0.28	0.63 / 0.35	0.61 / 0.39	0.56 / 0.36	0.48 / 0.32	0.42 / 0.18
$0.8 < t < 1.2$	0.54 / 0.27	0.63 / 0.38	0.61 / 0.40	0.62 / 0.43	0.56 / 0.34	0.52 / 0.21
$1.2 < t < 1.8$	0.54 / 0.24	0.61 / 0.44	0.60 / 0.46	0.59 / 0.43	0.62 / 0.39	0.32 / 0.25

Table 4.1: Purity and Acceptance for each W and t bin as extracted from the Monte Carlo simulation using the DIPSI generator.

over the whole muon system in several regions, 2-track events with a known trigger track may be used to study the efficiency in the region pointed by the second track as shown in Fig. 4.5.

The obtained efficiencies, plotted as a function of the muon momentum, were compared with the Monte Carlo simulation. Similar results are obtained in [48],[49].

In Fig.4.4 the muon momenta and transverse component are drawn as a function of the polar angle. It can be observed that while in the forward and rear regions the muon momenta range extends from 1 to 5 GeV in the barrel region the momentum range is sensibly lower, with the J/ψ meson produced almost at rest in the laboratory frame. It turns out that the transverse momentum p_T is a more natural unit to study the efficiency dependence in the barrel region. For the barrel region more than 90% of the muons detected are in the range $1 < p_T < 2$ GeV.

FMUON trigger

The efficiency for a single muon passing FCAL and FMUI has been evaluated using the selected sample with the additional requirement of a barrel or rear muon trigger set and one of the tracks in the polar region with $15° < \theta < 30°$. In Fig. 4.6 the efficiency as a function of the forward traversing muon momentum is drawn for data and Monte

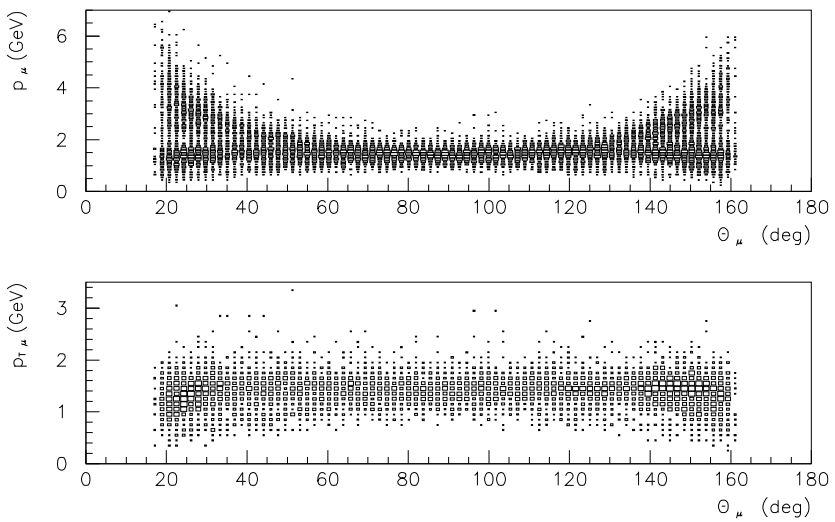

Figure 4.4: Muon p and p_T distributions as a function of the polar angle for the data after the selection.

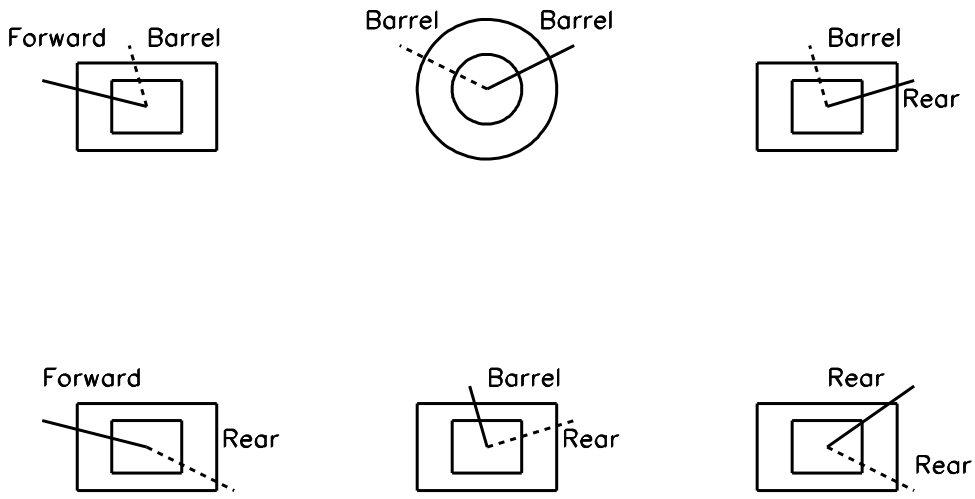

Figure 4.5: Some of the events topologies used for the muon chamber efficiency studies. Using the selected 2-track elastic sample and requiring a trigger (continuous line) either in the forward, barrel or rear region is it possible to study the trigger efficiency of another angular region (dashed line).

Carlo. The efficiency improves for higher muon momenta and the agreement between data and Monte Carlo is satisfactory. Bins have been choosen to have a reasonable statistics (cf. Fig. 4.4). For $p < 1$ GeV the muon does not reach the muon chambers

at all.

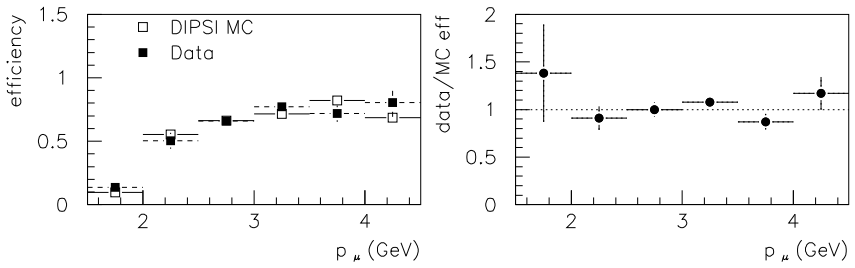

Figure 4.6: Trigger efficiency for the forward muon chambers: the trigger efficiency for data and Monte Carlo simulation as a function of the traversing muon momentum for di-muon elastic events using as independent trigger the Barrel or Rear Muon Chambers. On the right the data to Monte Carlo efficiency ratio. The trigger efficiency extracted from the data appears to be in good agreement with the Monte Carlo in the full momentum range.

BRMUON trigger

The same steps described for the FMUON case were performed to evaluate the barrel and rear elastic trigger efficiency. In Fig.4.7 the efficiency as a function of $p_T(\mu)$ of the traversing muon is drawn for events with a trigger in the forward or rear muon chambers. The same plot as a function of $p(\mu)$ is given in Fig. 4.8 for the rear muon chambers for events with a trigger in the forward or barrel region. In both cases, a discrepancy between data and Monte Carlo is observed for low muon momenta. The value of the discrepancy after reweighting with the muon momentum distribution is around 15% and 10%, for the barrel and rear section respectively.

4.4.1 Momentum Correction

When comparing the $\mu^+\mu^-$ invariant mass for data and Monte Carlo a small deviation from the nominal J/ψ mass peak (3.096 GeV) can be observed in the data sample. This small difference has turned out to be due to the uncertainty in the magnetic field of the superconducting solenoid. A momentum correction by assuming the nominal J/ψ mass value of 3.096 GeV can be easily extracted. In Fig. 4.9 the invariant mass after non resonant background subtraction (as described in next chapter) is plotted for events with tracks traversing at least 5 CTD superlayers. With a momentum correction of +0.35% the distribution matches the one described by the Monte Carlo.

4.5 Comparison of Data with Monte Carlo

In this section, to understand how well the Monte Carlo simulation describes the data behaviour, some distributions of the reconstructed quantities in data and Monte Carlo

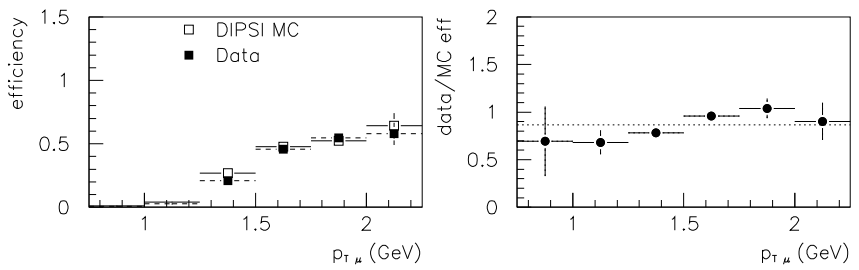

Figure 4.7: Trigger efficiency for the BMUON chambers: the trigger efficiency for data and Monte Carlo simulation is plotted as a function of the muon p_T momentum for the selected di-muon elastic events using as independent trigger the Forward and Rear Muon Chambers. The data trigger efficiency appears to be systematically lower than the Monte Carlo simulation, improving for higher p_T. In the second plot the data to Monte Carlo efficiency ratio in different bins of p_T. The muon distributions, concentrated in the range of $1.25 < p_T < 1.75$ (cf. Fig.4.4), may suggest the need for a correction of the order of 15 % in the trigger barrel muon efficiency.

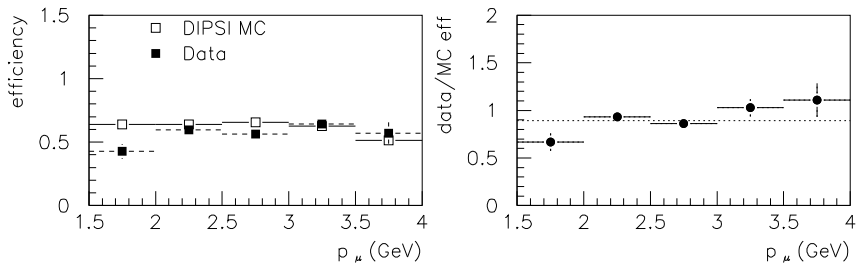

Figure 4.8: Trigger efficiency for the RMUON chambers: the trigger efficiency for data and Monte Carlo simulation is plotted as a function of the muon momentum traversing the RMUON for selected di-muon elastic events using as independent trigger the forward and barrel muon chambers. On the right the data to Monte Carlo efficiency ratio. The efficiency appears to be slightly lower than in Monte Carlo expectations in the lower momentum regions. A trigger efficiency correction of the order of 10% can be assumed.

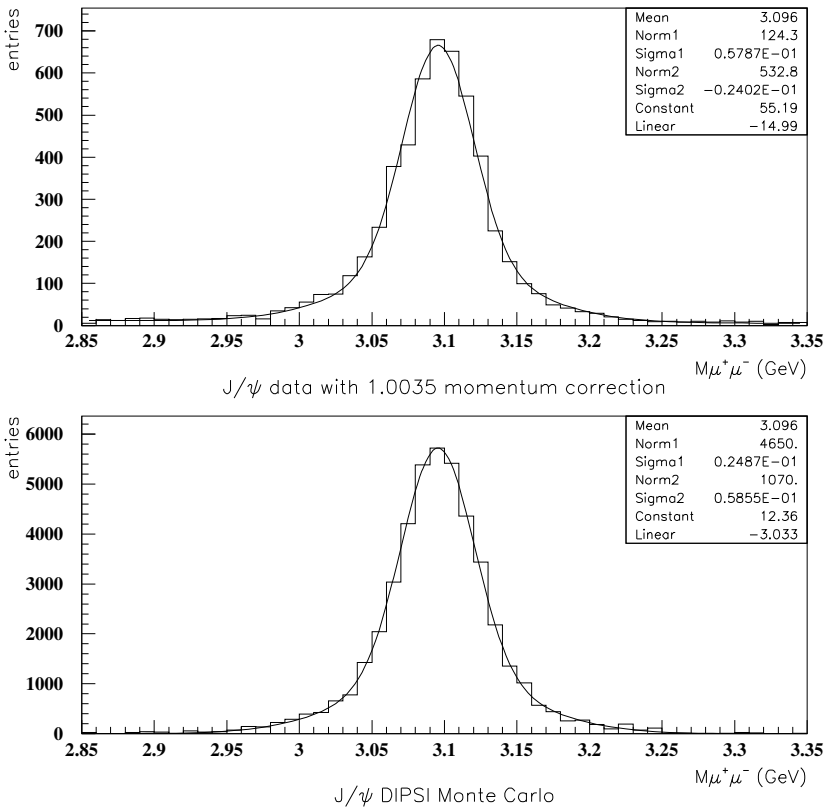

Figure 4.9: Data and Monte Carlo $\mu^+\mu^-$ invariant mass plot for events with tracks with at least 5 CTD superlayers. The mass peak (Mean= 3.096 GeV) of a double gaussiam fit is correctly described after a momentum correction of 0.35% on the data.

are compared for events after the selection described in previous chapter and within an invariant mass window of $2.85 < M_{\mu^+\mu^-} < 3.25$. The efficiency and momentum corrections described above were included in the detector simulation.

The DIPSI Monte Carlo δ and b parameters that appear in the W^{δ} and $e^{-b|t|}$ slopes of the γp cross section were tuned at generation level in order to describe the experimental slopes obtained from the data.

Figure 4.10 shows the muon momenta distributions and their angular distributions. The distributions are presented separately for positive and negative tracks. The overall agreement is sufficiently satisfactory.

In figure 4.11 the W and p_T^2 as well as the helicity angle distributions (Θ_h, $\cos\phi_h$) are shown for data and Monte Carlo. For the p_T^2 a disagrement in the exponential shape can be observed with a smoother fall at high p_T^2 of the data with respect to the Monte Carlo. This can be explained by the proton diffractive background still present in the current selection.

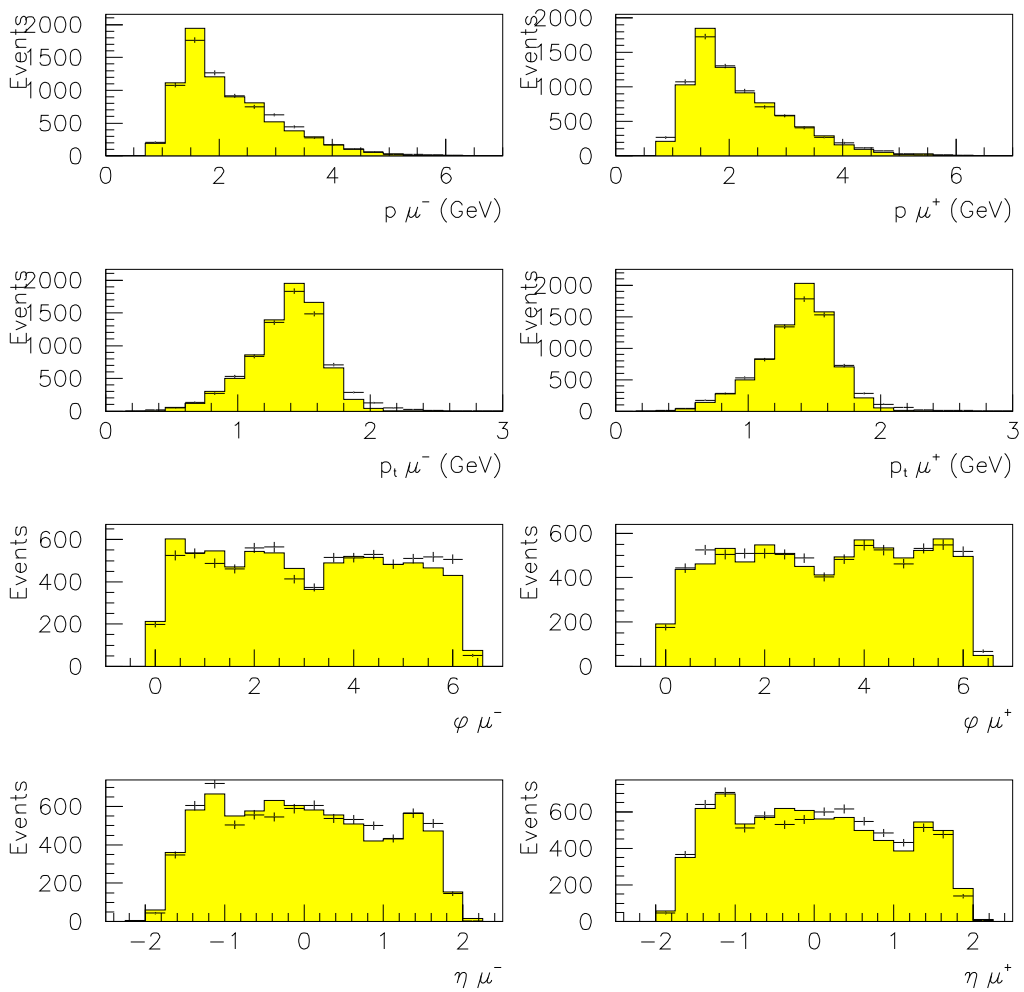

Figure 4.10: Data distributions of muon momenta and angular distributions for positive and negative tracks after the full selection. The solid histograms are from the DIPSI Monte Carlo after corrections.

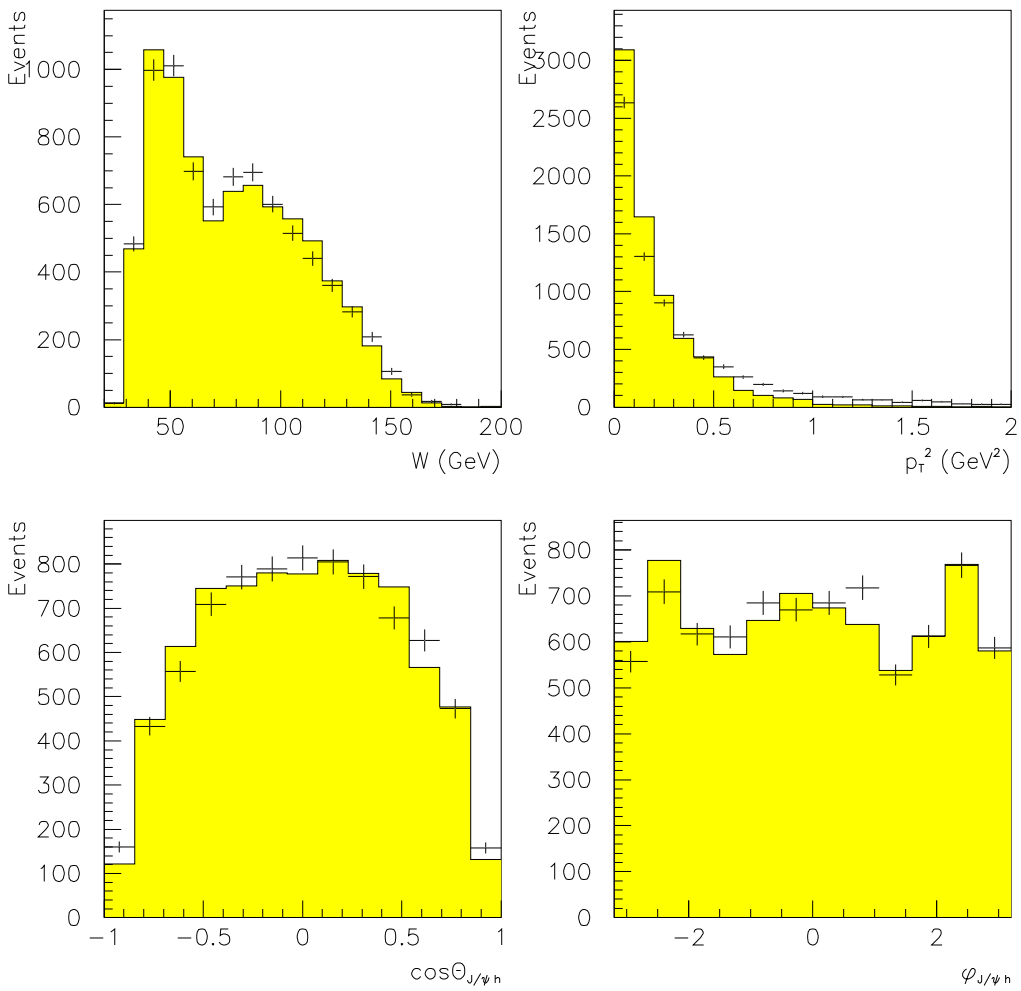

Figure 4.11: Data distribution of the main J/ψ kinematic variables after the full selection: W , p_T^2 and the helicity angles $\cos\Theta_h$ and ϕ_h. The solid histograms are from the DIPSI Monte Carlo after the Monte Carlo corrections.

Chapter 5

Signal Extraction

5.1 Background Studies

The selection criteria described earlier were designed to select elastically produced J/ψ mesons decaying in a couple of muons. While being effective for the removal of events with different decaying products and kinematics, the selection cuts may not be able to remove contributions from other processes characterized by similar kinematics and detector signatures. These contributions have to be evaluated and removed before any quantitative measure can be extracted from the data. In this respect the most important tool is the comparison of data sample with the specifically Monte Carlo generated events.

For this analysis the main background sources are the non resonant background due to the lepton pair production by a $\gamma\gamma$ fusion and a resonant background where the proton diffracts into a higher mass state. While in the first case the background contribution can be evaluated by looking in the region outside the resonance peak of the interested signal, in the second a different approach has to be provided.

5.2 Non-Resonant Background

5.2.1 The Bethe-Heitler Process

The lepton pair production by $\gamma\gamma$ fusion, also known as Bethe-Heitler process as described in section 1.7.3, has a very similar topology as compared to the elastic J/ψ events. The lepton pair is produced when a photon radiated by the electron interacts with a photon radiated by the proton to form the pair of oppositely charged leptons. Since the leptons do not come from a particle decay the invariant mass spectrum has the typical non resonant shape as shown in Fig.5.1. The LPAIR Monte Carlo expectation normalized to the entries in regions outside the mass peak [1] is superimposed in the same figure.

Once the background contribution is subtracted, the distribution shows a clean J/ψ peak with no entries outside the resonant region. At the invariant mass of 3.68 GeV

[1] Depending on the W and t range studied, different invariant mass regions were used for the Monte Carlo background normalization. In Fig. 5.1 the background was normalized in the regions $1.8 < M_{\mu^+\mu^-} < 2.5$, and $4.0 < M_{\mu^+\mu^-} < 7.0$ GeV.

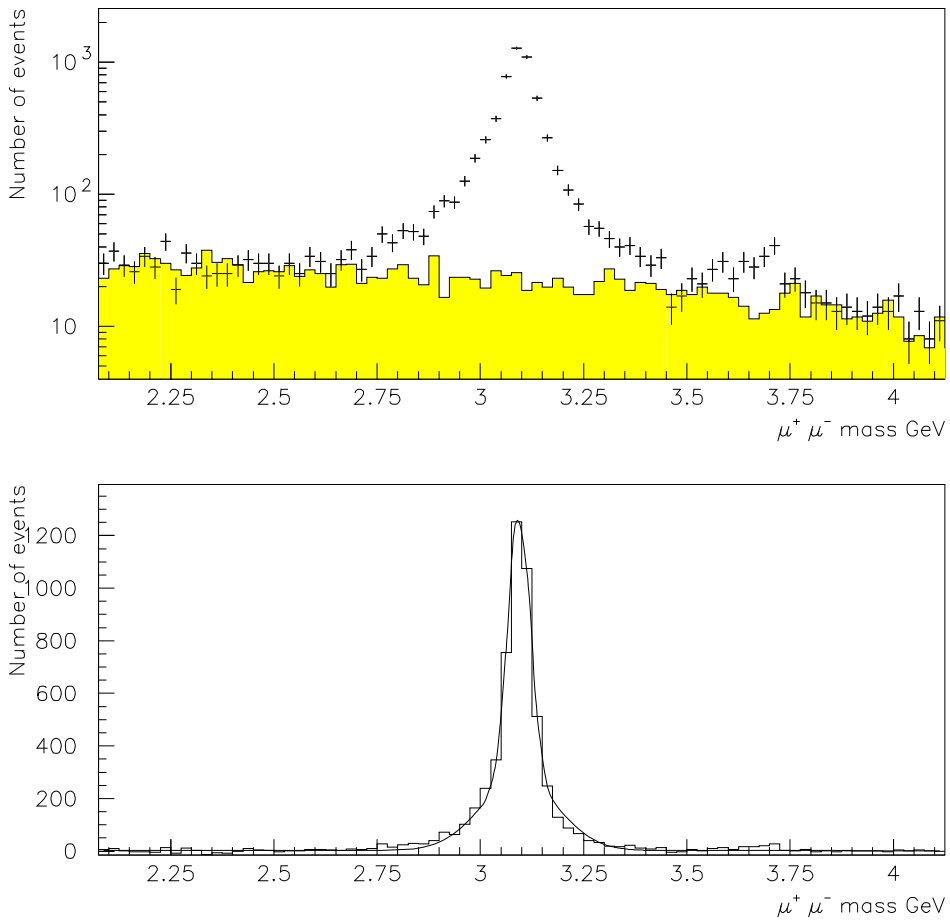

Figure 5.1: Invariant mass of the $\mu^+\mu^-$ system for whole data sample after all selection cuts excluding the mass. The Monte Carlo distribution for the $\gamma\gamma \rightarrow \mu^+\mu^-$ Bethe Heitler process normalized to the data in the region outside the resonance is superimposed to the data. In the second histogram the signal (in linear scale) after background subtraction fitted to a double gaussian. Note that in the histogram the abscissa axis is slighlty shifted from origin to display the small fluctuations around zero due to the background subtraction.

also the ψ' peak has become observable.

The subtraction was also performed in different bins of W and t. In this case, to minimize errors due to lower statistics, different approaches were followed:

- performing a direct bin by bin subtraction of the MC sample from the data sample,
- using a polynomial and an exponential fit to the MC distribution for the background estimation and subsequent subtraction.

In Figures 5.2 and 5.3 the invariant mass distributions for data and for non resonant Monte Carlo are superimposed and subtracted for different W ranges. The Monte Carlo was normalized to the data in a region at least 3 σ outside from any known resonance region and when dealing with systematics the range was changed in order to evaulate the uncertainty in the subtraction.

5.3 Resonant Background

5.3.1 Proton Dissociation

In the J/ψ production with diffractive dissociation the incoming proton is excited into a higher mass state which then decays into final state hadrons. These proton remnants are boosted in the forward direction at very small polar angle and may escape undetected through the beam pipe especially at low t. Cuts on the energy deposit in the first FCAL ring around the beam pipe (as described in chapter 3) help only relatively since most likely the decay products will escape undetected.

To evaluate the proton dissociation contamination, the information of the Proton Remnant Tagger (see 2.8) was used.

Events with proton dissociation will more likely deposit energy at small angle and be tagged by the sections of the PRT. By comparing the fractions of events with a PRT tag separately for data and for the elastic and dissociative Monte Carlos an estimate of the contamination can be extracted.

Going a bit more into detail, we introduce the fraction of PRT tagged events

$$\mathcal{F} = \frac{N^{tag}}{N_{total}}. \tag{5.1}$$

The unknown proton dissociative fraction ξ_{pd} satisfies the relation:

$$\mathcal{F}_{data} = \xi_{pd}\mathcal{F}_{elas} + (1 - \xi_{pd})\mathcal{F}_{diss} \tag{5.2}$$

where $\mathcal{F}_{elas}$ and $\mathcal{F}_{diss}$ are extracted from the elastic (DIPSI) and diffractive (EPSOFT) Monte Carlo respectively. Thus for each W and/or p_T^2 bin, ξ_{pd} can be extracted as:

$$(\xi_{pd})_{W,p_T^2} = \left(\frac{\mathcal{F}_{data} - \mathcal{F}_{diss}}{\mathcal{F}_{elas} - \mathcal{F}_{diss}}\right) \tag{5.3}$$

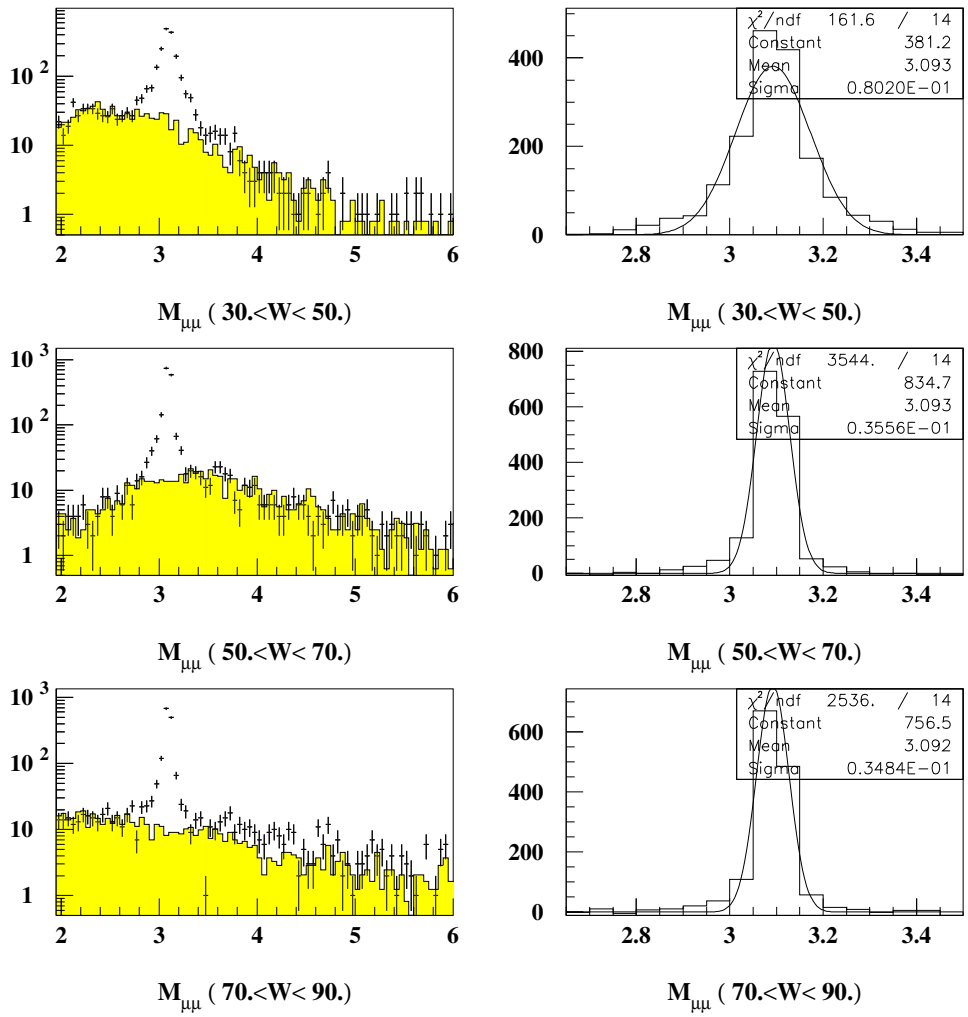

Figure 5.2: $\mu^+\mu^-$ invariant mass distribution for the first three W bins as previously defined $30 < W < 90$ GeV. before (left) and after (right) the subtraction of the non resonant background. Data (points) and Monte Carlo (histograms) were normalized in the region of $1.8 < M_{\mu^+\mu^-} < 2.5$ and $4.0 < M_{\mu^+\mu^-} < 6.0$ GeV.

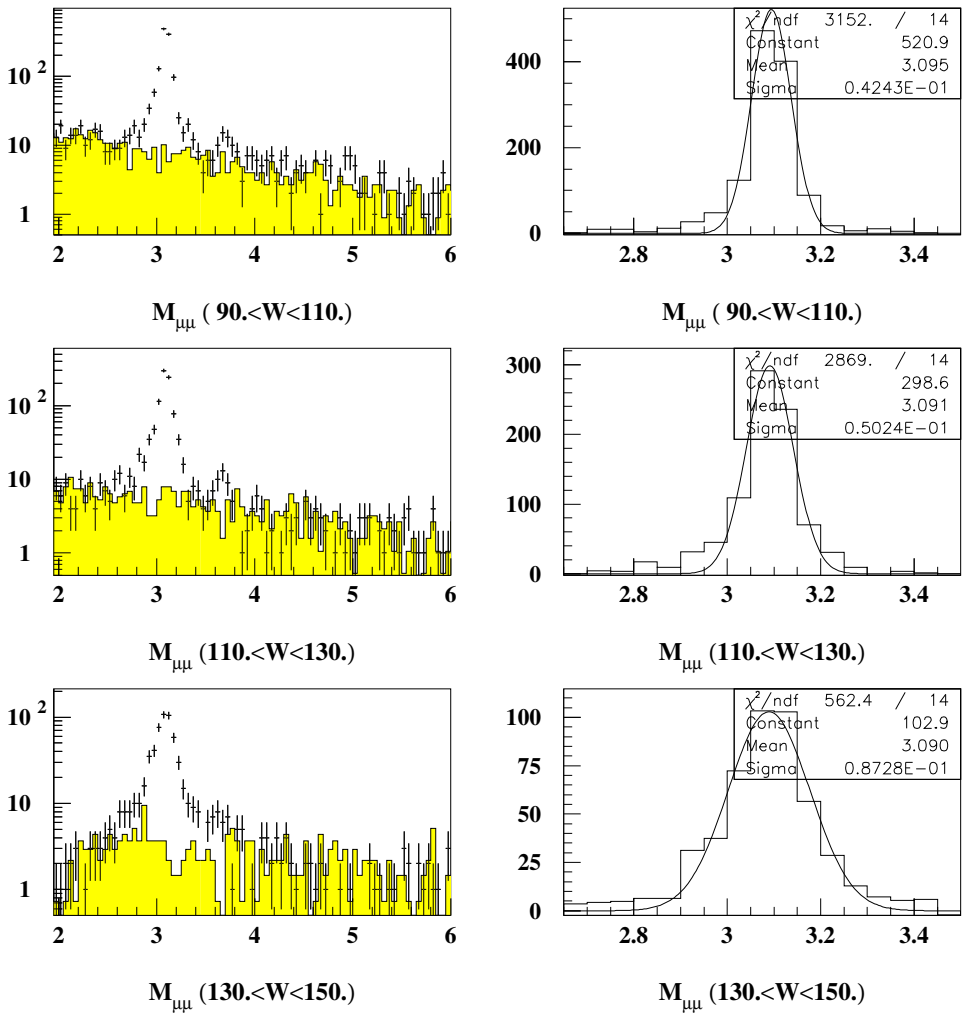

Figure 5.3: $\mu^+\mu^-$ invariant mass distribution for the second three W bins as previously defined $90 < W < 150$ GeV. before (left) and after (right) the subtraction of the non resonant background. Data (points) and Monte Carlo (histograms) were normalized in the region of $1.8 < M_{\mu^+\mu^-} < 2.5$ and $4.0 < M_{\mu^+\mu^-} < 6.0$ GeV.

In Fig.5.4 the fraction of selected events with a tag in the PRT1 or PRT2 is plotted for different W and p_T^2 bins. Both taggers show an almost flat distribution in W while at high values of p_T^2 a higher tagged fraction is revealed.

In Fig.5.5 the proton dissociative fraction is plotted as extracted using formula 5.3 in bins of W using the information of PRT1 and PRT2. The proton dissociative background appears to be reasonably flat in W and with an average contribution of about 20 %.

On the contrary the linear increase as a function of p_T^2 observed in Fig.5.6 can be explained by the different t slopes of the elastic and dissociative cross section respectively. The obtained values range from about 10% at $p_T^2 = .1$ GeV^2 up to 60 % in the highest p_T^2 bin. The result from a linear fit is also shown in Fig. 5.6.

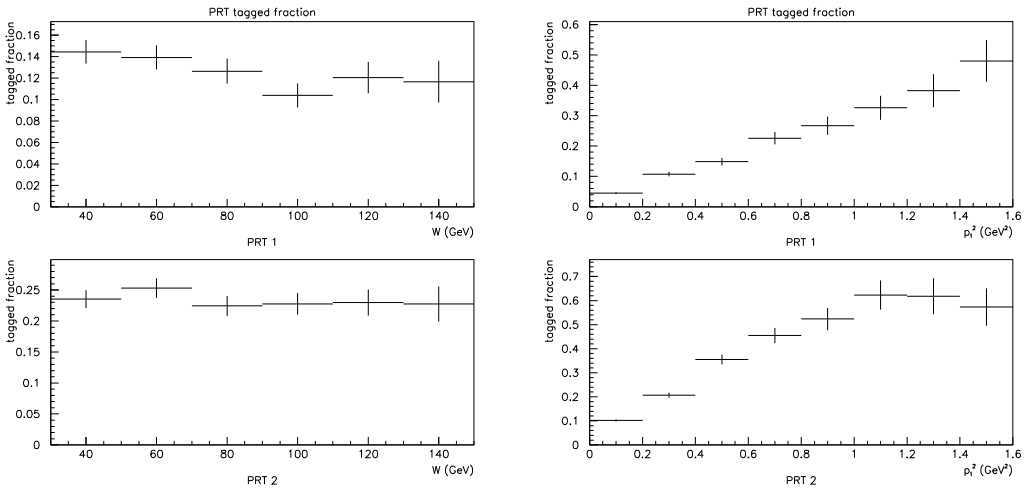

Figure 5.4: The fraction of the selected events with a tag in the PRT1 or PRT2 as a function of W and p_T^2.

5.3.2 ψ' Contamination

The ψ' [2] contribution was evaluated using different DIPSI Monte Carlo samples. A sample of 20000 events of $\psi' \to \mu^+\mu^-$ was used to evaluate the contribution of the 3.68 GeV mass peak. The sample was processed through the same selection as for the J/ψ study. An acceptance of 25.8 ± 0.1(stat) % was obtained. Figure 5.7 shows the reconstructed invariant $\mu^+\mu^-$ mass spectra in the mass range $2.0 < M_{\mu^+\mu^-} < 6.0$ GeV and a fit on the data. The gaussian function, which was used to fit the ψ' signal gives a ψ' mass of 3.7 GeV. The number of events estimated from the fit in the mass range $3.5 < M_{\mu^+\mu^-} < 4.0$ GeV is 208 ± 30. Using this information toghether with

[2]The ψ' is the $2s$ $c\bar{c}$ vector meson state with a mass $M_{\psi'} = 3.686 \pm 0.09$ GeV. Among the various decay modes the ψ' decays into a muon pair with a branching ratio of 0.77 ± 0.17% and into a $J/\psi\pi^0\pi^0$ with a branching ratio of 17.9 ± 1.8%

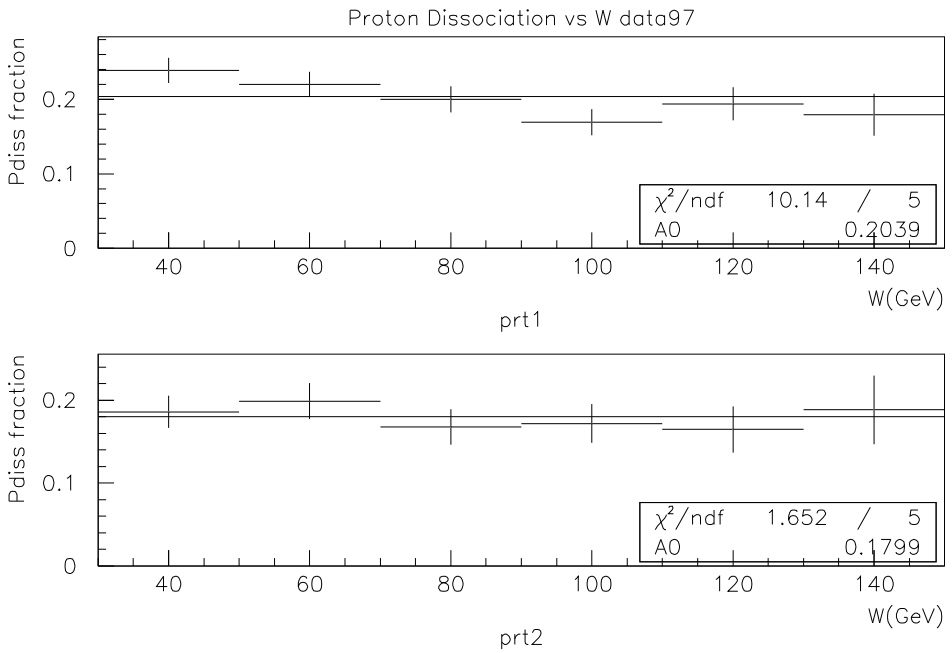

Figure 5.5: The final fraction of proton dissociative events in the data as extracted from the PRT using the DIPSI and EPSOFT Monte Carlo. The data sample was restricted to the mass range ($2.9 < M_{\mu^+\mu^-} < 3.3$). The fraction appears pretty flat in W and at around 20%.

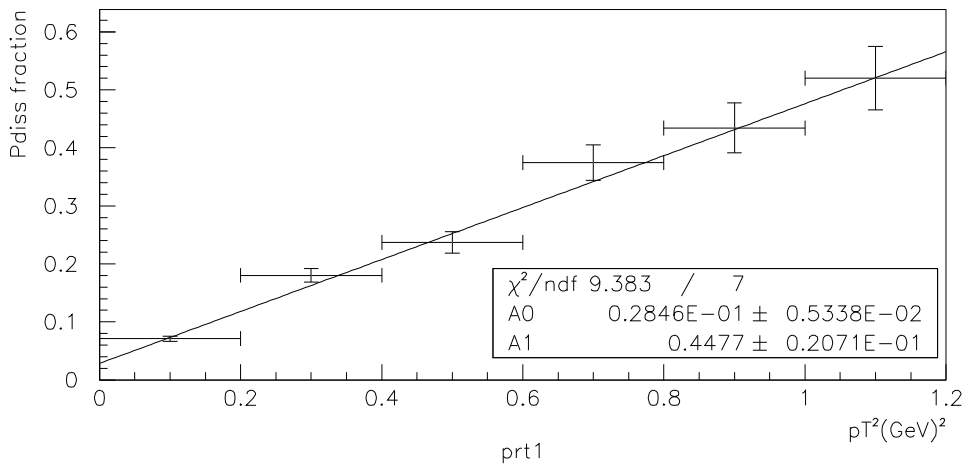

Figure 5.6: The fraction of proton dissociative events in the data as extracted from the PRT1 using the DIPSI and EPSOFT Monte Carlo. The data sample was restricted to the mass range ($2.9 < M_{\mu^+\mu^-} < 3.3$). The fraction increases almost linearly with p_T^2. This behaviour can be easily understood as due to the different t slope of the elastic and dissociative processes. At higher t, since elastic events have a steeper fall, almost only dissociative events will be present.

the luminosity, the branching ratio and the acceptance previously calculated, a cross section can be extracted $\sigma_{ep\to eN\psi'} = 2.75 \pm 0.30$ nb. This result is compatible with the current measurements by H1 [50]. The number of events from ψ' production present in the J/ψ elastic sample via the decay $\psi' \to J/\psi\pi^0\pi^0$ can now be estimated using the formula

$$N = \sigma_{ep\to eN\psi'} \mathcal{L} \mathcal{A} \mathcal{B}_{\psi'} \mathcal{B}_{J/\psi} \tag{5.4}$$

where $\mathcal{L}$ is the luminosity, $\mathcal{B}_{\psi'}$ is the branching ratio for $\psi' \to J/\psi\pi^0\pi^0$ and $\mathcal{B}_{J/\psi}$ is the usual di-muon decay of the J/ψ. The acceptance for the process $\psi' \to J/\psi\pi^0\pi^0$ has been estimated using a DIPSI Monte Carlo ($\psi' \to J/\psi\pi^0\pi^0$) sample leading to a value $\mathcal{A} \simeq 8.0 \pm 0.1(stat)\%$. A final contamination of $2. \pm 0.5$ % assumed flat in W and p_T^2 when compared to the J/ψ distributions was estimated.

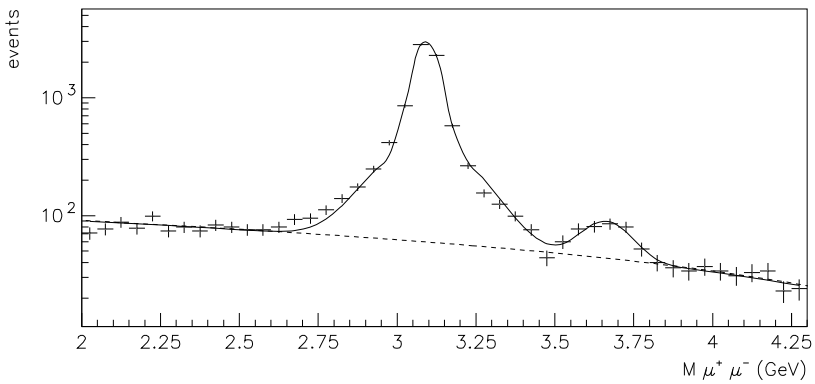

Figure 5.7: The mass distribution $M_{\mu^+\mu^-}$ from the data in the J/ψ and ψ' region. The solid line shows the result of a fit to the sum of a double gaussian (J/ψ), a single gaussian (ψ') and a linear background.

Chapter 6

Results

6.1 Procedure for Obtaining a Cross Section

The cross section for J/ψ production in the reaction $ep \rightarrow eJ/\psi p$ is given by the formula:

$$\sigma_{ep\rightarrow J/\psi p} = \frac{N_{corr}}{\mathcal{L} \cdot \mathcal{A} \cdot \mathcal{B}} \tag{6.1}$$

where N_{corr} is the number of J/ψ candidates after background subtraction, $\mathcal{L}$ the integrated luminosity, $\mathcal{A}$ the acceptance including all detector efficiency corrections and $\mathcal{B}$ the muonic decay branching ratio. The value used in this analysis is $B = 6.01 \pm 0.19$ [51]. $\mathcal{N}_{corr}$ is obtained as

$$N_{corr} = (N_{obs} - N_{BH}) \left(1 - \mathcal{F}_{\psi'}\right) (1 - \mathcal{F}_{pdiss}) \tag{6.2}$$

where N_{BH} is the non resonant background, mainly the Bethe-Heitler process and $\mathcal{F}_{pdiss}$ and $\mathcal{F}_{\psi'}$ are the fractions of proton diffractive and ψ' contribution present after the non resonant background subtraction.

6.2 Photoproduction Cross Section

As already anticipated in chapter 1, the photoproduction γp cross section is related to the ep cross section by

$$\sigma = \frac{\int \Phi(y, Q^2) \sigma_{\gamma p\rightarrow J/\psi p}(y, Q^2) dy dQ^2}{\int \Phi(y, Q^2) dy dQ^2} = \frac{\sigma_{ep\rightarrow eJ/\psi p}}{\Phi_T} \tag{6.3}$$

where $\sigma_{ep\rightarrow eJ/\psi p}$ is the mean cross section in a range of measured W while Φ_T is the effective flux of virtual photons accompanying the positron. The integral runs over the full range of Q^2 and from $y_{min} = W^2_{min}/s$ to $y_{max} = W^2_{max}/s$ where W_{min} and W_{max} are the minimum and maximum values for W respectively. The effective photon flux is computed as:

$$\Phi_T = \frac{\alpha}{2\pi}\int_{y_{min}}^{y_{max}}\left[\frac{1+(1-y)^2}{y}\ln\left(\frac{Q^2_{max}(y)}{Q^2_{min}(y)}\right)+\frac{2(y-1)}{y}\left(1-\frac{Q^2_{min}(y)}{Q^2_{max}(y)}\right)\right]dy \tag{6.4}$$

where α is the electromagnetic coupling constant and $M_e^2\frac{y^2}{1-y} < Q^2 < 1$ GeV.

6.3 Systematic Uncertainties

Several sources contributed to the systematic uncertainties in the elastic J/ψ cross section measurement. Below follows a list of the sources that were considered and the relative uncertainty.

- Trigger
  - Muon chambers trigger efficiency 10% (cf. 4.4).
  - Central tracking trigger efficiency 5% (cf. 4.4).
- Uncertainty in the acceptance estimation 3%

  The standard analysis uses DIPSI for acceptance evaluation. This acceptance was checked using a different Monte Carlo, namely DIFFVM [1]. In table 6.1 the acceptances in the usual W bins are compared for the DIPSI and DIFFVM generators.
- Offline selection Cuts

  The systematic errors associated with the selection procedure were estimated varying each cut within a range determined by the resolution. Among others the cuts on
  - energy in the first ring of the FCAL,
  - mip requests,
  - elasticity,
  - cosmic rejection,

  described in sections 3.6 and 3.7 were included in the study.
- Estimation of the number of signal events
  - Proton diffractive dissociation subtraction.
    It has been estimated using a sample of DIFFVM Monte Carlo events.

[1] DIFFVM [52] is an unweighted Monte Carlo generator based on (soft) Regge phenomenology and the Vector meson Dominance Model. It simulates diffractive processes in ep scattering, such as elastic vector meson production ($ep \to eVp$) and vector meson production with proton dissociation ($ep \to eVN$) as well as single and double diffractive dissociation ($ep \to eXp,\ ep \to eXN$).

  - Non resonant background subtraction.
    It has been estimated by varying the method of the background subtraction (cf. 5.2.1).
  - ψ' contamination (cf.5.3.2)

- Global factors
  - Branching Ratio
    The uncertainty on the Branching Ratio $J/\psi \to \mu^+\mu^-$ was taken as given in [51].
  - Luminosity.
    An uncertainty of 2% on the luminosity determination was assumed in agreement with the recommendations of the ZEUS Collaboration.
  - Photon Flux factor Φ_T
    An uncertainty of 2% was assumed.

The results are summarized in table 6.2. Summing up in quadrature the various contributions the systematic error on the cross section normalization is of the order of 15%.

W range	DIPSI	DIFFVM
$30 < W < 50$	25.96%	25.75%
$50 < W < 70$	31.61%	30.91%
$70 < W < 90$	34.82%	34.92%
$90 < W < 110$	36.00%	34.96%
$110 < W < 130$	28.62%	28.88%
$130 < W < 150$	16.55%	17.10%

Table 6.1: Detector and selection acceptance obtained from from the DIPSI and DIFFVM Monte Carlo generators. The differences are within 4 %.

6.4 Elastic Cross Sections in W bins

The cross sections σ_{ep} and $\sigma_{\gamma p}$ have been determined in the range $30 < W < 150$ in 6 W bins as introduced in section 4.3.1.

Efficiency corrections and background subtraction were applied as described in previous chapter. The results are summarized in table 6.4.

In Fig.6.1 the ep cross section is drawn as a function of W. After convolution with the photon flux factor, the extracted $\sigma_{\gamma p}(W)$ is shown in Fig.6.2. A fit to a function $\sigma(W) \propto W^{\delta}$ gives $\delta = 0.67 \pm 0.05$ (stat) ± 0.05 (syst). The measured value shows a much steeper W dependence as expected from perturbative QCD calculations and is clearly not in agreement with a Regge-like soft pomeron model as for light vector mesons ($\delta \approx 0.22$). In Fig.6.3 the same points are compared to data from previous H1

Breakdown of Contributions to the Systematic Error *Values are quoted in percent*						
W bin (GeV)	30-50	50-70	70-90	90-110	110-130	130-150
CTD Trigger	$^{+5}_{-5}$	$^{+5}_{-5}$	$^{+5}_{-5}$	$^{+5}_{-5}$	$^{+5}_{-5}$	$^{+5}_{-5}$
Muon Chamber Trigger	$^{+10}_{-10}$	$^{+10}_{-10}$	$^{+10}_{-10}$	$^{+10}_{-10}$	$^{+10}_{-10}$	$^{+10}_{-10}$
Elastic definition	$^{+1}_{-3}$	$^{+1}_{-3}$	$^{+1}_{-3}$	$^{+1}_{-3}$	$^{+1}_{-2}$	$^{+1}_{-2}$
Cosmic rejection	$^{+0}_{-0}$	$^{+0}_{-0}$	$^{+0.5}_{-2}$	$^{+0}_{-0}$	$^{+0}_{-0}$	$^{+0}_{-0}$
Other selection cuts	$^{+4}_{-4}$	$^{+4}_{-4}$	$^{+3}_{-4}$	$^{+2}_{-4}$	$^{+4}_{-6}$	$^{+4}_{-5}$
Acceptance	$^{+3}_{-3}$					
BH subtraction	$^{+3}_{-3}$					
Proton dissociation	$^{+9}_{-6}$					
ψ' contamination	$^{+1}_{-1}$					
Luminosity	± 2					
Photon Flux	± 2					
Branching ratio	± 3.2					
Total Systematic Errors						
W bin (GeV)	30-50	50-70	70-90	90-110	110-130	130-150
Total	$^{+16.1}_{-14.9}$	$^{+16.1}_{-14.9}$	$^{+15.9}_{-15.0}$	$^{+15.9}_{-14.9}$	$^{+16.1}_{-15.4}$	$^{+16.1}_{-15.0}$

Table 6.2: The contributions to the systematic errors on the J/ψ photoproduction cross section.

and ZEUS measurements and from results of lower energy measurements. Superimposed are theoretical curves by Frankfurt et al. [53] based on the latest gluon density parametrizations. Even if the measurement would allow to discriminate between the available parametrizations, the uncertainty in the normalization prevents from drawing final conclusions.

The obtained values are slightly higher, but compatible with the new H1 measurement [65] done on a comparable statistical sample. The previous measurements of ZEUS[63], done in a smaller W window and with a lower statistics and based the 1994 data-taking period, appear to be slighlty below.

6.5 b Slope Extraction

In this section the t dependence of the cross section in different ranges of W is studied in order to investigate for shrinkage effects as described in section 1.4.

The measurement was done by subdividing the whole selected data sample in bins of W and t in order to extract for each W range the t dependence of the cross section. In Fig.6.4 the invariant mass spectra of the selected sample are drawn for each W and

W range	Flux	$y \times 10^{-2}$
$30 < W < 50$	0.05375	$0.997 < y < 2.771$
$50 < W < 70$	0.03199	$2.771 < y < 5.431$
$70 < W < 90$	0.02175	$5.431 < y < 8.979$
$90 < W < 110$	0.01584	$8.979 < y < 13.41$
$110 < W < 130$	0.01200	$13.41 < y < 18.74$
$130 < W < 150$	0.00933	$18.74 < y < 24.94$

Table 6.3: Photon flux calculation for each W bin considered. The y ranges are also indicated. In the calculation $Q^2_{min} < Q^2 < 1$ was assumed.

W Range	N_{corr}	$\sigma_{ep\to eJ/\psi p}$ (nb)	$\sigma_{\gamma p\to J/\psi p}$ (nb)
$30-50$	1627 ± 47	$2.16 \pm 0.06^{+0.34}_{-0.32}$	$40.2 \pm 1.2^{+6.5}_{-6.0}$
$50-70$	1519 ± 44	$1.70 \pm 0.05^{+0.27}_{-0.25}$	$53.1 \pm 1.6^{+8.5}_{-7.9}$
$70-90$	1369 ± 41	$1.40 \pm 0.04^{+0.22}_{-0.21}$	$64.6 \pm 1.9^{+10.3}_{-9.6}$
$90-110$	1189 ± 37	$1.14 \pm 0.04^{+0.18}_{-0.17}$	$72.3 \pm 2.3^{+11.6}_{-10.8}$
$110-130$	824 ± 31	$0.99 \pm 0.04^{+0.16}_{-0.15}$	$82.9 \pm 3.1^{+13.3}_{-12.8}$
$130-150$	446 ± 24	$0.93 \pm 0.05^{+0.15}_{-0.14}$	$100. \pm 5.5^{+16.0}_{-15.0}$

Table 6.4: The results for the integrated photoproduction cross section as a function of W. For each W bin the corrected number of events after background subtraction is given. The γp cross section is obtained from the ep one by applying the photon flux factor calculated in table 6.3.

t bin.

After background subtraction, in Fig. 6.5 the cross section is presented as a function of t separately for each W bin. Each point was extracted using the formulas 6.1 and 6.2 and the established results for proton dissociative (as a function of W and t) and non resonant background contamination. In the same figure a fit to a function of the type $d\sigma_{\gamma p}/d|t| \propto e^{-b|t|}$ is done.

The results of the fits are summarized in Fig.6.6 where the b slope as a function of W is extracted in the hypothesis of presence or absence of shrinkage effects. The obtained values are (statistical error only):

$$b = 4.32 \pm 0.12 \text{ GeV}^{-2} \tag{6.5}$$

$$b = 4.31 \pm 0.12 + 4 \cdot (0.086 \pm 0.074) \cdot \ln\left(\frac{W_{\gamma p}}{90 \text{ GeV}}\right) \text{GeV}^{-2} \tag{6.6}$$

Due to the big uncertainties no definitive conclusion on this topic can be drawn even if little or no shrinkage seems to be favoured.

In Fig. 6.7 the same points are presented with other measurements from H1 [65], the previous ZEUS measurement [63] and a point from low energy data obtained from E401 [57]. A new fit using the low energy measurement with the values extracted in this analysis yields, in the two hypothesis of precence or absence of shrinkage, to the following results:

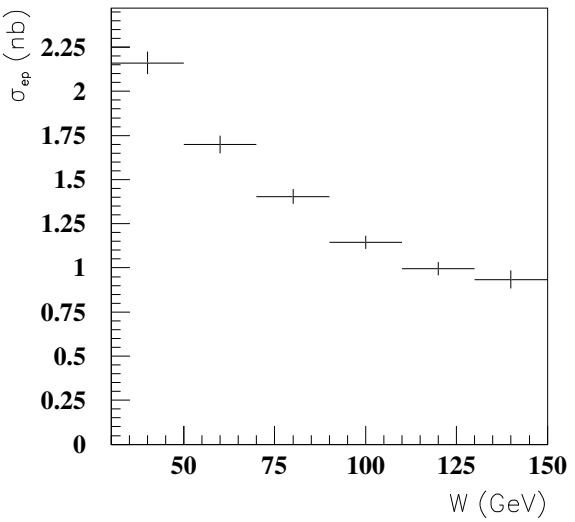

Figure 6.1: ep cross section of the elastic J/ψ photoproduction process for the different W bins.

$$b = 4.29 \pm 0.11 \text{GeV}^{-2} \qquad (\chi^2 = 0.85, \text{ndf} = 6) \tag{6.7}$$

$$b = 4.29 \pm 0.11 + 4 \cdot (0.111 \pm 0.059) \cdot \ln\left(\frac{W_{\gamma p}}{90 \text{ GeV}}\right) \text{GeV}^{-2} \qquad (\chi^2 = 3.05, \text{ndf} = 5).$$

Also in this case the value $b(W)$ turns out to be compatible with small or no shrinkage, the latter being predicted by the pQCD calculations.

The data are clearly compatible with being independent of $W_{\gamma p}$ even if shrinkage can however not be excluded in view of the errors.

This result is compatible with the previous ZEUS measurement [63] $b_t = 4.6 \pm 0.7$ GeV^{-2} in the smaller W range of $30 \leq W_{\gamma p} \leq 140$ GeV^{-2}.

6.6 Pomeron Trajectory

In this section, following a method proposed in [62], a calculation of the pomeron trajectory for the elastic J/psi photoproduction is performed. The data are again divided in W and t bins and the differential cross section $d\sigma/dt$ is calculated for each t bin as a function of W. The trajectory $\alpha_{I\!P}(t)$ is extracted for each t bin from a fit to a function

$$\frac{d\sigma}{dt}(W_{\gamma p}) = N \cdot \left(\frac{W_{\gamma p}}{90\text{GeV}}\right)^{4\alpha(t)-4} \tag{6.8}$$

using N and $\alpha(t)$ as free parameters. The resulting values of $\alpha(t)$ are then fitted to the form $a(t) = \alpha(0)_{I\!P} + \alpha' t$.

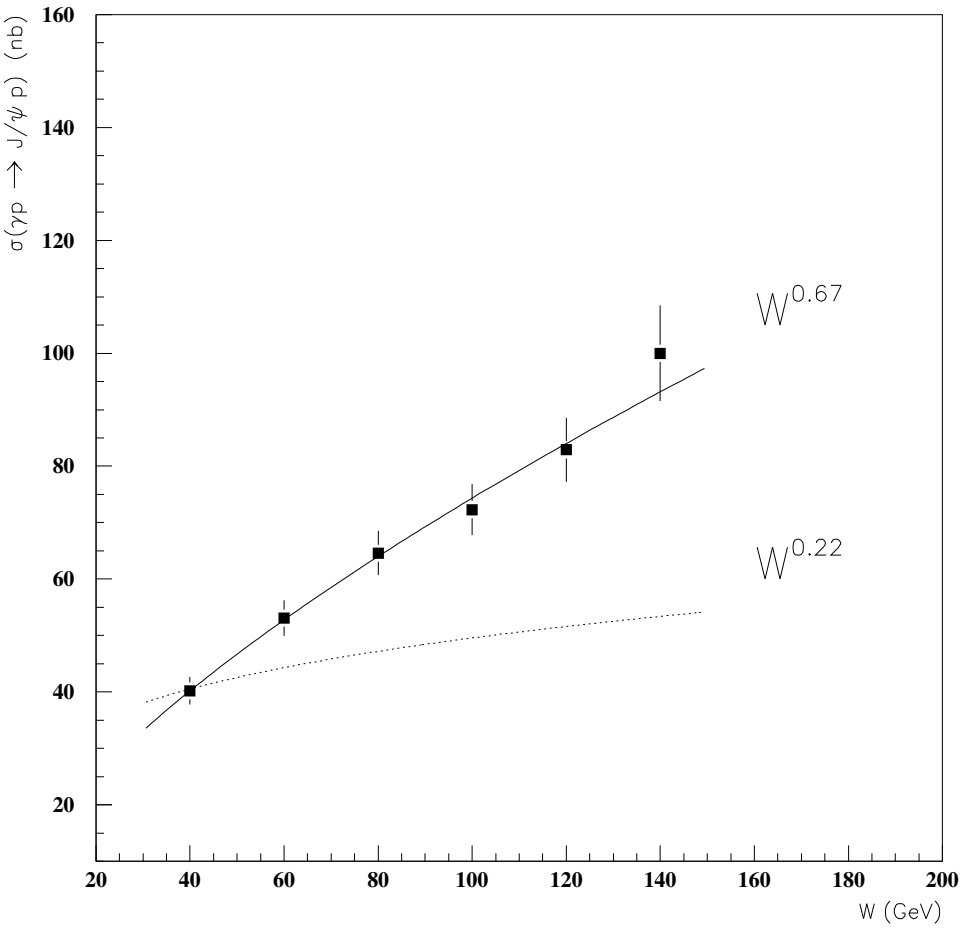

Figure 6.2: Elastic J/ψ photoproduction cross section as a function of W. The error bars are statistical only. The solid line shows the result of the fit to the data using the expression $\sigma_{\gamma p \to J/\psi p} \propto W^{\delta}_{\gamma p}$. The value $\delta = 0.67 \pm 0.05$ (stat) ± 0.05 (syst) was obtained from the fit. The dashed line shows the prediction of a soft pomeron model ($\delta \approx 0.22$) as used succesfully for the light vector meson case.

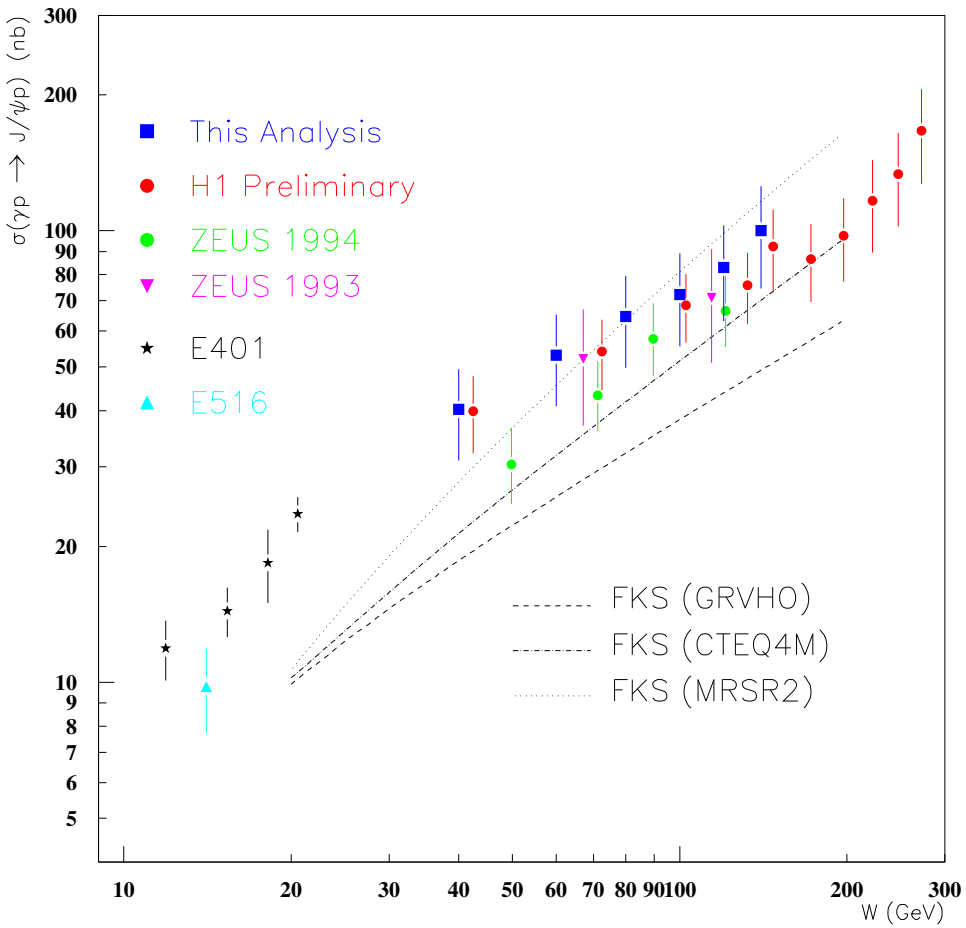

Figure 6.3: Elastic J/ψ photoproduction cross section as a function of W, obtained from this analysis and compared to previous measurements from ZEUS, H1 and fixed target experiments in the low W region. The error bars include statistic and systematic errors.

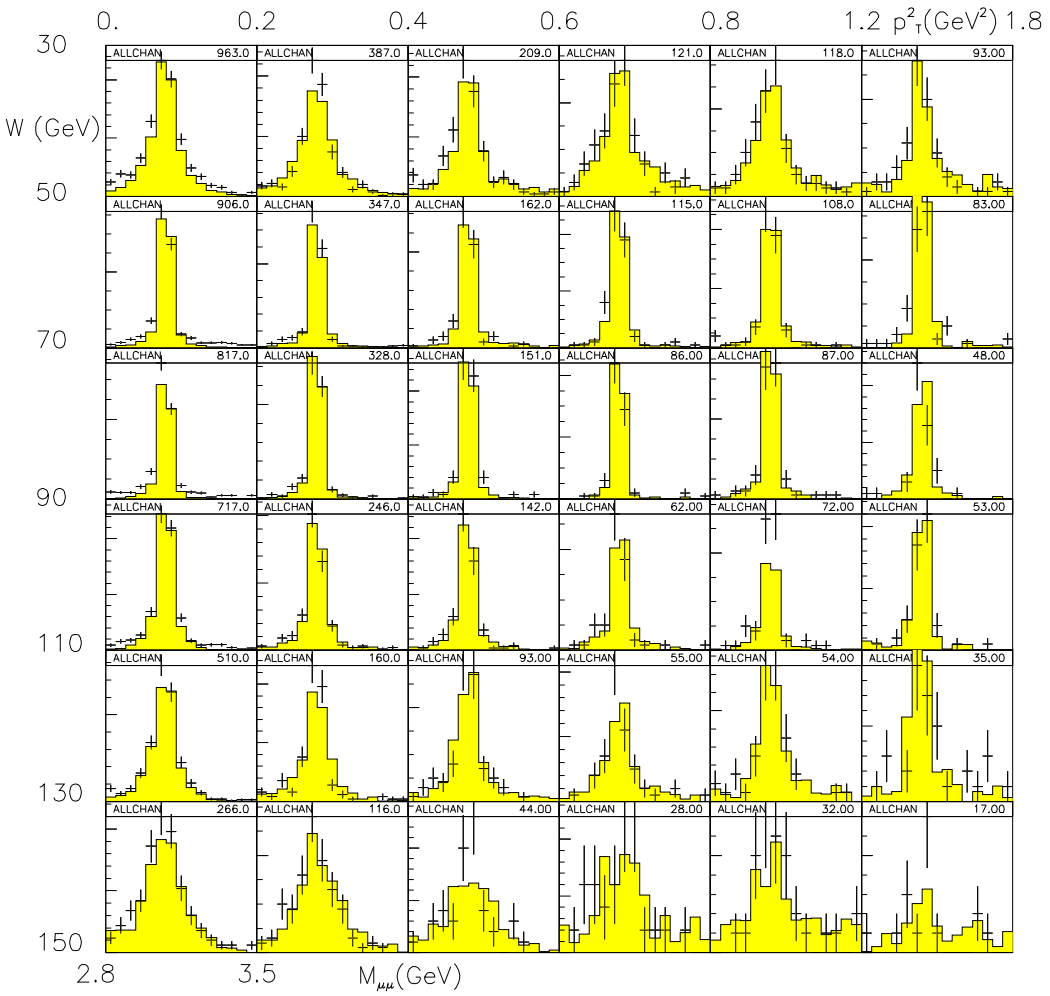

Figure 6.4: Invariant mass distributions for different bins of W and p_T^2. The full histograms refer to the DIPSI Monte Carlo simulation normalized to the data. The entries are corrected for Bethe-Heitler subtraction only. The invariant mass is displayed in the range $2.8 < M_{\mu^+\mu^-} < 3.5$. At high W the mass resolution appears to be worse in the Monte Carlo than in the data.

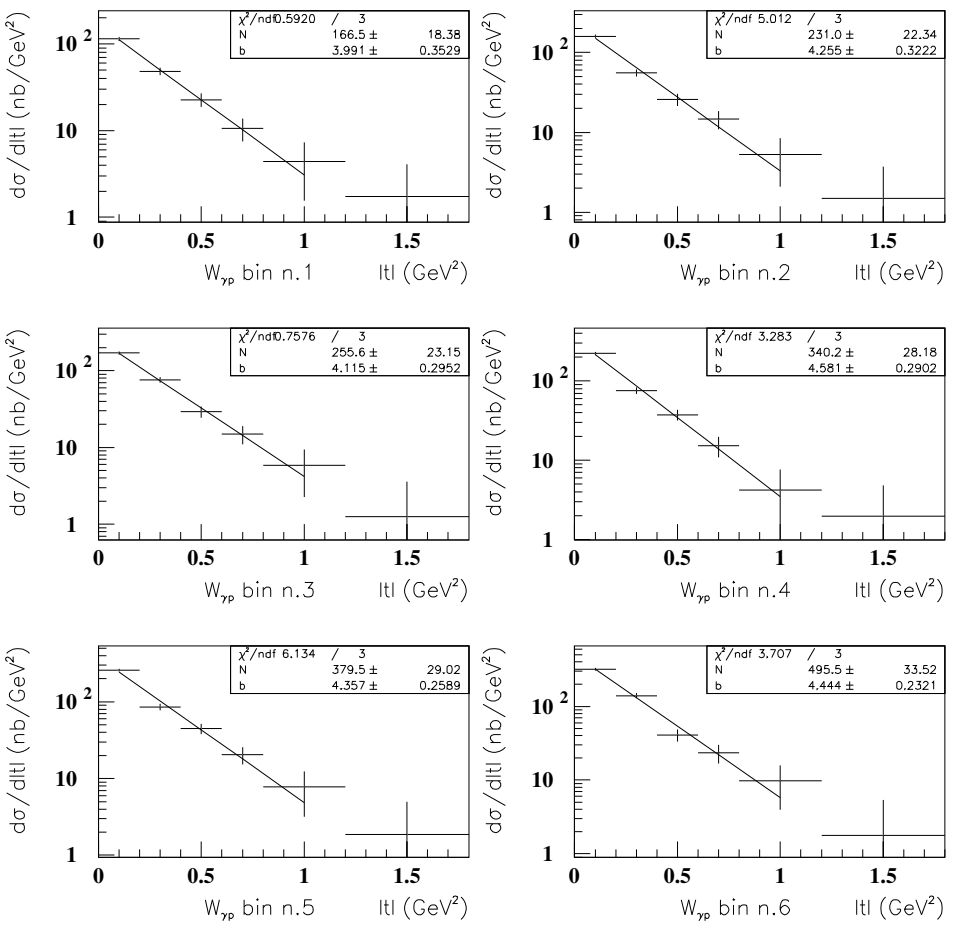

Figure 6.5: $d\sigma_{\gamma p}/d|t|$ for each W bin. A fit to $\frac{d\sigma}{dt} = Ne^{-b|t|}$ was done using the first 5 t points. The values obtained from the fit are indicated.

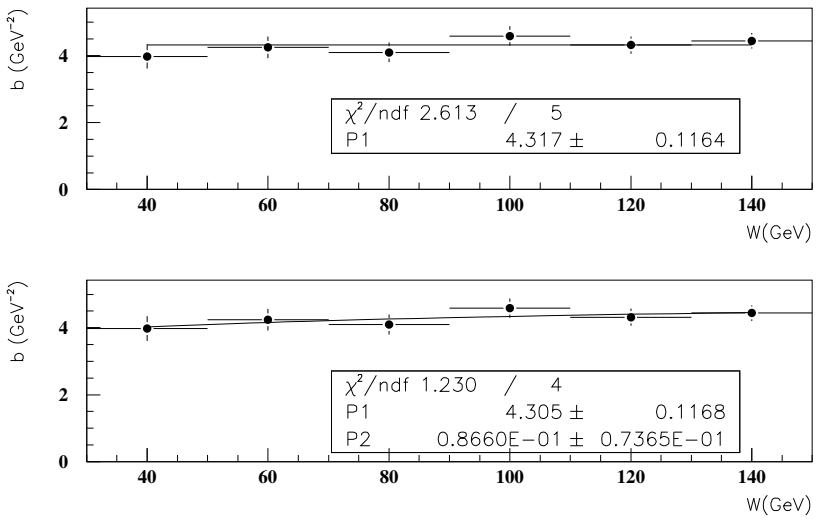

Figure 6.6: The result for b in the six $W_{\gamma p}$ bins from this analysis applying two different fitting models. In the first case assuming no shrinkage a vale $b = 4.32$ is obtained. In the second figure a fit is applied assuming shrinkage: The values of the fit and the χ^2 are indicated. Only statistical errors are shown. In both cases the χ^2 of the fit is good.

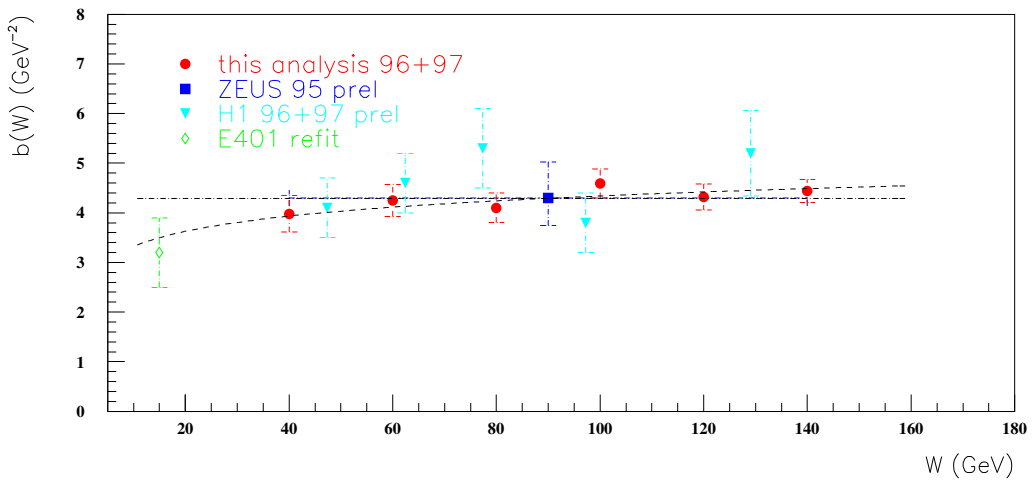

Figure 6.7: The result for b in the six $W_{\gamma p}$ bins from this analysis toghether with previous H1 and ZEUS measurements as well as an extrapolation from an E401 value. Two different fit results are shown, assuming the presence or the absence of shrinkage effects. The values of the fit are in the text.

In Fig.6.8 the $d\sigma/dt$ data points together with the described fit procedure are shown. The cross section shows the expected increase as already noticed when studying only the W dependence.

In Fig. 6.9 the results from the fits are put toghether and the trajectory is extracted. Both intercept and slope are not compatible with a soft pomeron model like the Donnachie-Landshoff that is superimposed for comparison. The values obtained are:

$$\alpha_{I\!P}(t) = 1.208 \pm 0.011 + (0.105 \pm 0.038)t$$

A hard pomeron contribution or a pQCD mechanism has to be invoked to justify the results. The value of α' is compatible within errors with the hypothesis of little or no shrinkage effects.

6.7 Decay Angular Distributions

In this section the decay angular distributions are studied. The J/ψ decay angular distributions can then be used to determine some matrix elements of the J/ψ spin density matrix. As previously mentioned, in the s-channel helicity frame the J/ψ is at rest and the quantization axis is taken to lie along the J/ψ direction in the photon-proton center of mass system. The decay angular distributions can thus be shown to be described by the formulas:

$$\frac{1}{N}\frac{dN}{d\cos\theta_h} = \frac{3}{8}\left[1 + r^{04}_{00} + \left(1 - 3r^{04}_{00}\right)\cos^2\theta_h\right], \tag{6.9}$$

$$\frac{1}{N}\frac{dN}{d\phi_h} = \frac{1}{2\pi}\left[1 + r^{04}_{1-1}\cdot\cos 2\theta_h\right], \tag{6.10}$$

where r^{04}_{00} and r^{04}_{1-1} are the parameters of the J/ψ spin density matrix introduced in section 1.6. Since $Q \approx 0$ i.e. the photon is real, the J/ψ is expected to be produced predominantly by transverse photons. If s-channel helicity is conserved, the spin density matrix parameters r^{04}_{00} and r^{04}_{1-1} should be close to zero. Under the assumption of SCHC, r^{04}_{00} can be related to the ratio of the photoproduction cross sections for longitudinal and transverse photons:

$$R = \frac{1}{\epsilon}\frac{r^{04}_{00}}{1 - r^{04}_{00}} \tag{6.11}$$

$$\epsilon = \frac{2\,(1-y)}{1 + (1-y)^2 - 2\,(1-y)\,\frac{Q^2_{min}}{Q^2}} \tag{6.12}$$

where ϵ is the virtual photon polarization, i.e. the ratio of the flux of longitudinally polarized photons to the flux of transversely polarized ones. The mean value of ϵ over the kinematic range of Q^2 and y sampled by the present experiment is $\epsilon = 1.043$

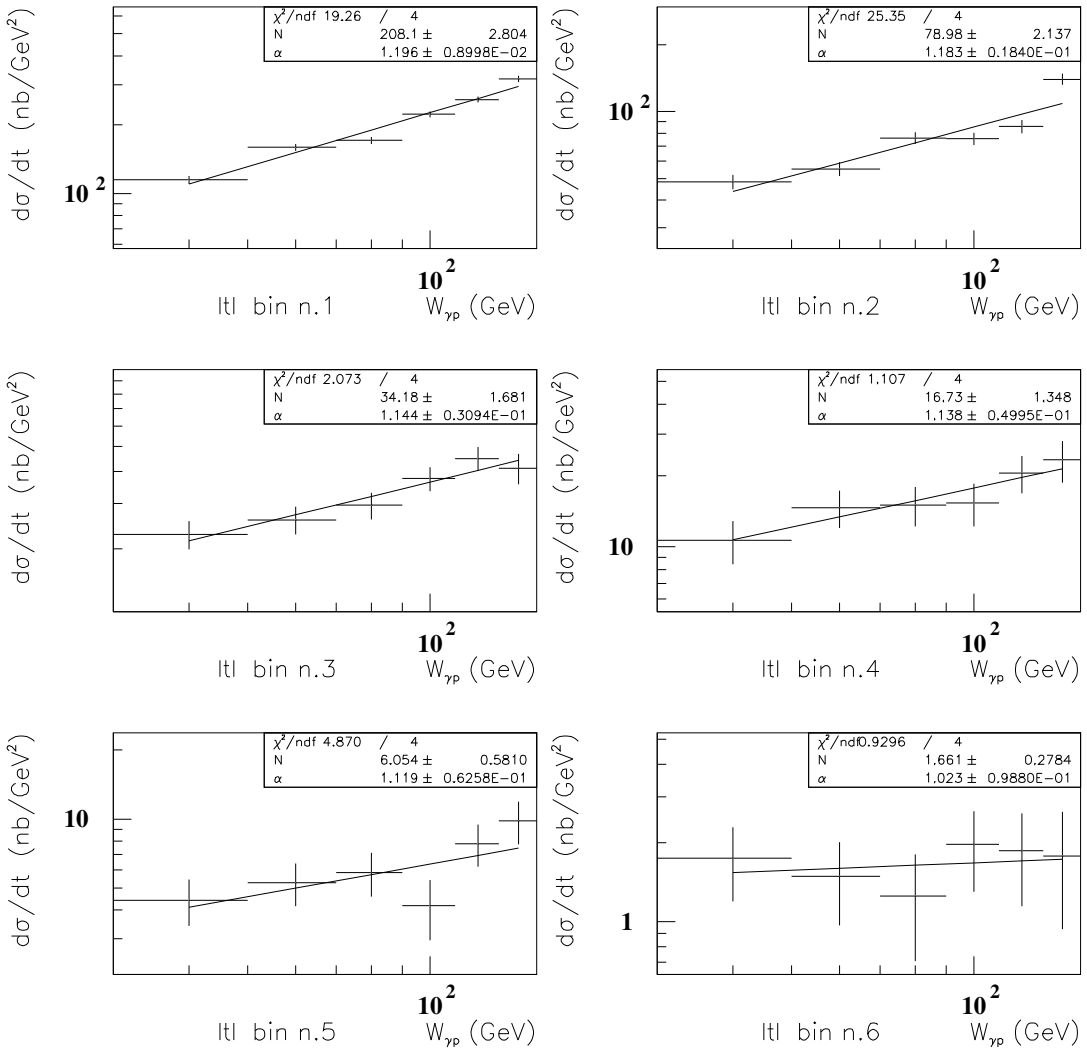

Figure 6.8: The W dependence in bins of $|t|$. Differential γp cross section $d\sigma/dt$ as a function of $W_{\gamma p}$ in bins of t toghether with a fit of the form $d\sigma/dt = NW_{\gamma p}^{\alpha}$.

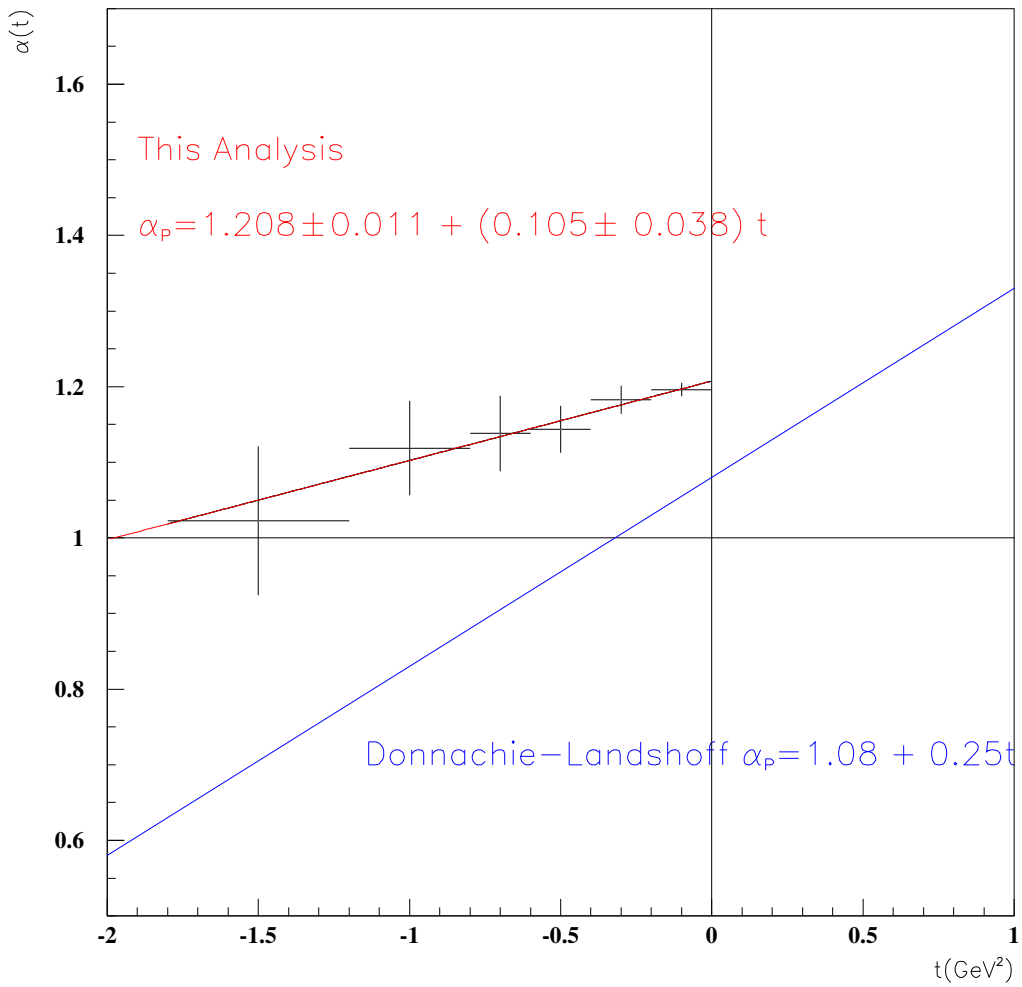

Figure 6.9: The measured Regge Trajectory $\alpha(t) = \alpha(0)_{I\!P} + \alpha' \cdot t$ for the elastic process $\gamma p \to J/\psi p$. The value from the fit is indicated. For comparison the soft Donnachie-Landshoff pomeron trajectory is superimposed.

The decay angular distributions are presented in Fig.6.10 in terms of cosθ_h and ϕ_h. No subtraction of dissociative contribution has been made since it is assumed that elastic and dissociative processes have same angular dependence. A fit has been used to determine r_{00}^{04}. The result, $-0.054 \pm 0.018 \pm 0.030$ (cf. table 6.5), gives $R = -0.05 \pm 0.09$ and is consistent with SCHC. A fit to the ϕ_h distribution has been made to determine r_{1-1}^{04}. Again the result $r_{1-1}^{04} = -0.08 \pm 0.017 \pm 0.035$ is consistent with SCHC.

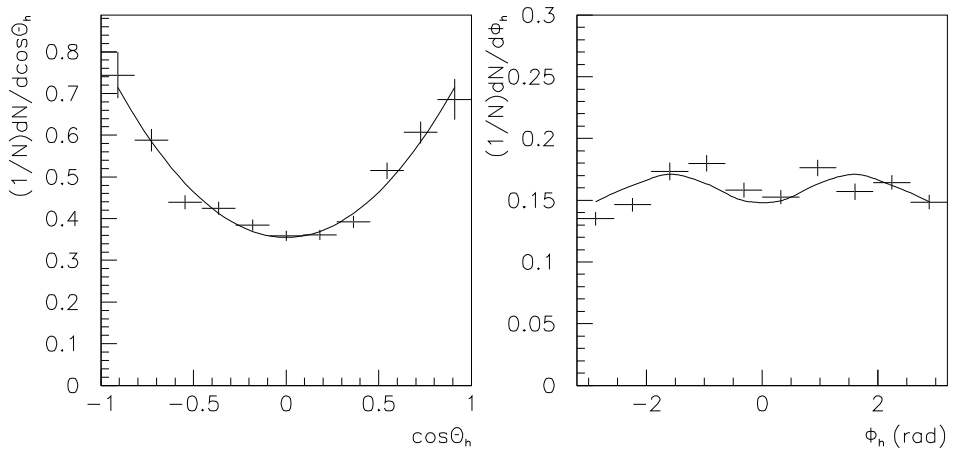

Figure 6.10: Differential distributions $(1/N)dN/d\cos\theta_h$ and $(1/N)dN/d\phi_h$ for elastic for elastic J/ψ photoproduction over the full W range. The curves are the results of the fits described in the text. Only statistical errors are displayed. The parameters of the fit are shown in tab. 6.5.

Matrix Element	Value	χ^2 / *ndf*
r_{00}^{04}	$-0.054 \pm 0.018(stat) \pm 0.030(syst)$	1.50 / 11
r_{1-1}^{04}	$-0.074 \pm 0.017(stat) \pm 0.035(syst)$	3.51 / 10

Table 6.5: Results from fits on the matrix elements r_{00}^{04} and r_{1-1}^{04}.

Conclusions

In this thesis the elastic J/ψ photoproduction in ep interactions has been studied in the range $30 \leq W_{\gamma p} \leq 150$ GeV, via the J/ψ di-muon decay, using a data sample corresponding to an integrated luminosity of 38 pb^{-1}. Compared to the measurement previously pubblished by ZEUS the statistics considered is an order of magnitude larger and the W range has been extended.

The simulation of the physics process using Monte Carlo techniques as well as the study of the detector simulation, trigger efficiency, and background subtraction have been performed.

The elastic $ep \to eJ/\psi p$ and $\gamma p \to J/\psi p$ cross sections in different $W_{\gamma p}$ ranges have been extracted. The measured $W_{\gamma p}$ dependence of the γp cross section

$$\sigma_{\gamma p} \propto W_{\gamma p}^{0.67 \pm 0.05(\text{stat}) \pm 0.05(\text{syst})}$$

confirms, with more accuracy, previous results and appears to be significantly steep with respect to the predictions of the soft pomeron exchange model. A perturbative QCD calculation, justified if the scale of the process is related to the large vector meson mass ($M_{J/\psi} \gg \Lambda_{QCD}$), is in good agreement with the measurements.

The calculated cross sections are slightly higher than the previous measurements by ZEUS and H1. Compared to the previous ZEUS result, the discrepancy may be partially (+15%) explained by the improved description of the muon trigger efficiency.

The search for shrinkage effects as expected from the Regge-like approaches has been done.

The elastic slope parameter b has been measured in different W bins yielding a value of:

$$b = 4.32 \pm 0.12 \text{GeV}^{-2}$$

and

$$b = 4.31 \pm 0.12 + 4 \cdot (0.086 \pm 0.074) \cdot \ln\left(\frac{W_{\gamma p}}{90\text{GeV}}\right) \text{GeV}^{-2}$$

under the assumptions of absence and presence of shrinkage respectively. The data do not allow a distinction between the hypothesis of small and no shrinkage. This still holds combining the new data with previous low energy measurements. A global fit including those results and assuming shrinkage yields to a value of:

$$b = 4.29 \pm 0.11 + 4 \cdot (0.111 \pm 0.059) \cdot \ln\left(\frac{W_{\gamma p}}{90\text{GeV}}\right) \text{GeV}^{-2}$$

The Regge trajectory exchanged in elastic J/ψ photoproduction has been found to be:

$$\alpha_{I\!P}(t) = 1.208 \pm 0.011 + (0.105 \pm 0.038)t.$$

This result is not compatible with the soft pomeron predictions. Based on the energy dependence of the cross sections as well as on the energy independence of the slope parameter a purely soft production mechanism can be ruled out from the present measurements.

Finally the decay angular distributions for elastic J/ψ production have been measured. They seem to be consistent with the s-channel helicity conservation. In photoproduction the produced J/ψ's are predominantly in helicity state 1 or -1 as expected.

Conclusioni

Nella presente tesi si studia la fotoproduzione elastica di J/ψ nelle interazioni ep nell'intervallo $30 \leq W_{\gamma p} \leq 150$ GeV attraverso il decadimento in due muoni, usando un campione di dati corrispondente a una luminosità integrata di $38pb^{-1}$. In confronto alla misura pubblicata in precedenza da ZEUS la statistica considerata è un ordine di grandezza maggiore e l'intervallo di W è stato esteso.

Con l'uso di tecniche Monte Carlo si sono simulati i processi fisici e studiate la simulazione del rivelatore, l'efficienza di "trigger" e la sottrazione del fondo.

Le sezioni d'urto elastica $ep \to eJ/\psi p$ e $\gamma p \to J/\psi p$ sono state estratte in diversi intervalli di $W_{\gamma p}$. La dipendenza da $W_{\gamma p}$ della sezione d'urto γp

$$\sigma_{\gamma p} \propto W_{\gamma p}^{0.67 \pm 0.05(\text{stat}) \pm 0.05(\text{syst})}$$

misurata con maggiore precisione, conferma i risultati precedenti ed appare significativamente più accentuata rispetto alle previsioni del modello di scambio del pomerone soffice, indicando la necessità di ricorrere ad un altro approccio. D'altro canto un calcolo di QCD perturbativa, suggerito dalla grande massa del mesone vettore ($M_{J/\psi} \gg \Lambda_{QCD}$),è in buon accordo con le misure.

Le sezioni d'urto calcolate sono lievemente più alte delle misure precedenti di ZEUS e H1. Rispetto al risultato precedente di ZEUS la discrepanza può essere parzialmente (+15%) spiegata dalla descrizione migliorata delle efficienze di "trigger" per muoni.

Si sono cercati effetti di "shrinkage" contemplati dagli approcci del tipo alla Regge.

Si è misurato il parametro di "slope" elastica b in diversi "bin" di W trovando un valore :

$$b = 4.32 \pm 0.12(stat)\ \text{GeV}^{-2},$$

$$b = 4.31 \pm 0.12 + 4 \cdot (0.086 \pm 0.074) \cdot \ln\left(\frac{W_{\gamma p}}{90\text{GeV}}\right) \text{GeV}^{-2}$$

nelle assunzioni di assenza o presenza di "shrinkage" rispettivamente. La misura è compatibile con le ipotesi di "shrinkage" piccolo o assente. Questo è ancora vero se si combinano i nuovi dati con le precedenti misure a energia inferiore. Un "fit" globale che include tali risultati e assume lo "shrinkage" dà:

$$b = 4.29 \pm 0.11 + 4 \cdot (0.111 \pm 0.059) \cdot \ln\left(\frac{W_{\gamma p}}{90\text{GeV}}\right) \text{GeV}^{-2}.$$

La traiettoria di Regge scambiata nella fotoproduzione elastica di Regge si è trovata essere

$$\alpha_{I\!P}(t) = 1.21 \pm 0.011 + (0.105 \pm 0.038)t.$$

Il risultato non è compatibile con le previsioni del pomerone soffice e favorisce l'assenza di "shrinkage" anche se i dati non sono abbastanza precisi da permettere una affermazione definitiva in proposito. Sulla base della dipendenza dalla energia delle sezioni d'urto come pure della indipendenza dall'energia del parametro di "slope" un meccanismo di produzione puramente soffice può essere scartato.

Infine si sono misurate le distribuzioni angolari per la produzione elastica di J/ψ. Esse appaiono consistenti con la conservazione della elicità nel canale s. In fotoproduzione le J/ψ prodotte sono prevalentemente in uno stato di elicità 1 o -1 come ci si aspetta.

Bibliography

[1] A Donnachie, P.V. Landshoff, Phys.Lett. **B296** (1992) 227.

[2] H1 Collab., S. Aid et al., Z. Phys. **C69** (1995) 27.

[3] ZEUS Collab., M. Derrick et al., Phys. Lett. **C63** (1994) 391.

[4] H. Abramowicz, E. M. Levin, A. Levy, U. Maor, Phys. Lett. **B269**, (1991) 465.

[5] J. R. Cudell, K. Kang, S. K. Kim 1997, Phys Lett. **B395**, 311.

[6] L. P. Haakman, A. Kaidalov, J. H. Koch, *Preprint hep-ph/9507394* (1995).

[7] A Donnachie, P.V. Landshoff, Phys.Lett. **B348** (1995) 213.

[8] M.G. Ryskin, Z. Phys **C57** (1993) 89.

[9] L. Frankfurt, W. Koepf, M. Strikman, Phys. Rev. **D54** (1996) 319.

[10] , K. Schilling and G. Wolf, 1973, Phys Rev. **D7**, 3150

[11] M. Arneodo, L. Lamberti and M.G. Ryskin, Comp. Phys. Comm. 100 (1997) 195.

[12] A. Martin, W. J. Stirling and R. C. Roberts, Phys. Lett. **354** (1995) 155.

[13] M. Kasprzak, *EPSOFT - a Monte Carlo Generator of Soft Photon-Proton Collisions*, ZEUS-Note 95-069, internal report.

[14] S.P. Baranov et el., Physics at HERA, Vol.3, p.1478

[15] J.A.M. Vermaseren, Nucl.Phys., **B229** (1983) p.347

[16] B.H.Y. Hung et al.,*Monte Carlo Generator for Lepton Pair Production by 2-Photon Process for ZEUS*, ZEUS-Note 95-013, internal report.

[17] ZEUS Collab., M. Derrick et al., Phys. Lett. **B350** (1995) 120.

[18] H1 Collab., T. Ahmed et al., Phys. Lett. **B338** (1994) 507.

[19] A. Martin, W. J. Stirling and R. C. Roberts, Phys. Rev. **D47** (1993) 867.

[20] "HERA, A proposal for a Large Electron-Proton Colliding Beam Facility at DESY", DESY HERA 81-10.

[21] G.A.Voss and B.H.Wiik, *The electron-proton collider HERA*, Ann. Rev. Nucl. Part. Sci. 44 (1994), 413.

[22] ZEUS Collab., *The ZEUS Detector*, Technical Proposal, March 1986.

[23] ZEUS Collab., M.Derrick at al., *The ZEUS Detector*, Status Report 1993, DESY (1993).

[24] B.Foster et al., Nucl. Inst. Meth. **A338** (1994) 254.

[25] D.S.Bailey et al., Nucl. Inst. Meth.**A 396** (1997) 320.

[26] Jürgen Krüger, *The Uranium Scintillator Calorimeter for the ZEUS Detector at the Electron-Proton Collider HERA, The Heart of ZEUS*, Internal Report DESY F35-92-02, January 1992.

[27] E. Iarocci, Nuclear Instruments and Methods 217 (1983) 30-42.

[28] E. Iarocci, Laboratori Nazionali di Frascati LNF-87/23(P).

[29] A. Polini, *Il sistema di acquisizione e trigger dello spettrometro di muoni in avanti di ZEUS*, tesi di laurea, unpublished, (1994).

[30] G. Abbiendi et al., Nucl. Instr. & Meth. **A333** (1993) 342; F. Gasparini et al., Nucl. Instr. Meth. **A267** (1988) 87.

[31] S. Limentani, M. Posocco e L. Stanco, ZEUS-Note 92-027, internal report. (1992).

[32] W.H.Smith et al., *The ZEUS Trigger System*, ZEUS-Note 89-084, internal report.

[33] C.Youngman, *The ZEUS Data Acquisition System*, DESY 92-150A.

[34] F. Anselmo at al., *Measurement of the Elastic* $J/\Psi(\rightarrow \mu^+\mu^-)$ *Cross Section in the forward region*, ZEUS-Note 97-023, internal report.

[35] K. Desler, *How to Use the Proton Remnant Tagger in 1996.* ZEUS-Note 97-084, internal report.

[36] W.H. Smith et al., *The ZEUS Calorimeter First Level Trigger*, DESY 94-183.

[37] G. Bruni, *Muons and Mips MAtcher: a package to tag forward muons*, march 95, internal report.

[38] L. Wai, *A Muon Separator*, ZEUS-Note 93-012, internal report.

[39] G. Abbiendi et al., *Observation of* $J/\psi \rightarrow \mu^+\mu^-$ *in the first 274* nb^-1 *of 1993 run*, ZEUS-Note 93-120, internal report.

[40] G. F. Hartner et al., *VCTRAK Briefing: Program and Math*, ZEUS-Note 98-058 internal report.

[41] A. Savin, *Study of Calorimeter Noise 1996 Data*, ZEUS-Note 98-007, internal report.

[42] D. Westphal, private communication.

[43] K.Long, *How to generate input to MOZART*, ZEUS-Note 91-13.

[44] R.Brun et al., CERN DD/EE/84-1 (1987).

[45] R.van Woudenberg, *ZGANA Version 3.05/01, User Manual and Documentation* (1993).

[46] E.Tscheslog, *Zeus Reconstruction Program, Organisation and Control*, ZEUS-Note 91-37, internal report.

[47] ZEUS Collaboration, J. Breitweg et al., Phys. Lett. **B437** (1998) 432.

[48] R. Brugnera, private communication.

[49] A. Bruni, private communication.

[50] H1 Collab., S. Aid et al., Z. Phys. Phys. Lett. **B421** (1998) 385.

[51] Particle Data Group, C. Caso et al., Eur Phys. J., **C3** (1998)

[52] A. Mastroberardino *Diffvm - a Monte Carlo Generator for Diffractive Processes in ep Scattering. Long Write-up* ZEUS-Note 98-057, internal report.

[53] L. Frankfurt, W. Koepf, M. Strikman, Phys. Rev. **D57** (1998) 512.

[54] V.N. Gribov et al., Sov. Phys. JETP 14 (1962) 1308;
V.M. Budnev et al., Phys. Rep. **C15** (1975) 181.

[55] H1 Collaboration, S. Aid. et al., Nucl. Phys, **B472** (1996) 3.

[56] E516 Collaboration, B. H. Denby et al., Phys. Rev. Lett. **52** (1984) 795.

[57] E401 Collaboration, M. Binkley et al., Phys. Rev. Lett. **48** (1982) 73.

[58] H. L. Lai et al. Phys Rev. **D55** (1997) 1280.

[59] M. Glück, E. Reya, A. Vogt, Z. Phys. **C67** (1995) 433.

[60] A.D. Martin, R.G. Roberts, W.J.Stirling, Phys Lett. **B237** (1996) 419.

[61] A Donnachie, P.V. Landshoff, hep-ph/9806344 (1998).

[62] A. Levy, hep-ph/9712519(1997).

[63] ZEUS Collaboration, J. Breitweg et al., Z. Phys. **C75** (1997) 215.

[64] ZEUS Collaboration, J. Breitweg et al., Z. Phys. **C76** (1997) 599.

[65] H1 Collaboration, *Diffractive J/ψ Photoproduction*, Submitted to the International Europhysics Conference on High Energy Physics, HEP99, Tàmpere, Finland, July 1999.

Acknowledgements

I would like to thank first of all Prof. Maurizio Basile for having led me in this experience of education and work in the DESY laboratories in Hamburg, and for having followed carefully this thesis.

Thanks particularly to Alessia Bruni, for her invaluable help and many advices in this analysis, and to Rosario Nania, Giuseppe Iacobucci and Giuseppe Barbagli who have followed very friendly and kindly the development of the manuscript and contributed with many suggestions.

I wish to thank my colleagues and friends from Bologna, among which Lorenzo Bellagamba, Massimo Corradi, Davide Boscherini and Graziano Bruni, for interesting discussions and useful advices. Moreover I would like to thank the ZEUS working group on Diffractive Physics and its current coordinators, Halina Abramowicz, Michele Arneodo, Jim Whitmore and Yuji Yamazaki, who have stimulated the progress of this analysis.

This experience has allowed me to get in touch with the issues of data analysis, with which I was less familiar, having spent last years working essentially on the development of the experimental apparatus, with particular respect to data acquisition and control software. I have realized how fascinating and complex data analysis and physics can be.

I would like to thank for their patience my work colleagues in the project of the new ZEUS microvertex detector, where I have been forced to limit my efforts in these last months spent on my thesis, and particularly Christopher Youngman and Roberto Carlin.

This work finally permitted me to analyze the data of the Forward Muon Spectrometer, the detector I have seen to grow up since my first involvement in ZEUS, in my work on data acquisition and trigger, 6 years ago, which costed me a lot of sleepless nights.

Finally I would like to thank all the friends from Hamburg, in no particular order, Marcella Capua, Maria Carmela Petrucci, Antonio Pellegrino, Enrico Tassi, Alberto Garfagnini, Raphael Galea and the bad luck mate Nicola Coppola. I am sure to forget many and I apologize. Their friendship and kindness have been very important to me in these years.

Thanks to all people who, at any time during the day or the night, have come or will come to my office (at 2010) for drinking coffee, or eventually for discussing problems or chatting about CDs to buy and concerts to see in the weekend.

This work is dedicated to my mother and my father, who always supported my interests and my choices, even when this caused long periods of separation.

Ringraziamenti

Desidero ringraziare prima di tutto il Professor M. Basile per avermi guidato in questa esperienza formativa e di lavoro nei laboratori di DESY Amburgo e per aver seguito attentamente e con pazienza la stesura di questo lavoro di tesi.

Un ringraziamento particolare va alla Dott. Alessia Bruni per il prezioso aiuto ed i numerosi consigli nella realizzazione di questa analisi e a Rosario Nania, Giuseppe Iacobucci e Giuseppe Barbagli che, con massima disponibilità, hanno seguito la stesura del manoscritto e contribuito con numerosi suggerimenti.

Desidero ricordare i colleghi e amici di Bologna tutti, tra cui Lorenzo Bellagamba, Massimo Corradi e Davide Boscherini e Graziano Bruni per le interessanti discussioni e gli utili consigli. Desidero altresì ringraziare il gruppo di lavoro a ZEUS sulla fisica diffrattiva e di fotoproduzione ed i suoi attuali coordinatori Halina Abramowicz, Michele Arneodo, Jim Withmore e Yuji Yamazaki che hanno stimolato l'approfondimento di questa analisi.

Questa esperienza mi ha permesso di venire a contatto con le problematiche dell'analisi dati con cui ero meno familiare essendomi negli ultimi anni prevalentemente occupato dello sviluppo dell'apparato sperimentale con particolare riguardo ai sistemi di acquisizione e al software di controllo. Ho scoperto quanto l'analisi dati e la fisica possano essere affascinanti e complesse.

Questo lavoro di tesi mi ha permesso di analizzare finalmente i dati dello spettrometro di muoni in avanti, rivelatore che ho visto crescere fin dalle mie prime attività in ZEUS, nella realizzazione dell'acquisizione e del trigger, ormai più di 6 anni fa, e che mi è costato tante notti insonni.

Ringrazio per la pazienza i colleghi di lavoro nel progetto del nuovo rivelatore di microvertice ZEUS, ed in particolare Christopher Youngman e Roberto Carlin, verso i quali ho dovuto limitare, mio malgrado, l'impegno negli ultimi mesi di lavoro sula tesi.

Infine un rigraziamento a tutti gli amici di Amburgo, tra i quali non posso che ricordare in ordine sparso e senza alcun criterio Marcella Capua, Maria Carmela Petrucci, Antonio Pellegrino, Enrico Tassi, Alberto Garfagnini, Raphael Galea oltre al compagno di sventura Nicola Coppola. Sono sicuro di dimenticarne molti, molti altri. La loro amicizia e la estrema disponibilità hanno rappresentato per me una parte importante di questi anni.

A tutti coloro che a qualsiasi ora del giorno o meglio della notte sono venuti o verranno a trovarmi in ufficio (al 2010), magari per un caffè, un problema da discutere o per una chiacchierata sul programma di acquisti discografici e concerti del fine settimana, anche a loro esprimo il mio ringraziamento.

Dedico questo lavoro a mia madre e mio padre che in questi anni hanno sempre

sostenuto i miei interessi ed appoggiato le mie scelte anche quando questo comportava lunghi periodi di lontananza.